Simulation and Process Development for Ion-Implanted N-type Silicon Solar Cells

A Thesis
Presented to
The Academic Faculty

By

Steven Ning

In Partial Fulfillment

Of the Requirements for the Degree

Master of Science in Electrical and Computer Engineering

Georgia Institute of Technology

May 2013

Approved by:

Dr. Ajeet Rohatgi, Advisor
School of Electrical and Computer Engineering
Georgia Institute of Technology

Dr. Bernard Kippelen
School of Electrical and Computer Engineering
Georgia Institute of Technology

Dr. Thomas K. Gaylord
School of Electrical and Computer Engineering
Georgia Institute of Technology

Date Approved: 5th April, 2013

This work is dedicated to

My Family

for their unconditional love, to which I owe everything.

The Georgia Tech Solar Jackets

for the inspiration they have given me,

may they continue to inspire generations of students to come.

Acknowledgments

I am grateful for the guidance provided by Dr. Young Woo Ok of the UCEP on all aspects of N-type solar cell fabrication and characterization. Without his help, development of the simulation models in this work would have been impossible. I am also grateful for the substantial assistance and troubleshooting provided by John Renshaw of the UCEP during development of the Sentaurus code used in this study. Parts of the Sentaurus Structure Editor and Sentaurus Device code are taken from his work.

I would like to acknowledge Dr. Fuccio Cristiano and Zahi Essa of the CNRS-LAAS Laboratory in Toulouse (France), as well as Dr. Bartek Pawlak of IMEC (Belgium), for their invaluable assistance in teaching me the use of the Sentaurus AdvancedCalibration package. Without their help, the process simulation would never have produced correct results. I would also like to acknowledge Dr. Santosh Kurinec and Dr. Karl Hirschman of Rochester Institute of Technology for their assistance and experienced guidance in performing ion implantation. I am indebted to Brian Rounsaville of the UCEP for his guidance and assistance in photolithography techniques and small-area cell fabrication. I would also like to acknowledge the patient help provided by the R&D staff at Suniva, Inc. with ion implantation and wafer texturing.

I would like to thank Francesco Zimbardi of the UCEP, for his patient instruction on all steps of the solar cell fabrication procedure, as well as instruction on operation of all the equipment. I would also like to thank Vinny Nguyen and the rest of the Georgia Tech cleanroom staff for their help with custom processing procedures for solar cells which they had not attempted before. I am also thankful to Dr. Muhannad Bakir of Georgia Tech for teaching me the basics of semiconductor process simulation and showing me what was possible, from which the concept for this research project was born.

I am grateful for the support of the other UCEP members: Ajay Upadhyaya, Dr. Arnab Das, Erik Westman, Eunhwan Cho, Dr. Ian Cooper, Jim Keane, Jiun Hong Lai, Keith Tate, Kumar Upadhyaya, Kyungsun Ryu, Malka Kadish, Dr. Moon Hee Kang, Ricky Chen, and

Dr. Yuguo Tao. Their technical and emotional support through this process made all the difference. I am especially grateful to Carla Crippins for her care and assistance while I hobbled around with a broken foot. I am also thankful to her for taking care of all of the UCEP!

I would like to express gratitude to Dr. Bernard Kippelen and Dr. Tom Gaylord of Georgia Tech for their generosity of time in serving on my thesis reading committee. Finally I would like to express sincere gratitude to Dr. Ajeet Rohatgi for his support and guidance in all aspects of this work, from concept through completion. This study would not have been possible without his help!

Contents

List of Tables

List of Figures

List of Symbols and Abbreviations

ALD Atomic Layer Deposition

BIC Boron Interstitial Cluster

BOE Buffered Oxide Etch

BRL Boron Rich Layer

BSF Back Surface Field

BSRV Back Surface Recombination Velocity

CZ Czochralski-Grown

ECV Electrochemical Capacitance-Voltage

FGA Forming Gas Anneal

FSRV Front Surface Recombination Velocity

FZ Float Zone

IBC Interdigitated Back Contact

IQE Internal Quantum Efficiency

IV Current-Voltage

LBSF Local Back Surface Field

LID Light Induced Degradation

PECVD Plasma Enhanced Chemical Vapor Deposition

PERL Passivated-Emitter Rear Locally-Diffused

QSSPC Quasi Steady State Photoconductance

SIMS Secondary Ion Mass Spectrometry

SRH Shockley-Read-Hall

SRV Surface Recombination Velocity

UCEP University Center of Excellence for Photovoltaics Research and Education

E_o Original particle energy

η Cell efficiency

f_active Activation factor

FF Fill Factor

J_o Reverse leakage current density

J_sc Short circuit current density

M_1 Incident particle mass

M_2 Stationary particle mass

N_{active} Active atom count

$N_{inactive}$ Inactive atom count

R_s Series resistance

R_sh Shunt resistance

S Recombination velocity

S_{eff} Effective recombination velocity

τ_{bulk} Bulk carrier lifetime

τ_{eff} Effective carrier lifetime

θ Implant angle, scatter angle

V_{oc} Open circuit voltage

W Thickness of wafer

Summary

As the efficiency potential for the industrial P-type Al-BSF silicon solar cell reaches its limit, new solar cell technologies are required to continue the pursuit of higher efficiency solar power at lower cost. It has been demonstrated in literature that among possible alternative solar cell structures, cells featuring a local BSF (LBSF) have demonstrated some of the highest efficiencies seen to date. Implementation of this technology in industry, however, has been limited due to the cost involved in implementing the photolithography procedures required. Recent advances in solar cell doping techniques, however, have identified ion implantation as a possible means of performing the patterned doping required without the need for photolithography.

In addition, past studies have examined the potential for building solar cells on N-type silicon substrates, as opposed to P-type. Among other advantages, it is possible to create N-type solar cells which do not suffer from the efficiency degradation under light exposure that boron-doped P-type solar cells are subject to. Industry has not been able to capitalize on this potential for improved solar cell efficiency, in part because the fabrication of an N-type solar cell requires additional masking and doping steps compared to the P-type solar cell process. Again, however, recent advances in ion implantation for solar cells have demonstrated the possibility for bypassing these process limitations, fabricating high efficiency N-type cells without any masking steps.

It is clear that there is potential for ion implantation to revolutionize solar cell manufacturing, but it is uncertain what absolute efficiency gains may be achieved by moving to such a process. In addition to development of a solar specific ion implant process, a number of new

thermal processes must be developed as well. With so many parameters to optimize, it is highly beneficial to have an advanced simulation model which can describe the ion implant, thermal processes, and cell performance accurately. Toward this goal, the current study develops a process and device simulation model in the Sentaurus TCAD framework, and calibrates this model to experimentally measured cells. The study focuses on three main tasks in this regard:

Task I - Implant and Anneal Model Development and Validation

This study examines the literature in solar and microelectronics research to identify features of ion implant and anneal processes which are pertinent to solar cell processing. It is found that the Monte Carlo ion implant models used in IC fabrication optimization are applicable to solar cell manufacture, with adjustments made to accommodate for the fact that solar cell wafers are often pyramidally textured instead of polished. For modeling the thermal anneal processes required after ion implant, it is found that the boron and phosphorus cases need to be treated separately, with their own diffusion models.

In particular, boron anneal simulation requires accurate treatment of boron-interstitial clusters (BICs), transient enhanced diffusion, and dose loss. Phosphorus anneal simulation requires treatment of vacancy and interstitial mediated diffusion, as well as dose loss and segregation. The required models are implemented in the Sentaurus AdvancedModels package, which is used in this study. The simulation is compared to both results presented in literature and physical measurements obtained on wafers implanted at the UCEP. It is found that good experimental agreement may be obtained for sheet resistance simulations of implanted wafers, as well as simulations of boron doping profile shape. The doping profiles of phosphorus as measured by the ECV method, however, contain inconsistencies with measured sheet resistance values which are not explained by the model.

Task II - Device Simulation Development and Calibration

This study also develops a 3D model for simulation of an N-type LBSF solar cell structure. The 3D structure is parametrized in terms of LBSF dot width and pitch, and an algorithm is used to generate an LBSF structure mesh with this parametrization. Doping profiles generated by simulations in Task I are integrated into the solar cell structure. Boundary conditions and free electrical parameters are calibrated using data from similar solar cells fabricated at the UCEP, as well as data from lifetime test wafers. This simulation uses electrical models recommended in literature for solar cell simulation.

It is demonstrated that the 3D solar cell model developed for this study accurately reproduces the performance of an implanted N-type full BSF solar cell, and all parameters fall within ranges expected from theoretical calculations. The model is then used to explore the parameter space for implanted N-type local BSF solar cells, and to determine conditions for optimal solar cell performance. It is found that adding an LBSF to the otherwise unchanged baseline N-type cell structure can produce almost 1% absolute efficiency gain. An optimum LBSF dot pitch of 450 μm at a dot size of 100 μm was identified through simulation. The model also reveals that an LBSF structure can reduce the fill factor of the solar cell, but this effect can be offset by a gain in V_{oc}. Further efficiency improvements may be realized by implementing a doping-dependent SRV model and by optimizing the implant dose and thermal anneal.

Task III - Development of a Procedure for Ion Implanted N-type LBSF Cell Fabrication

Finally, this study explores a method for fabrication of ion-implanted N-type LBSF solar cells which makes use of photolithographically defined nitride masks to perform local phosphorus implantation. The process utilizes implant, anneal, and metallization steps previously developed at the UCEP, as well as new implant masking steps developed in the course of this study. Although an LBSF solar cell has not been completely fabricated, the remaining

steps of the process are successfully tested on implanted N-type full BSF solar cells, with efficiencies reaching 20.0%.

Chapter 1

Introduction

1.1 Statement of Problem

The quest to pursue more widespread adoption of solar cells over hydrocarbon-based fuels for electric power generation increasingly demands more cost-effective means to fabricate high efficiency solar cells. The workhorse of the terrestrial solar industry for the past few decades has undoubtedly been the P-type Al-BSF crystalline silicon solar cell. This technology, however, is reaching the limits of its efficiency potential, and there is now a need for new solar cell designs which break from established formula in order to reach higher efficiencies at lower cost. Among candidates for new silicon-based technologies today, ion implantation and N-type substrates show particular promise.

Phosphorus doped N-type substrates offer significant advantages over boron doped P-type substrates. Namely, they do not suffer from light-induced degradation (LID), are insensitive to common contaminants in the fabrication process, and feature high carrier lifetime [1, 8]. The fabrication of N-type solar cells, however requires an additional masking and doping step compared to P-type solar cells, since the back surface field (BSF) can no longer be formed in the same step as rear metallization. For this reason, the N-type process has historically been too expensive for mass adoption. Recently, however, there have been

studies using ion-implantation to dope both front and rear surfaces of N-type substrates with high-throughput and no additional masking [9, 10, 11].

A technology used for decades in the microelectronics industry, ion-implantation opens possibilities for the large-scale fabrication of novel solar cells previously infeasible for industrial production. In addition to the creation of full surface BSF, recent studies have suggested that ion-implantation can be used to perform patterned doping of solar cells using cheap hard masks. Patterned doping has been used in the past to create locally doped BSF (LBSF) structures for use in record-setting cells such as the PERL. This patterning, however, was accomplished using expensive and time-consuming photolithographically [12, 1]. If ion-implantation is shown to be capable of creating PERL-type structures without the need for photolithography, high efficiency LBSF solar cells would quickly become viable candidates for mass-production.

As the issues mentioned above suggest, there are a large number of parameters which determine overall performance for an ion-implanted N-type LBSF solar cell. In order to develop a road map to guide efficient development of this technology, advanced simulation techniques are required. This study aims to develop such a simulation, and then use it to investigate the performance of this novel solar cell structure.

1.2 Research Objectives

In order to address the problem posed, we identify three crucial tasks which must be accomplished, as discussed below.

Task I - Implant and Anneal Model Development and Validation

We require first an accurate characterization of the dopant distribution resulting from ion implant and anneal. In the literature, data for ion implanted dopant distribution is underrepresented for solar-cell relevant thermal treatments. Thus, for Task I, a process simulation

is developed which predicts dopant distributions for solar-cell-specific implant and anneal conditions. These implant and anneal conditions have been developed at the University Center of Excellence for Photovoltaics Research and Education (UCEP) for fabrication of high efficiency ion-implanted N-type solar cells. The UCEP experimental data are used to fine tune the simulation model. The process simulation also provides information on quantities which are experimentally unmeasurable, such as inactive dopant concentration and distribution.

Task II - Device Simulation Development and Calibration

Next, a calibrated device model must be developed which performs electrical simulation of an ion implanted solar cell structure. The current study accomplishes this by building on an existing solar cell simulation developed by Synopsys, expands its functionality to N-type LBSF solar cells, and integrates with it the previously discussed process simulation for ion implantation and anneal. As far as the author knows, no prior study in literature has developed such a combined process-device simulation model for ion-implanted solar cells. The 3D device model is calibrated against experimental data taken from implanted N-type solar cells fabricated at the UCEP. Parametric studies are then performed using the model in order to find performance-optimizing parameters for ion-implanted N-type LBSF solar cells.

Task III - Development of a Procedure for Ion Implanted N-type LBSF Cell Fabrication

Finally, a procedure must be developed for fabrication of an implanted N-type LBSF solar cell in order to validate the model. This work discusses preliminary work toward developing such a procedure. While there are known methods for fabricating LBSF structures using photolithography and diffusion, there are no established methods for doing the same using ion implantation. At the time of writing, efforts toward achieving this final task are ongoing.

The nature of the last section of this study is therefore exploratory, and its results will serve to provide guidance for future work on ion-implanted LBSF solar cells.

Chapter 2

Review of the Current State of the Art

This study spans four separate areas of active solar cell research: N-type substrates, ion implantation, LBSF structures, and advanced simulation. The current state of the art in each area will be discussed in the following sections.

2.1 N-Type Substrates

2.1.1 N-Type Advantages and Trade-Offs

Solar cells utilizing N-type substrates have been studied for many decades. As discussed previously, N-type substrates confer a number of advantages over P-type substrates. Among these, the most important to solar cell design are absence of light inducted degradation (LID), high bulk lifetimes, and insensitivity to common contaminants [1, 8].

LID is a well known phenomenon in boron doped P-type silicon substrates. During the fabrication process for a solar cell, oxygen impurities can be introduced into the bulk. Under illumination, the minority carrier lifetime of the device is seen to decrease over time. This

has been attributed to the formation of metastable boron-oxygen complexes with an effective trapping level around mid-gap [13]. These complexes can be dissolved under low temperature thermal anneal at 200 °C, but under solar cell operating conditions, such an annealing process in infeasible. Using phosphorus doped N-type silicon as substrate material effectively bypasses the effects of LID.

Iron is a common contaminant in semiconductor grade silicon, degrading carrier lifetimes and reducing the overall performance of the device. It has been shown that Fe interstitials have a higher capture cross section for electrons than holes, however, which means that N-type materials are less sensitive to Fe contamination than P-type materials [14]. As a result of the effects of such contaminants, P-type substrates in the solar industry typically have carrier lifetimes one order of magnitude lower than N-type substrates. In order to reach the highest efficiencies theoretically predicted for silicon solar cell operation, it is preferable for this reason to start with N-type silicon substrates.

The majority of industrial solar cells produced today utilize P-type silicon as a substrate. This is due in part to the simplicity of the process involved. N+ phosphorus emitter formation for a P-type solar cell occurs in a diffusion furnace under a POCl ambient. The BSF for the solar cell is formed simultaneously with the rear electrical contact during the firing process, wherein the aluminum paste alloys with silicon in the interface to create a P+ region [15].

For an N-type silicon solar cell, on the other hand, rear contact formation and rear surface doping can no longer be combined. It is necessary to separately dope the surfaces - most often in a BBr_3 ambient for the front, and a POCl ambient for the rear. Diffusion furnaces, however, introduce dopant to both sides of the wafer simultaneously. For this reason, measures such as wafer doubling or nitride masking must be taken to ensure that the dopants diffuse into only their intended surface. Ion implantation is an alternative doping process, discussed in Section 2.3.1, which bypasses this additional masking requirement.

2.1.2 N-Type Surface Passivation

Surface passivation techniques also differ for N-type solar cells compared to P-type. Because bulk lifetimes are so high (on the order of 700 μs for the complete device), performance of an N-type solar cell depends sensitively on front and rear surface passivation quality. For the P-type solar cell with low bulk lifetime, a simple oxide-nitride stack is sufficient to adequately passivate front and rear surfaces. For the N-type solar cell, use of the same oxide-nitride stack on the P+ surface will preclude attainment of high device efficiency. This is due to the fact that positive fixed charges in the PECVD-grown nitride induce an inversion layer in the P+ surface, greatly increasing the surface recombination rate.

Alternative passivation materials such as Al_2O_3 have been under investigation for P+ surfaces of N-type solar cells [1, 16]. Unlike PECVD nitrides, Al_2O_3 grown via atomic layer deposition (ALD) carries negative fixed charges, and does not introduce an inversion layer but rather an accumulation layer. This provides a degree of field effect passivation which reduces the surface recombination velocity (SRV). It has also been shown that PECVD nitrides in some cases can provide acceptable passivation for P-type surfaces. Schmidt et al. have demonstrated that PECVD SiN grown at a stoichiometric conditions can achieve recombination values of $S_{eff} = 10\,\mathrm{cm/s}$ for $1\,\Omega \cdot \mathrm{cm}$ P-type wafers at certain injection levels [17].

2.1.3 Example N-Type Process

A good example of a modern N-type solar cell, and in many ways the prototype for the cell proposed in this study, was fabricated by Benick et al. with Fraunhofer ISE in 2008. The cell structure is shown in schematic form in Figure 2.1[1]. This design is itself heavily based on the PERL cell structure first developed in 1990 by Wang et al. [12].

The cell features an float-zone grown $1\,\Omega \cdot \mathrm{cm}$ N-type substrate with a thickness of 250 μm. The front surface is textured using inverted pyramids, and a P+ emitter is diffused using BBr_3 ambient. Front surface passivation is achieved using an Al_2O_3-nitride stack. Front

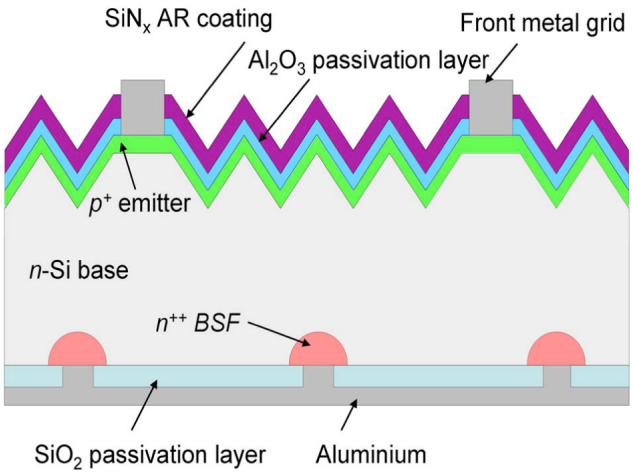

Figure 2.1: Schematic of Al_2O_3-passivated N-type LBSF Solar Cell[1]

Table 2.1: Performance Parameters for LBSF Cell from Benick et al.[1]

	V_{oc} (mV)	J_{sc} ($^{mA}/_{cm^2}$)	**FF** (%)	η (%)
Average	696.9 ± 5.6	40.9 ± 0.3	78.8 ± 1.8	22.5 ± 0.7
Best	703.6	41.2	80.2	23.2

contacts are defined by photolithography and subsequently evaporated and plated. The planar rear surface is locally N+ doped with a phosphorus diffusion, and coated with an SiO_2 passivation layer with openings under the local diffusion regions. Rear contact is achieved with a full surface aluminum evaporation.

This structure exhibits an average efficiency of 22.5%, and a maximum efficiency of 23.2%. Parameters of the cell performance are summarized in Table 2.1. Of note is the high V_{oc} of 703.6 mV, which can be attributed to the excellent front surface passivation afforded by the Al_2O_3-nitride stack, and rear surface passivation by the LBSF structure. This study investigates methods by which to reproduce the LBSF of this solar cell using ion implantation technology to simplify the process.

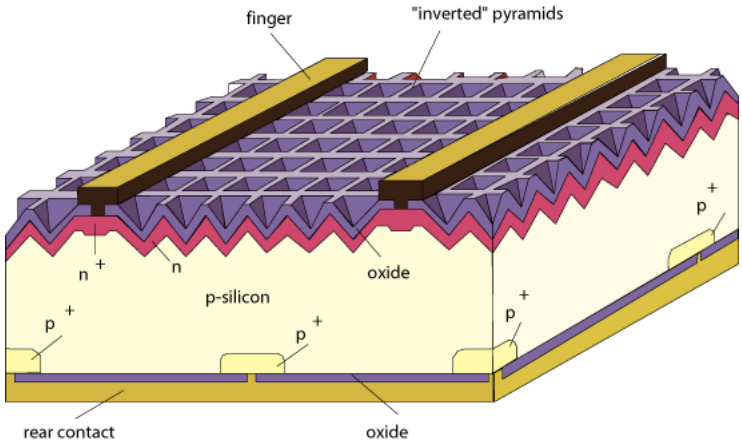

Figure 2.2: PERL Cell Schematic [2]

2.2 LBSF Solar Cells

2.2.1 LBSF Implementation in PERL Cell

The LBSF structure for passivating the rear side of a solar cell has been known for decades. The fundamental idea behind the LBSF concept is to maintain doped BSF regions in the rear of the solar cell only where contact is being made. The diffused regions serve to provide field effect passivation for the metal-silicon interface, and also to allow for a low resistance ohmic contact. The rest of the rear surface (the field) is covered with a dielectric. Because of the low doping in the field, the dielectric passivation quality is also much greater, and the overall rear surface recombination much lower compared to a conventional solar cell. The PERL cell, first fabricated by Wang et al. in 1990, is perhaps the most well known of LBSF-type cells [18, 12]. Shown in Figure 2.2 is a schematic representation of the PERL structure.

In the PERL cell, the LBSF takes the form of a dot-grid pattern of diffused regions on the rear surface of a P-type solar cell. These dots have a width of $30-100\,\mu$m, and a pitch of $250-500\,\mu$m. The entire rear surface is covered with a passivating oxide, with the exception of $10-50\,\mu$m windows centered at the diffused regions. An evaporation of aluminum covers the oxide, and makes contact to the diffused regions only through these windows. The cells also featured inverted pyramid texturing and a planar rear surface. PERL cells fabricated

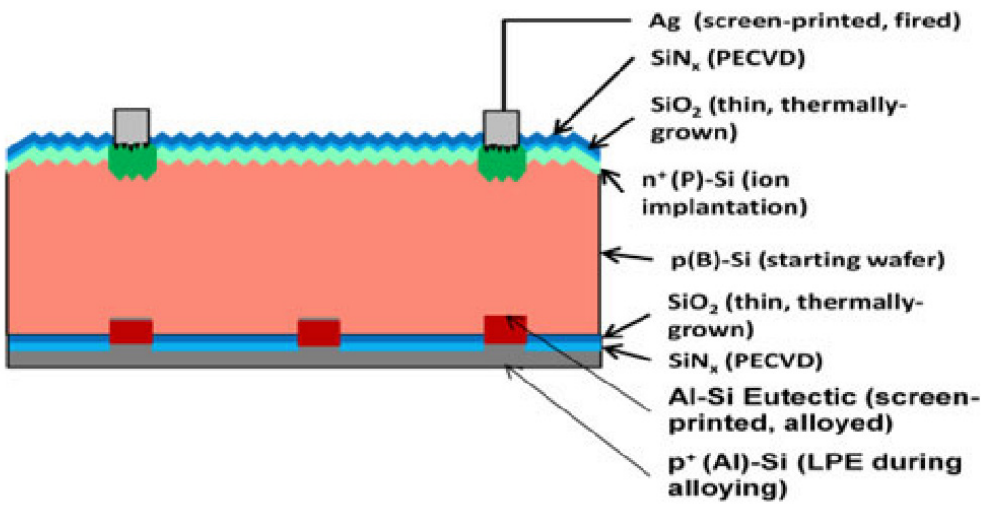

Figure 2.3: Delta-Star Cell Schematic

in the study had a maximum efficiency of 24.2% [12]. A later study by Zhao et al. increased this efficiency to 24.7%, which remains one of the highest seen in monocrystalline silicon solar cells to date [19].

The LBSF structure has the potential for higher performance than a standard full BSF. The reasons for this are twofold: the reduction in area coverage of the highly doped BSF region results in lower Auger recombination on the rear surface, and the increased passivation quality on the undoped surface reduces the overall BSRV. These two features together provide the cell with a high V_{oc} of over 700 mV. Back of the envelope calculations show $J_{0b} = 25\,{}^{\mathrm{fA}}/_{\mathrm{cm}^2}$ for a PERL-type structure [20]. Fabrication of the PERL cell, however, requires many time-consuming photolithography steps. In addition to the steps needed to form the contact regions, other steps utilizing photolithography include patterning the rear side diffusion mask, creating the inverted pyramid structures, and isolating the edges of the cells. For these reasons, it has never been feasible to manufacture PERL cells on a commercial scale.

2.2.2 LBSF Implementation in Delta-Star Cell

Another solar cell structure which utilizes the LBSF concept is the Delta-Star cell, developed by Ramanathan et al. and Lai et al.. The Delta-Star structure is summarized in Figure 2.3. It is similar to the PERL cell in some respects, but is designed to be fabricated without the need for any photolithography steps. The Delta-Star cell features a random pyramidally textured front side and a planar back side. The front emitter is formed by ion-implanted phosphorus, and both surfaces are passivated by an oxide-nitride stack. Windows in the rear dielectric are subsequently opened via laser ablation or screen printed etching paste. The LBSF and rear contacts are formed simultaneously when screen printed aluminum is fired through these windows. The front contacts are achieved by firing screen printed silver paste [21, 22]. The Delta-Star cell has been shown to reach 20.3% efficiency and $V_{oc} = 657\,\text{mV}$ with etching paste opened dielectric windows. Compared to a full-surface aluminum BSF cell, the LBSF structure on the Delta-Star gives it a 17mV boost in V_{oc} [22]. A comparable process has also been developed by Schneiderlochner et al. in which the laser step simultaneously opens the dielectric and fires the contact [23].

2.3 Ion Implanted Solar Cells

2.3.1 Ion Implantation Basics

The concept of the ion implanted solar cell has been around for decades, but not until recently has a cost effective means been developed for uniformly implanting large area solar cells at production rates [24, 25, 4, 26, 27]. Figure 2.4 shows a schematic of the ion implantation process. The implanter accelerates dopant ions through an electric potential gradient, focuses the ions into a beam, and directs the beam onto a target substrate [3, 28, 29]. Because of the high directionality of the implant process, no masking is required to prevent dopants from reaching the opposite wafer surface [11, 10].

There are three main process parameters which are relevant to solar cell fabrication for an ion implant system: dose, energy, and angle. Dose is a measure of the flux of dopant atoms

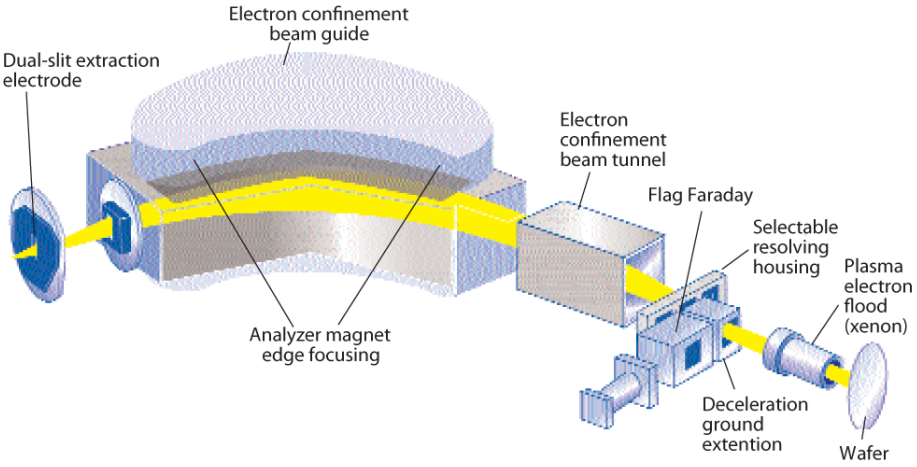

Figure 2.4: Ion Implantation Schematic [3]

which impinge upon the surface of the substrate wafer, integrated over time. It represents the final number of atoms implanted into the substrate, and is measured in units of atoms per square centimeter. The dose as measured by the ion implantation tool, however, does not necessarily correspond the the dose received by the silicon surface for textured substrates. The ions impinging upon a textured surface arrive at an angle relative to the faces of the texture pyramids. The effective dose into a single face of a pyramid reduces as the cosine of the angle of incidence. Equivalently, it can be said that the implanted dose is distributed over the larger effective surface area provided by the texturing.

Implant energy, on the other hand, is a measure of the electric potential accelerating dopant atoms toward the target substrate. As such, it is a proxy for the kinetic energy of the dopant atoms. Implant energy is typically measured in the tens of keV, with higher implant energy corresponding to deeper substrate penetration [29]. For this study, implant energies of between 5 keV and 30 keV are used.

Ion implantation has been studied in depth by the microelectronics industry. It has been found that implanting at certain angles relative to the crystal lattice greatly increase the implantation depth of the ions. This phenomenon is termed “channeling”, and occurs when the implant beam is aligned to a crystallographic orientation in which ions can travel unimpeded through channels between silicon atoms in the lattice. In order to avoid this behavior, the

ion beam is often aimed at an angle of 5 to 7 degrees off of perpendicular to the substrate. For implanting into a pyramidally textured surface, the effective angle of incidence of the ions is further increased due to the tilt of the pyramid faces. It has also been shown that a thin layer of oxide can serve as an effective scattering layer, randomizing the direction of implanted ions and thus reducing the channeling effect [29].

2.3.2 Post Ion Implantation Anneal

The implant process produces crystal damage on the surface of the implanted wafer. In addition to dopant ions, the implantation introduces a supersaturation of silicon self-interstitials in a shallow region near the surface. After implantation, wafers must undergo a thermal anneal process in order to repair this damage and dissolve the self-interstitials. In addition, the thermal anneal serves to diffuse dopant atoms further into the substrate and electrically activate them [30, 31, 32]. There are numerous dynamics between interstitials and dopants which affect the diffusion and activation process. These are discussed in depth in Section 3.2 and Section 3.4.

After the post-implant anneal, it is possible to grow a thermal oxide on the wafer to serve as surface passivation. This oxidation process also affects the diffusion behavior of the dopants. Since boron and phosphorus behave differently under thermal annealing and oxidation conditions, work at the UCEP on ion implanted solar cells have utilized two separate implant-anneal processes: one for the boron emitter, and one for the phosphorus BSF. From a production standpoint, however, it can be advantageous to combine both anneal processes into one, termed a "co-anneal" [33]. Development of a feasible co-anneal, however, is dependent on whether the process can avoid formation of a boron-rich layer on the surface of the silicon, a topic discussed in Section 3.2.4.

2.3.3 Example Ion Implanted Solar Cell Process

The UCEP, in collaboration with Suniva, has done much work in pioneering the development of ion implanted solar cells [26, 4]. Shown in Figure 2.5 is a representative schematic, and

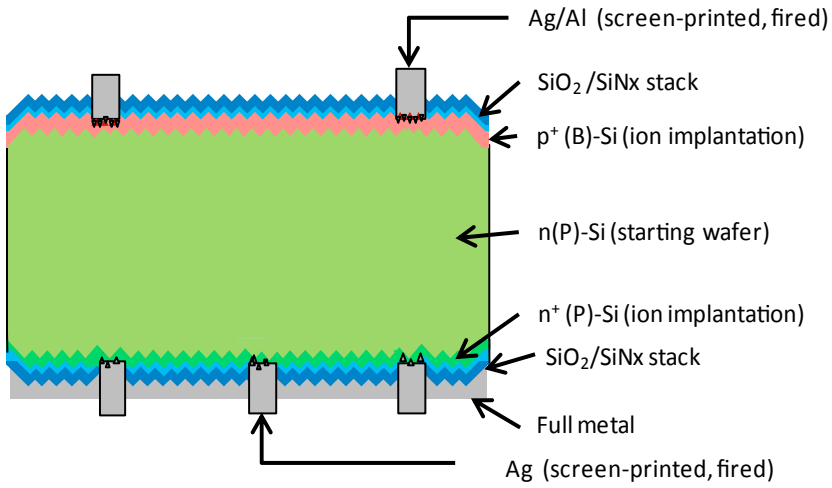

Figure 2.5: Baseline Implanted N-Type Cell Schematic [4]

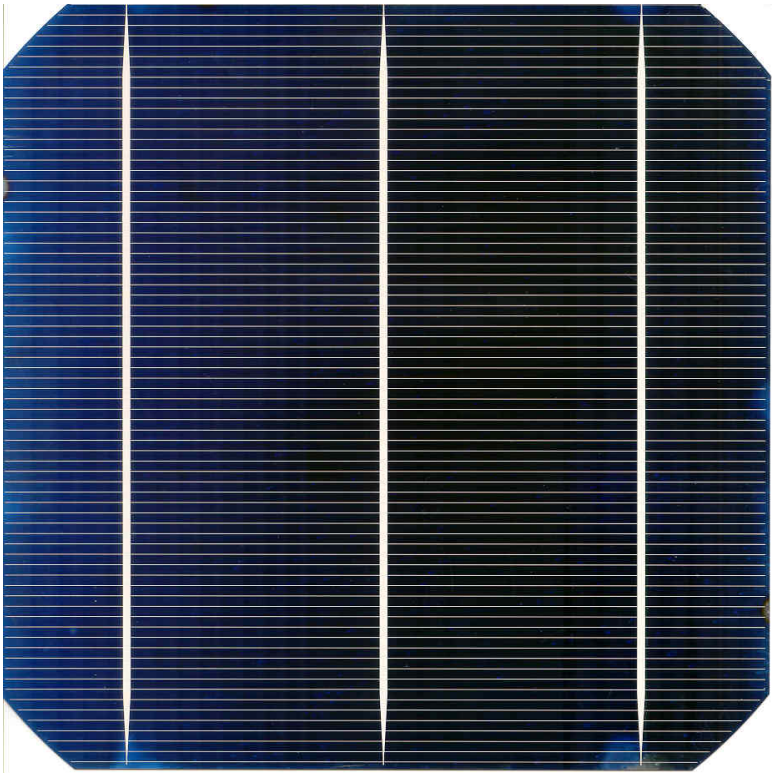

Figure 2.6: Photograph of Typical Implanted N-type Baseline Cell

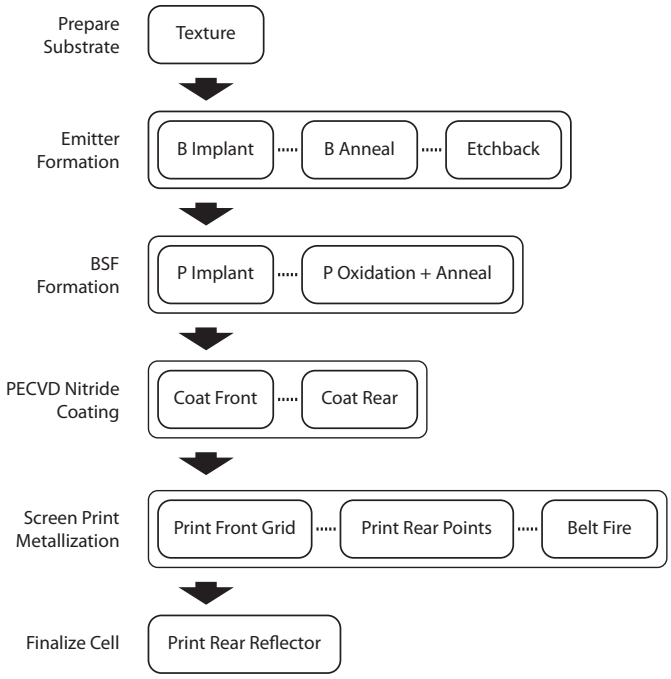

Figure 2.7: UCEP Baseline Implanted N-type Process

in Figure 2.6 a photo, of one of the baseline implanted N-type cells developed. The design features a CZ-grown N-type substrate which is textured on both surfaces with random pyramids. Both emitter and rear field are formed by implantation. Passivation is achieved through an oxide-nitride stack, and the contacts are printed and belt-fired.

The process sequence for this baseline cell is shown in Figure 2.7. The front side emitter is formed by implanting boron at a dose of $3 \times 10^{15}\,\mathrm{cm}^{-2}$ and energy of 10 keV, followed by an hour-long anneal at 1000 °C. After a chemical etchback of the emitter, the rear side BSF is formed by implanting phosphorus at a dose of $3.4 \times 10^{15}\,\mathrm{cm}^{-2}$ and energy of 10 keV, followed by a 30 minute oxidation and 25 minute anneal at 840 °C. There is optionally an additional step which replaces the front surface oxide with Al_2O_3 (not shown in the process schematic). The front and rear surfaces are then capped with a PECVD nitride. Contacts are formed by screen-printing and belt-firing metal paste. Fritted aluminum paste is used to form the gridlines on the front surface, and fritted silver paste is used for the rear side dot-array contact. Lastly, an unfritted silver paste is printed on the rear side and dried at low temperature to form the back side reflector [20].

These N-type cells demonstrated published efficiencies in the neighborhood of 19.3%, with V_{oc} of 646 mV. A breakdown of the J_o losses for the cell structure indicates that of a total of $J_o = 690\,\mathrm{fA/cm^2}$, the rear surface accounts for $J_{ob} = 130\,\mathrm{fA/cm^2}$ [20, 26]. Prototype cells developed since then have exhibited higher efficiencies in the 19.8% range. These high efficiency cells have been used to calibrate the simulation model developed in this work, as discussed in Section 4.3.

2.3.4 Patterned Ion Implant Concept

In the microelectronics industry, patterned implants may be achieved by photolithographically defining openings in an implant-resistant material such as silicon nitride. For considerations of cost efficiency in the solar cell industry, however, photolithography is far from ideal. There have been a few studies in literature to date examining the potential for patterned ion implantation of solar cells via use of hard masks. These reusable hard masks are placed on the wafer surface prior to implantation, and limit the implanted ions only to certain regions without the need for photolithography.

Dube et al. recently investigated the use of a reusable hard mask with a line-array pattern to form a selective emitter on a P-type solar cell. The hard mask limits phosphorus implantation to thin strip-shaped regions on the front side of the wafer. Following implant, the wafers are then subject to an oxidation and anneal process. The different oxidation rates between doped and undoped silicon creates visual contrast between doped and undoped regions of the wafer, allowing for alignment of the screen printed front grid [34]. The maximum cell efficiency realized in the study is 18.9% [35].

Bateman et al. have utilized a photoresist-based method to create selectively doped regions for an interdigitated back contact (IBC) cell. Instead of a hard mask, photolithographically defined regions are etched in a layer of photoresist, which serves as the implant mask. It is argued that the process can be reproduced using hard masks without the need for photolithography in a production scenario. In their study, 20.0% efficient IBC cells were created utilizing an Al_2O_3 passivated rear side [27].

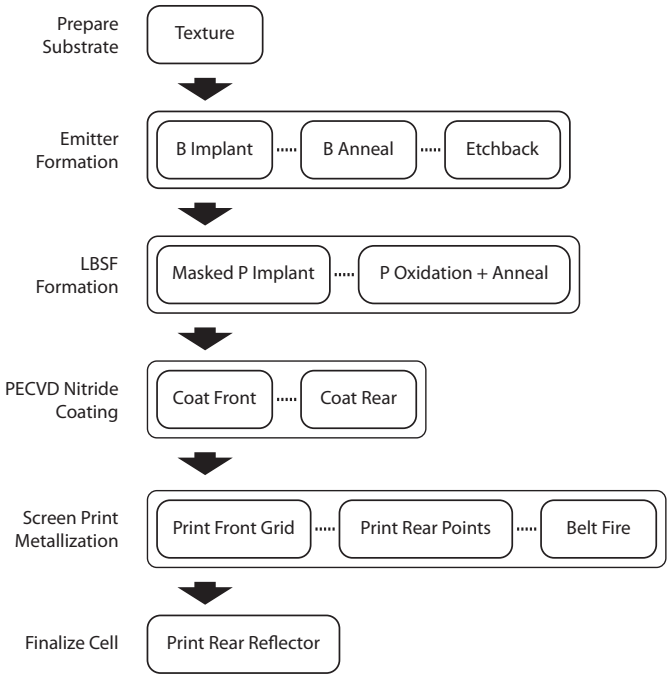

Figure 2.8: Concept Implanted N-type LBSF Process Utilizing Implant Masking

Patterned implant methods for solar cells are only just starting to appear in literature, but the above examples already indicate promise for the formation of high efficiency structures. The current study seeks to extend the use of patterned solar cell implantation to the formation of LBSF structures on N-type substrates. A conceptual process flow for such a cell is shown in Figure 2.8. This process would not require any additional steps beyond the baseline implanted N-type process discussed earlier. The only difference lies in replacement of the phosphorus implant step with a patterned phosphorus implant step, which is achieved using a hard mask.

A procedure is developed in this study to fabricate proof-of-concept implanted LBSF cells, discussed further in Chapter 5. Although it makes use of photolithographically defined implant masks, it is hoped that the process is transferable to hard mask technology, in order to progress toward the simpler concept process shown in Figure 2.8.

2.4 Solar Cell Modeling

2.4.1 Solar Cell Electrical Modeling

Modeling has maintained a role in the development of new solar cell technologies since the 1980's. Popular device modeling software in PV research include PC1D and Sentaurus Device, part of Sentaurus TCAD. PC1D is often used because of its speed and robust numerical convergence. It is, however, slowly falling out of favor as the simulator of choice for advanced solar cells because it is limited to the 1D domain, and it utilizes Boltzmann instead of Fermi-Dirac carrier statistics. Especially in the high doping or high injection regimes, Boltzmann statistics become inaccurate for modeling solar cell behavior. Sentaurus Device, on the other hand, includes Fermi-Dirac statistics, as well as support for the most recent semiconductor electrical models, including the Scharfetter SRH model, Dziewior and Schmid's Auger recombination model, and the Schenk band gap narrowing model [36, 37]. It is also capable of working with full 2D and 3D simulation domains. Sentaurus Device will be discussed more in depth in Chapter 4.

2.4.2 Solar Cell Process Modeling

Sentaurus TCAD also includes Sentaurus Process, a module for simulating diffusion, oxidation, and ion implantation, among other wafer processing events. The Sentaurus Process module has been used in the microelectronics industry for optimizing process parameters for ion implantation and anneals for IC fabrication, and is a prime candidate for modeling the same for solar cells. Sentaurus is designed as a unified simulation environment, in which the results from Sentaurus Process can be fed directly as input into Sentaurus Device or interact with any number the other TCAD simulation, support, and visualization modules. Three tools in the Sentaurus TCAD package are used in the current work: Sentaurus Process for modeling implant and anneal process, Sentaurus Structure Editor for creating geometry and meshes for 3D simulation, and Sentaurus Device for simulating the electrical characteristics of the solar cell. The tools are linked together using the Sentaurus Workbench software

[38, 39, 40, 37, 41]. Portions of this study utilize the 201012 version of Sentaurus TCAD, and others the 201206 version.

2.4.3 Electrical Simulation of Delta-Star Structure

Meemongkolkiat in 2008 developed a Sentaurus Device model of the Delta-Star solar cell structure, which in many ways serves as the intellectual predecessor of the current effort. The model consists of a unit cell for a highly simplified Delta-Star structure. The structure definition consists of a single cuboid with one quarter of an LBSF dot on the bottom, a full metal contact covering the top, and doped regions approximated by analytical doping profiles. The results, however, offered significant insights into the performance of the cell as a function of LBSF geometry, something which could not be accomplished using a 1D simulator like PC1D [42].

The simulations explored the effects of changing LBSF dot size and pitch, as well as the contribution of surface recombination velocity to cell performance. It also revealed that using metal contact points of the same size as the locally diffused regions leads to parasitic shunting around the edges of the contacts. For this reason, it is advantageous for the doped regions of the LBSF to slightly "overhang" the metal points which make contact to them. The optimal geometry identified by the model has been successfully tested in real Delta-Star cells, and has proven accurate in predicting the performance trends seen as a function of geometry and surface passivation quality [22].

Chapter 3

Task I - Implant and Anneal Model Development and Validation

As mentioned previously, the Sentaurus Process module can be used to simulate process steps such as ion implantation, annealing, and oxidation. It is used in this work to produce doping profiles for ion implanted solar cells as input for Sentaurus Device electrical simulation. Maintaining an accurate model of implant and annealing behavior is necessary for optimization of those processes in order to reach high cell efficiencies. Process simulation can also recover information otherwise difficult to measure in an actual cell, such as inactive dopant concentration and diffusion characteristics. In the course of this work, all process modeling for doping profiles has been conducted in the 1D simulation domain.

Five sections are covered in this chapter. The first section is dedicated to describing the Monte Carlo implant model used in this study, as well as the options applied. The second and third sections describe the boron anneal models used in this study, and discuss validation of simulated boron profiles to experimental data. The fourth and fifth sections describe the phosphorus anneal models, and discuss their corresponding validation to experimental data.

3.1 Use of Monte Carlo Implant Model

There are a number of ion implant models built into Sentaurus which the user may choose from. A number of these are analytical models, which express the probability distribution for particle penetration depth as an analytical function with a few fitting parameters. There are also two Monte Carlo models available. These track individual dopant ions as they enter the substrate, interact with stationary atoms, and then eventually come to a rest. Of course, the Monte Carlo methods are ill suited to tracking all dopant atoms which are introduced during a typical implant. Instead, a smaller number of "pseudoparticles" are simulated, each of which represents a large number of actual dopant atoms. Of the two Monte Carlo models, the Sentaurus MC model is used in this work because it is capable of running in a multi-threaded fashion.

Sentaurus MC models ion implantation as a series of collisions between the dopant nucleus and crystal nuclei via the the classical binary scattering model. Each collision event reduces the kinetic energy of the incident nucleus by a factor of

$$\frac{\Delta E}{E_0} \propto \frac{4M_1M_2}{(M_1+M_2)^2}, \tag{3.1}$$

where M_1 and M_2 are masses of the incident and target nuclei respectively. The angle at which the particle is then deflected is given by

$$\cos\theta = \frac{1-0.5\left(1+\frac{M_2}{M_1}\right)\frac{\Delta E}{E_0}}{\sqrt{1-\frac{\Delta E}{E_0}}}. \tag{3.2}$$

This simple collision model, however, does not provide an closed form solution for the energy loss and deflection angle, because the Coulomb potential term which appears in the full expression for $\frac{\Delta E}{E_0}$ cannot be evaluated analytically. In addition, the implanted ions feel both local and nonlocal Coulomb effects which retard their motion. For these reasons, Monte Carlo methods must be used to capture the full physical behavior of ion implanted particles [38].

The Sentaurus MC model also accounts for atom knock-out effect, in which a collision with sufficient energy knocks out a silicon atom from its lattice, generating a vacancy and a self-interstitial. These self-interstitials influence the subsequent dopant diffusion during annealing steps, as discussed in Section 3.2 and Section 3.4. Additional options used in this work for implant modeling include the "cascades" flag, which prompts Sentaurus MC to track the trajectories of all knocked-out silicon atoms, and perform binary collision modeling on them as well. This provides a more complete picture of the interstitial and vacancy concentration in the substrate after implantation is complete.

Sentaurus MC can accommodate implant simulation in various crystal types and orientations. For this study, we specify a zincblende crystal structure, corresponding to monocrystalline silicon, and [1 1 1] crystal orientation on the exposed surface, corresponding to the face of a random texturing pyramid. It is noted that changing the crystal orientation does not seem to significantly affect the post-anneal doping profile.

3.1.1 Dependence of Monte Carlo Implant Results on Pseudoparticles Implanted

The accuracy of the results provided by the Monte Carlo simulation is dependent on the number of pseudoparticles simulated. In this work, 1000 pseudoparticles are used to model the phosphorus and boron implants. A 1000 pseudoparticle implant creates a rather jagged implant profile of dopant atoms, but after the anneal simulation, these profiles become completely smooth. It has been found that for the annealing conditions of interest, increasing the number of pseudoparticles above 1000 does not appreciably affect the final doping profile. It should be noted, however, that if significantly shorter annealing times are used, more pseudoparticles may be necessary to obtain a smoother doping profile.

The smoothness of the implant profile also affects the behavior of oxidation simulation. Thermal oxidation is modeled in Sentaurus like its physical counterpart - the oxidized layer penetrates into the silicon region as it grows both inward and outward. The oxidation rate depends on the doping level present at the surface of the silicon, and incontinuities in this

doping level (such as those created by Monte Carlo implant) seem to present convergence problems for the simulator.

In order to simulate thermal processes which begin with oxidation, then, this study utilizes a short anneal in nitrogen ambient prior to the oxidation step. This ensures that the dopant concentration is adequately smooth for the oxidation simulation to proceed. For example, post implant phosphorus anneals studied in this work commonly utilize a 30 minute oxidation at 840 °C in a dry oxygen ambient, followed by a 25 minute anneal at 840 °C in a nitrogen ambient. For simulation purposes, we insert a 6 minute anneal at 840 °C in nitrogen ambient prior to the oxidation step, and decrease the post oxidation anneal to 19 minutes in order to keep the overall thermal budget constant. Sentaurus also provides an implant profile smoothing function, but this feature was not used in the present study.

3.1.2 Determination of the Effect of Texturing Angle on Implant Dose

Texturing of the surface of silicon wafers prior to ion implantation changes the effective dose received at the surface. For a perfectly directional flux of dopant ions into a face of a texture pyramid, the dose implanted into the surface falls off as $\cos\theta$, where θ is the angle between the implant vector and the line normal to the pyramid face's surface. Thus, there are two ways of adjusting the implant dose to reproduce this angle effect. One way is to decrease the dose by a factor of $\cos\theta$, and the other would be to model the implant as occurring at an angle of θ off normal from the substrate surface. The current study uses largely the latter method with $\theta = 54\,^\circ$, corresponding to the typical angle seen in texturing pyramids. In actual implantation, the wafer may be tilted by $5-7\,^\circ$ to reduce the effect of channeling, but the $\cos\theta$ loss in this case is very small, and the dose lost by pyramid faces pointed away from the implant is gained by those pointed toward the implant.

3.2 Theory and Implementation of Boron Anneal Models

Simulation of the thermal annealing and oxidation of boron is a non-trivial task. The diffusion of boron in silicon has been studied heavily by the microelectronics research community, and elucidating reviews of important results are given in Shao et al., Jain et al., and Stolk et al. [43, 44, 45]. The Sentaurus AdvancedModels package combines a number of models to explain unique features of the boron anneal process, including diffusion characteristics, defect cluster evolution, and dose loss. One section is dedicated to each phenomenon. Formation of a "boron rich layer" is an additional phenomenon seen in solar cells fabricated at the UCEP, and is discussed in the last section.

3.2.1 Boron Diffusion Characteristics

Boron diffusivity is dependent on temperature, but also on the concentration of silicon self-interstitials. Ion implantation and oxidation are two processes which generate large numbers of self-interstitials, and the interstitial supersaturation results in anomalous fast diffusion of boron during the early stages of anneal. The phenomena, called transient enhanced diffusion (TED) and oxidation enhanced diffusion (OED), need to be properly modeled in order to achieve the correct doping profile with anneal simulation. TED and OED are accounted for by user selectable models which are part of the AdvancedModels package in Sentaurus Process. These models, which track the escape of self-interstitials from clusters and extended defects, are calibrated to TEM measurements of extended defect evolution [46].

The Sentaurus package AdvancedCalibration is also activated for simulations in this study. This package contains a group of self consistent diffusion models and experimentally calibrated parameters, which allow for use of the AdvancedModels package.

3.2.2 Boron Interstitial Cluster Evolution

Boron atoms can interact chemically with silicon self-interstitials, forming boron-interstitial clusters (BICs) of various stoichiometries. The time evolution and dynamics of BICs is

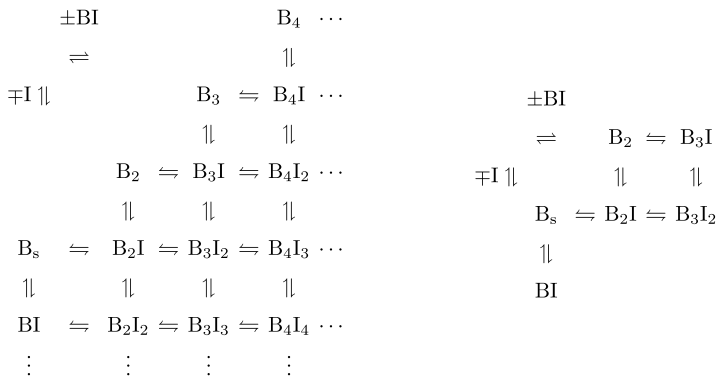

Figure 3.1: Reaction Schematics of BIC Evolution [5]

a complex study. BICs may transform into clusters of other stoichiometries (shown in Figure 3.1a) or even extended defects as they interact with boron and interstitial atoms [47, 48, 32]. In this study, we use a modern numerical model developed by Ortiz, Pichler, and Schermer, which is specifically designed for computational efficiency [49, 50, 5]. This model tracks evolution among only a small subset of the most important BIC species, shown in Figure 3.1b. Reaction rate constants and activation energies for this model are calibrated to experimentally measured profiles.

The trapping of boron in these BICs plays a major role in the electrical activation of implanted boron dopants. BICs are electrically inactive, and also serve as recombination centers for carriers [30, 31]. In order to make a high efficiency electrical device such as a solar cell, these BICs must be dissolved, and the free boron atoms integrated into the silicon lattice. This is accomplished most easily by means of a high temperature anneal in an ambient which does not inject additional self-interstitials, such as nitrogen [48]. The need to dissolve the BICs and activate the boron atoms, however, must be balanced with the limitations of thermal budget on the wafer. It has been shown that exposing a silicon wafer to high temperatures for long periods of time degrades its bulk lifetime [20].

In this study, in order to quantify the activation quality of dopants (including boron and

phosphorus), we use an activation factor f_{active} which we define as follows:

$$f_{active} \equiv \log_{10}\left(\frac{N_{active}}{N_{inactive}}\right), \tag{3.3}$$

where N_{active} is the number of active dopant atoms and $N_{inactive}$ the number of inactive dopant atoms, each resulting from integration across the entire doping concentration profile. For instance, a value $f_{active} = 2$ implies that there are 100 active dopant atoms per 1 inactive dopant atom. In this study, we typically see f_{active} values above 1.5 for diffusions which demonstrate proper electrical performance in the completed solar cell. Quantification of activation quality is a powerful feature of process simulation - for any desired implant condition, one can conduct simulations to find the anneal conditions required to guarantee electrical activation of the dopants.

3.2.3 Boron Boundary Conditions and Dose Loss

During the oxidation process, preferential diffusion of boron from the silicon into the oxide layer is a well known phenomenon. To first order, this behavior may be approximated by the two phase segregation model, in which a segregation coefficient describes the equilibrium difference in concentration of boron in oxide and boron in silicon [29]. A three phase model developed by Oh and Ward, however, has demonstrated to yield more accurate simulated profiles, and is used for the process simulations in the current study. This three-phase model considers the interface region between silicon and oxide to be a third phase which can either transfer dopant atoms with silicon, transfer them with oxide, or capture them in a fixed density of interface traps [51]. The interface trap density can be adjusted in order to fine tune the shape of the doping profile and the value of the sheet resistance to better match experimentally measured values. For the purposes of this study, no calibration was deemed necessary after comparison to experimental data in Section 3.3.2.

3.2.4 Notes on Formation of the Boron Rich Layer

A number of different doping methods (including ion implantation) are capable to creating a thin layer on the silicon surface which is rich in inactive dopant atoms, segregated impurities, and crystal defects. Known as the boron rich layer (BRL), it is a major source of recombination centers for minority carriers, and its presence severely degrades the performance of the device. It has been demonstrated that the BRL can be removed by a chemical etch, which recovers the surface quality of a boron doped surface [52]. The need for BRL removal, however, creates complications in the development of a boron-phosphorus co-anneal process, because removal of the BRL also removes the thermally grown oxide which is required for surface passivation in the device. Although not explored in the current work, it is possible that BRL formation may be observed in simulation by tracking the movement of inactive boron atoms to the silicon surface, and monitoring how interface traps in the three-phase segregation model are filled.

3.3 Validation of Boron Anneal Simulation

3.3.1 Boron Activation and Clustering Validation

One of the first models developed for the current study seeks to reproduce results from literature in order to demonstrate successful boron activation modeling. In a study by Pawlak et al., simulations were written to model implanted boron profiles for a back-junction solar cell. It was found that boron implant doses greater than $5 \times 10^{14}\,\mathrm{cm}^{-2}$, followed by 10 minute anneals of 1000 °C, result in doping profiles with noticeable quantities of inactive boron in the peaks. These inactive atoms are trapped in BICs, and it is noted that the thermal anneal is not sufficient to fully activate the implanted boron [6].

Our model recreates the conditions used in the Pawlak study, and incorporates the diffusion models of the Sentaurus AdvancedCalibration and AdvancedModels packages, described in previous sections. Implant doses are varied between $1 \times 10^{14}\,\mathrm{cm}^{-2}$ and

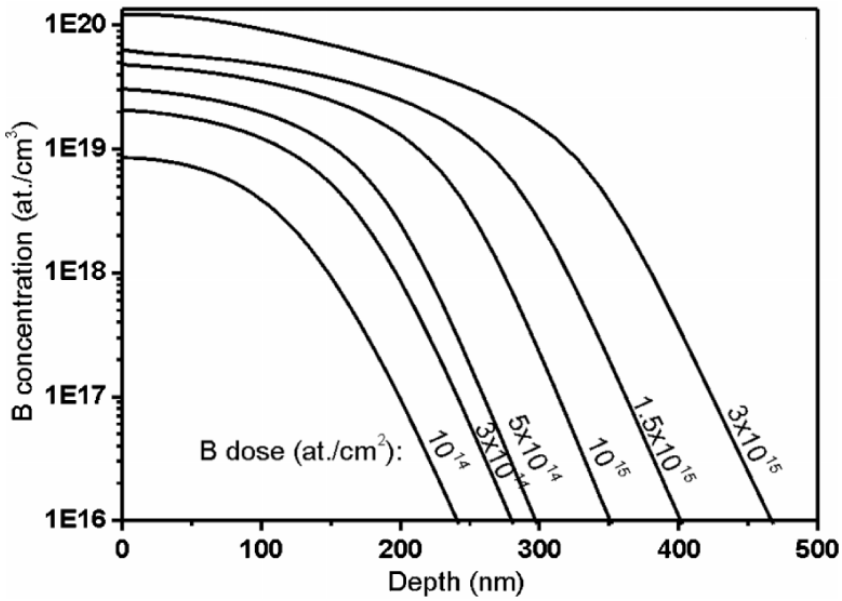

(a) Results from Pawlak et al.

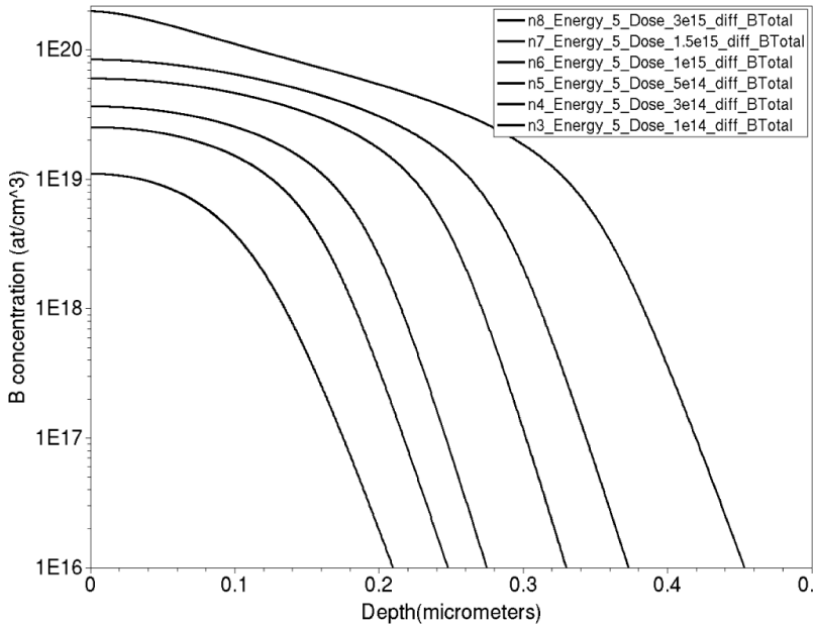

(b) Results from Current Study

Figure 3.2: Boron Implant and Anneal Doping Profile Comparison [6, 7]

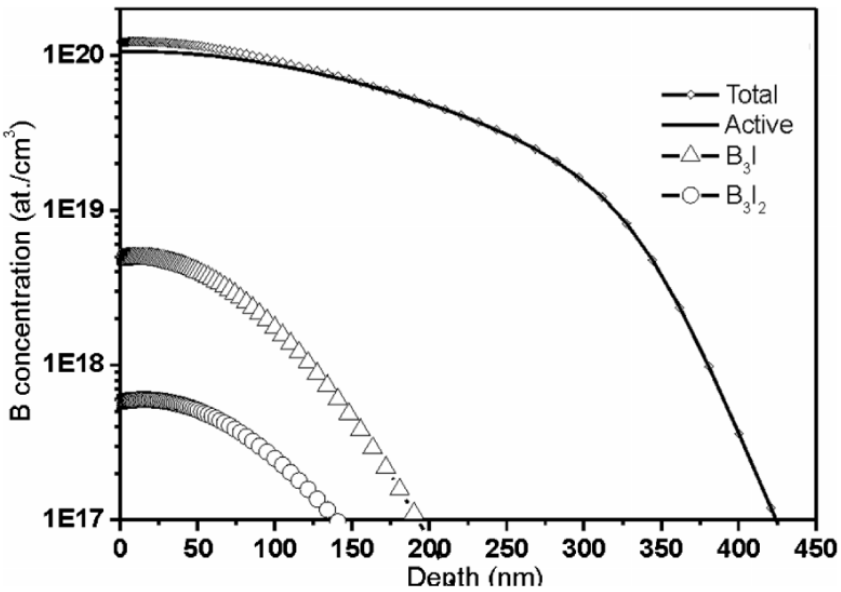

(a) Results from Pawlak et al.

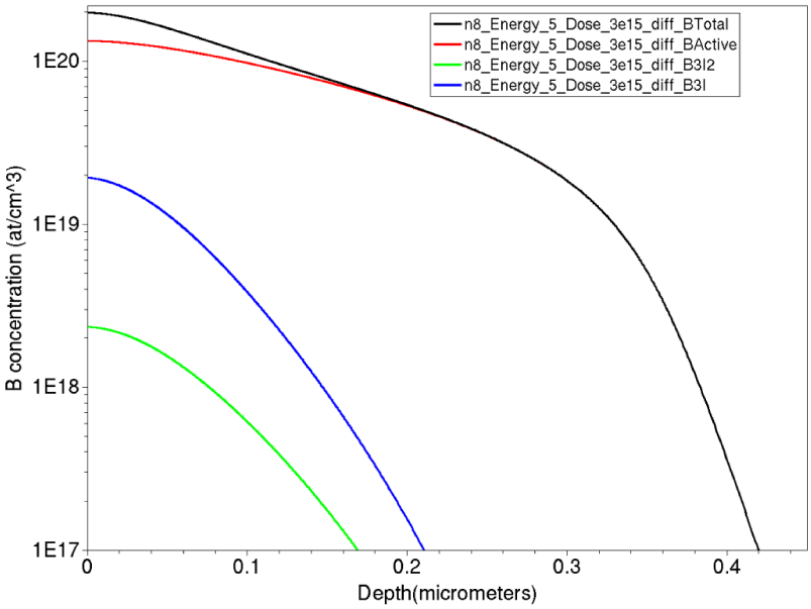

(b) Results from Current Study

Figure 3.3: Boron Implant and Anneal BIC-Cluster Profile Comparison [6, 7]

$3 \times 10^{15}\,\mathrm{cm}^{-2}$ at an energy of 5 keV, and the anneal is simulated for 10 minutes at 1000 °C. As seen in Figure 3.2, the resulting doping profiles are a good match to those presented in the Pawlak study. Figure 3.3 is a comparison of the profiles for representative BIC species B_3I and B_3I_2, as well as total boron and active boron, at a single implant dose $3 \times 10^{15}\,\mathrm{cm}^{-2}$. These profiles are also a reasonably good match, with the exception of slightly higher concentrations of active boron and BICs near the surface. It has been pointed out the these discrepancies might be due to the different versions of Sentaurus used between the two studies [7]. It should be also noted that although Sentaurus is capable of modeling temperature ramp up and ramp down during annealing, the current study uses only constant temperature anneal steps.

3.3.2 Boron Doping Profile Validation

During development of the baseline ion-implanted solar cell at the UCEP, many implanted and annealed samples were characterized by electrochemical capacitance-voltage (ECV) measurements. The ECV method records electrically active dopant concentration as a function of depth in a silicon wafer. To do so, the surface of the wafer is slowly etched by an electrolyte, while a potential is induced between the bottom of the silicon sample and the top of the electrolyte. With an electrolyte of sufficient concentration, charge transfer is limited by the carriers available in the doped region in the sample. The voltage-current characteristics of this effective electrochemical capacitor yields information about the dopant concentration, and the gradual etch allows for the reconstruction of doping as a function of depth [53].

Only recently, however, has the ECV method been used to successfully characterize the doping profile of textured solar cell wafers. This is due to the fact that the measurement is sensitively dependent on knowledge of the surface area of the sample being etched. The surface area of a textured solar cell is difficult to measure, and a number of compensation techniques have recently been developed [54, 55].

At the UCEP, textured wafers from experimental batch **BR-21** were implanted with boron,

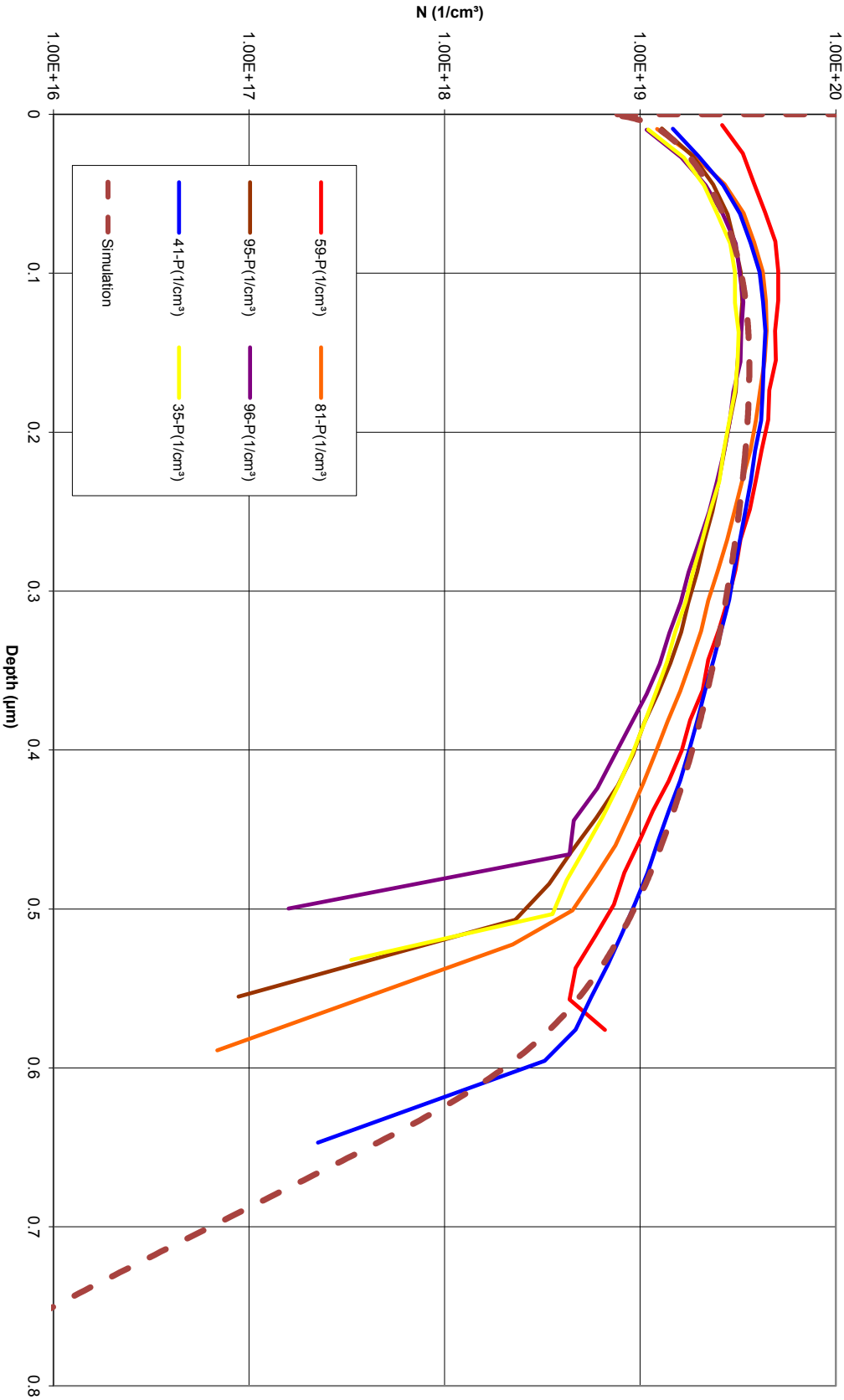

Figure 3.4: Boron Implant-Anneal Simulation vs. ECV Data

annealed, and subsequently characterized by ECV in 2010. It is currently unknown which area compensation techniques were used in the ECV measurement. The wafers received a dose of $3 \times 10^{15}\,\mathrm{cm}^{-2}$ at 10 keV, and an anneal for 1 hour at 1000 °C in nitrogen, followed by 2 hours at 840 °C in oxygen. The current study recreated these processing parameters in Sentaurus, in a model named **Boron1**, and compared the results to the ECV measurements. In Figure 3.4, we can see that the simulated profile (dashed line) tends toward the deep side, but overall is within the range of the profile variations for the wafers measured. Compared to the deepest ECV profile, the simulation gives a sheet resistance of 76 Ω/□, and 4-point probe measurement of the sample yields 77 Ω/□. Interestingly, the ECV measured sheet resistance for this sample is 72 Ω/□. The reason for this discrepancy is unknown, but this sheet resistance mismatch is also seen in phosphorus profiles discussed in Section 3.5.1.

3.4 Theory and Implementation of Phosphorus Anneal Models

As in the case of boron, Sentaurus AdvancedModels simulates phosphorus anneal using models which account for separable phenomena. General diffusion characteristics and dose loss are described below.

3.4.1 Phosphorus Diffusion Characteristics

Recent studies have indicated that phosphorus diffuses via a combination of vacancy mediated and kick-out diffusion processes. Diffused phosphorus profiles exhibit a well-known plateau at shallow depths, followed by a kink and gradual fall-off at greater depths. A model developed by Uematsu in 1997 suggests that this effect is caused by vacancy mediated diffusion dominating in the shallow regime and the kick-out process dominating in the deep regime. This can be seen in corresponding high concentrations of self-interstitials in the shallow regions and of phosphorus interstitials in the deeper regions [56].

In the Sentaurus implementation of phosphorus diffusion, these two regimes are handled by separate numerical terms describing phosphorus-vacancy (P-V) pair diffusion and phosphorus-interstitial (P-I) pair diffusion [38]. The P-V diffusion term predominantly affects the shallow region, in which phosphorus concentrations are high. In addition, Sentaurus tracks the diffusivity behavior of P-I and P-V pairs of different charges using the "ChargedReact" switch, which is activated for the current study. The AdvancedCalibration package is used to provide calibrated parameters for this model.

Although parameters for phosphorus diffusivity have been well calibrated for IC work in Sentaurus, there remain inconsistencies between phosphorus profile simulations in Sentaurus and ECV measured profiles on textured solar cell wafers. These discrepancies will be discussed in Section 3.5.1.

3.4.2 Phosphorus Boundary Conditions and Dose Loss

Phosphorus exhibits the opposite oxide segregation behavior from boron [57]. At equilibrium, the concentration of phosphorus in silicon is higher than that in oxide. Thus, the phosphorus doping profile of wafers having undergone oxidation often features a small peak at the interface. This peak is theoretically separate from the plateau created by the vacancy-mediated diffusion in the shallow regime. In practice, however, it is often hard to tell the difference in a measured phosphorus profile, especially when the surface phosphorus dose is lower than $1 \times 10^{20}\,\mathrm{cm}^{-3}$.

As in the case of boron, phosphorus dose loss is accounted for in Sentaurus by the three-phase segregation model. The segregation behavior can be fine tuned by modification of the interface trap density. Tuning has not been performed in this study since larger uncertainties remain in the doping profile shape.

Table 3.1: Phosphorus Simulation and ECV Sheet Resistance Comparison

Energy (keV)	**Dose** (cm^{-2})	**4-pt** R_{sh} ($\Omega/\square$)	**Sim** R_{sh} ($\Omega/\square$)	**ECV** R_{sh} ($\Omega/\square$)
5	1.2×10^{15}	162	171	481
	2.4×10^{15}	98	98	151
	3.6×10^{15}	73	67	103
	4.8×10^{15}	61	48	85
10	1.2×10^{15}	145	161	367
	2.4×10^{15}	84	90	116
	3.6×10^{15}	64	62	84
	4.8×10^{15}	55	46	70
20	1.2×10^{15}	130	147	286
	2.4×10^{15}	77	85	99
	3.6×10^{15}	58	58	74
	4.8×10^{15}	51	44	62
30	1.2×10^{15}	122	144	185
	2.4×10^{15}	73	83	81
	3.6×10^{15}	54	56	61
	4.8×10^{15}	48	43	52

3.5 Validation of Phosphorus Anneal Simulation

3.5.1 ECV and Simulated Doping Profile Comparison

The simulation **Phos3** was conducted to determine the accuracy of simulated phosphorus doping profiles compared with those measured using ECV. The experimental wafers originated from an earlier Suniva study in which implant doses ranged from $1.2 \times 10^{15}\,cm^{-2}$ to $4.8 \times 10^{15}\,cm^{-2}$ at energies from 5 keV to 30 keV. The wafers were subject to a 30 minute oxidation at 840 °C in a dry oxygen ambient, followed by a 25 minute anneal at 840 °C in a nitrogen ambient.

Shown in Table 3.1 are values for the experimentally measured 4-point probe and ECV sheet resistances, as well as the simulated sheet resistances. There are large inconsistencies between the sheet resistance values extracted from ECV and the sheet resistance values from 4-point probe measurement. The cause for this is still unknown. The simulated sheet resistances are closer to the 4-point probe values, but err both high and low depending on the implanted dose. Shown in Figure 3.5 is a comparison of the simulated and measured

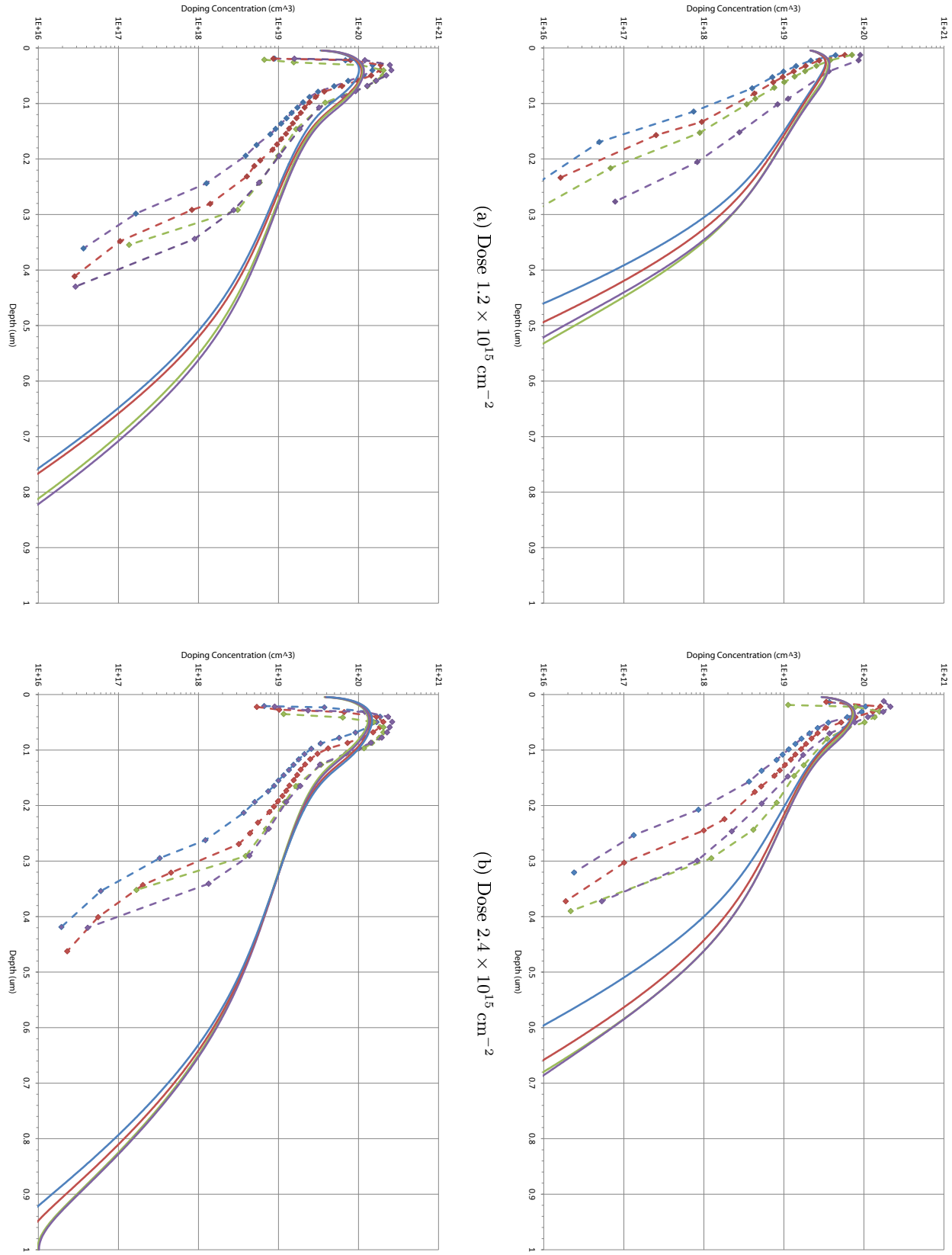

(a) Dose 1.2×10^{15} cm^{-2}

(b) Dose 2.4×10^{15} cm^{-2}

(c) Dose 3.6×10^{15} cm^{-2}

(d) Dose 4.8×10^{15} cm^{-2}

Figure 3.5: Phosphorus Implant-Anneal Simulation vs. ECV Data (Diffusivity Factor 1.0)

Table 3.2: Adjusted Phosphorus Simulation and ECV Sheet Resistance Comparison

Energy (keV)	**Dose** (cm^{-2})	**4-pt** R_{sh} ($\Omega/\square$)	**Sim** R_{sh} ($\Omega/\square$)	**ECV** R_{sh} ($\Omega/\square$)
5	1.2×10^{15}	162	230	481
	2.4×10^{15}	98	120	151
	3.6×10^{15}	73	81	103
	4.8×10^{15}	61	57	85
10	1.2×10^{15}	145	209	367
	2.4×10^{15}	84	110	116
	3.6×10^{15}	64	73	84
	4.8×10^{15}	55	55	70
20	1.2×10^{15}	130	182	286
	2.4×10^{15}	77	102	99
	3.6×10^{15}	58	68	74
	4.8×10^{15}	51	51	62
30	1.2×10^{15}	122	172	185
	2.4×10^{15}	73	97	81
	3.6×10^{15}	54	64	61
	4.8×10^{15}	48	49	52

doping profiles, organized by implant dose. The solid curves represent simulation, and the dashed curves ECV measurement. For a given dose, shallower profiles represent low implant energy and deeper ones higher implant energy, ranging from 5 keV to 30 keV. It is noted that the simulated profiles are deeper in all cases than the ECV profiles by roughly a factor of 2.

In order to match the shapes of the ECV profiles more closely, a followup simulation **Phos4** was conducted. This simulation implements a user-definable prefactor in the phosphorus-interstitial and phosphorus-vacancy diffusion terms. It is found that a prefactor of 0.35 provides a reasonable match to the shapes of the ECV profiles, as shown in Figure 3.6, but the sheet resistances between simulation and 4-point measurement no longer match. This prefactor has no physical basis, and right now serves only as a fitting factor. A more careful study of phosphorus diffusion under these conditions should be conducted to determine how best to model the behavior. For this study, device simulation will be conducted with phosphorus diffusivity unchanged from the default model (prefactor of 1).

One cannot rule out the possibility that the ECV measured profiles are not accurate repre-

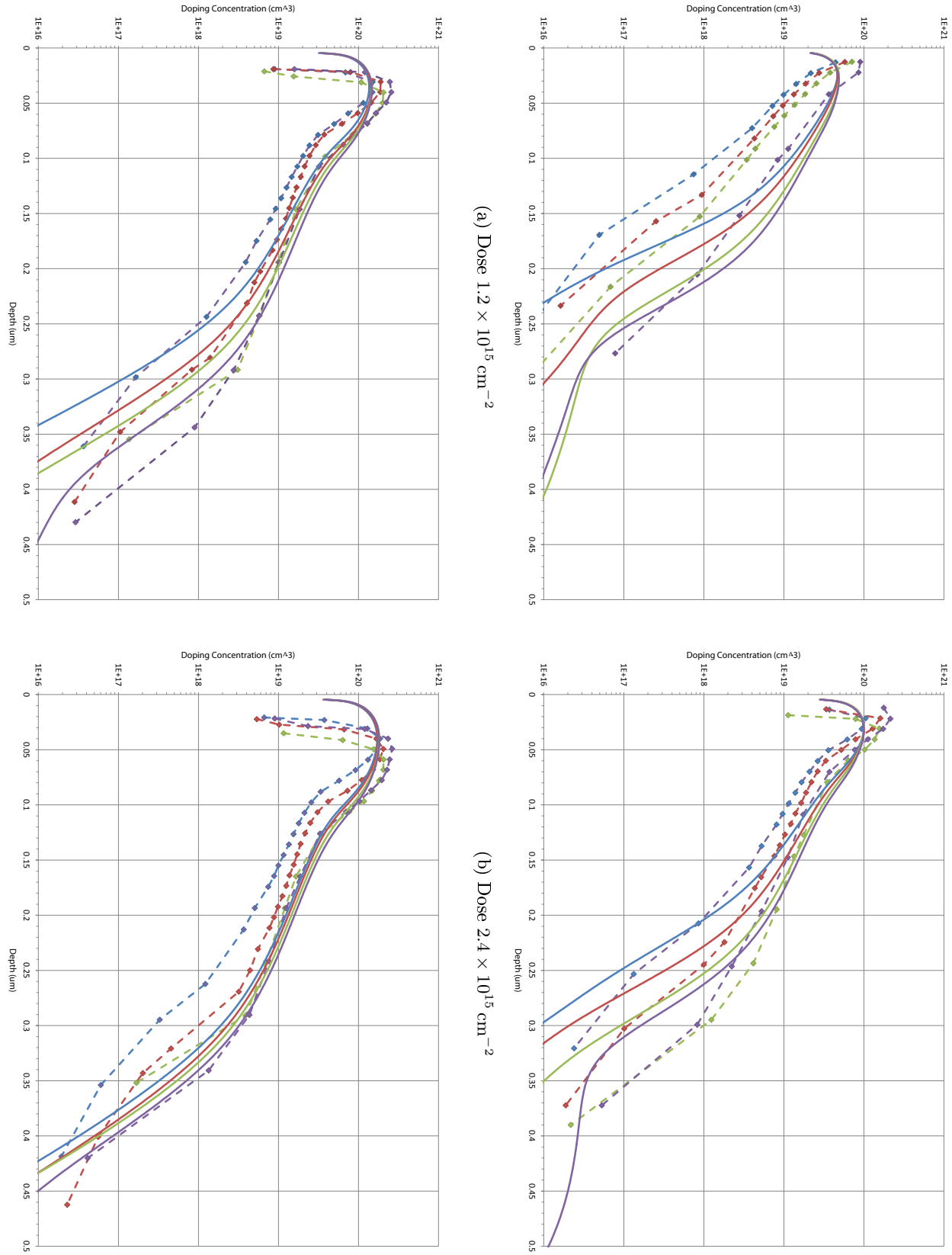

(a) Dose 1.2×10^{15} cm^{-2}

(b) Dose 2.4×10^{15} cm^{-2}

(c) Dose 3.6×10^{15} cm^{-2}

(d) Dose 4.8×10^{15} cm^{-2}

Figure 3.6: Phosphorus Implant-Anneal Simulation vs. ECV Data (Diffusivity Factor 0.35)

sentations of the actual doping profiles. In order to investigate this possibility, measurements on planar wafers may be conducted using alternative measurement methods such as SIMS. In order to extract the profile from a textured wafer, however ECV remains the only method to date. It is suggested that new ECV measurements be conducted with more carefully calibrated area correction factors.

3.5.2 Phosphorus Activation vs. Boron Activation

In general, phosphorus is easier to electrically activate than boron since it does not form extended defects with silicon self-interstitials. In the **Young5** simulation in this study for example, boron implant is simulated at a dose of $3 \times 10^{15}\,\mathrm{cm}^{-2}$, followed by thermal anneal at 1000 °C for one hour, oxidation at 840 °C for 30 minutes, and anneal at 840 °C for 25 minutes. The activation factor for boron after this process is $f_{active} = 1.6$. On the other hand, phosphorus implant is simulated in this model at a dose of $3.4 \times 10^{15}\,\mathrm{cm}^{-2}$, followed by oxidation at 840 °C for 30 minutes and anneal at 840 °C for 25 minutes. The activation factor for phosphorus in this case is $f_{active} = 2.9$.

Chapter 4

Task II - Device Model Development and Calibration

Sentaurus Structure Editor is used to algorithmically create the 3D solar cell structure, and Sentaurus Device is used for the subsequent electrical simulation. This chapter discusses how these tools are used in more detail. Once a model is constructed, it is first calibrated to an actual solar cell which is similar to the model. After successful calibration, the model is used to simulate LBSF cells of varying geometries, and to illuminate trends which affect their performance.

4.1 Cell Structure Development

The geometry of the LBSF can be parametrized by a small number of variables: dot width, dot pitch, and dot shape. In addition, the arrangement of the dots can follow a square or hexagonal lattice configuration. In this study, we perform simulations for a square lattice of square dots. Due to the anisotropic nature of carrier flow in an LBSF solar cell, it is necessary to use a fully 3D simulation domain in order to accurately model the electrical behavior of this LBSF structure.

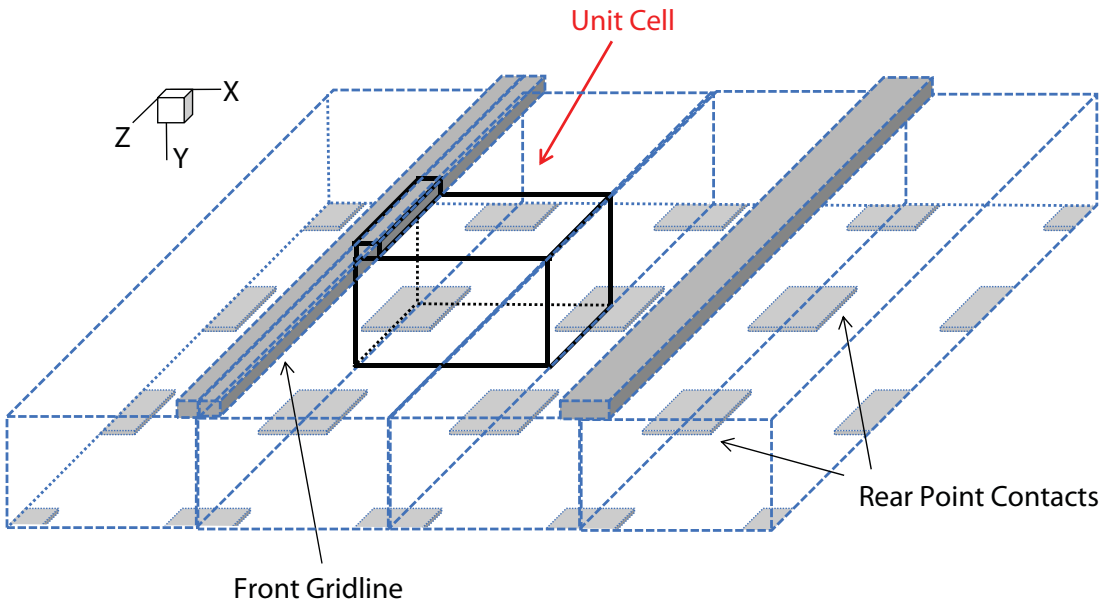

Figure 4.1: Unit Cell Schematic

Synopsys, the company behind Sentaurus, has published an example 3D solar cell model for Sentaurus, along with an application note describing its features [58]. For the current study, we use this example as a starting point for the code, and add to it our own geometry parametrization, optical generation profile, doping profiles, mesh sizes, and electrical models.

4.1.1 Defining the Simulation Unit Cell

Simulation in the 3D domain takes more time than the 1D and 2D domains. We can, however, simplify the problem by reducing the simulation volume down to a small unit cell. As shown in Figure 4.1 and Figure 4.2, the unit cell we use for this study has a width equal to half the separation between two front gridlines, a length equal to half the pitch between rear contact dots, and a variable depth. The unit cell also includes half of a gridline and at least a quarter of a rear contact dot. A full solar cell (less the busbars) may be constructed by tiling this unit cell.

The adjustable geometric parameters in our model include contact dot width, contact dot pitch, LBSF dot width (for defining doped regions larger than their contact dot), grid width, grid pitch, emitter width (for selective emitter modeling), and cell thickness. The bulk region

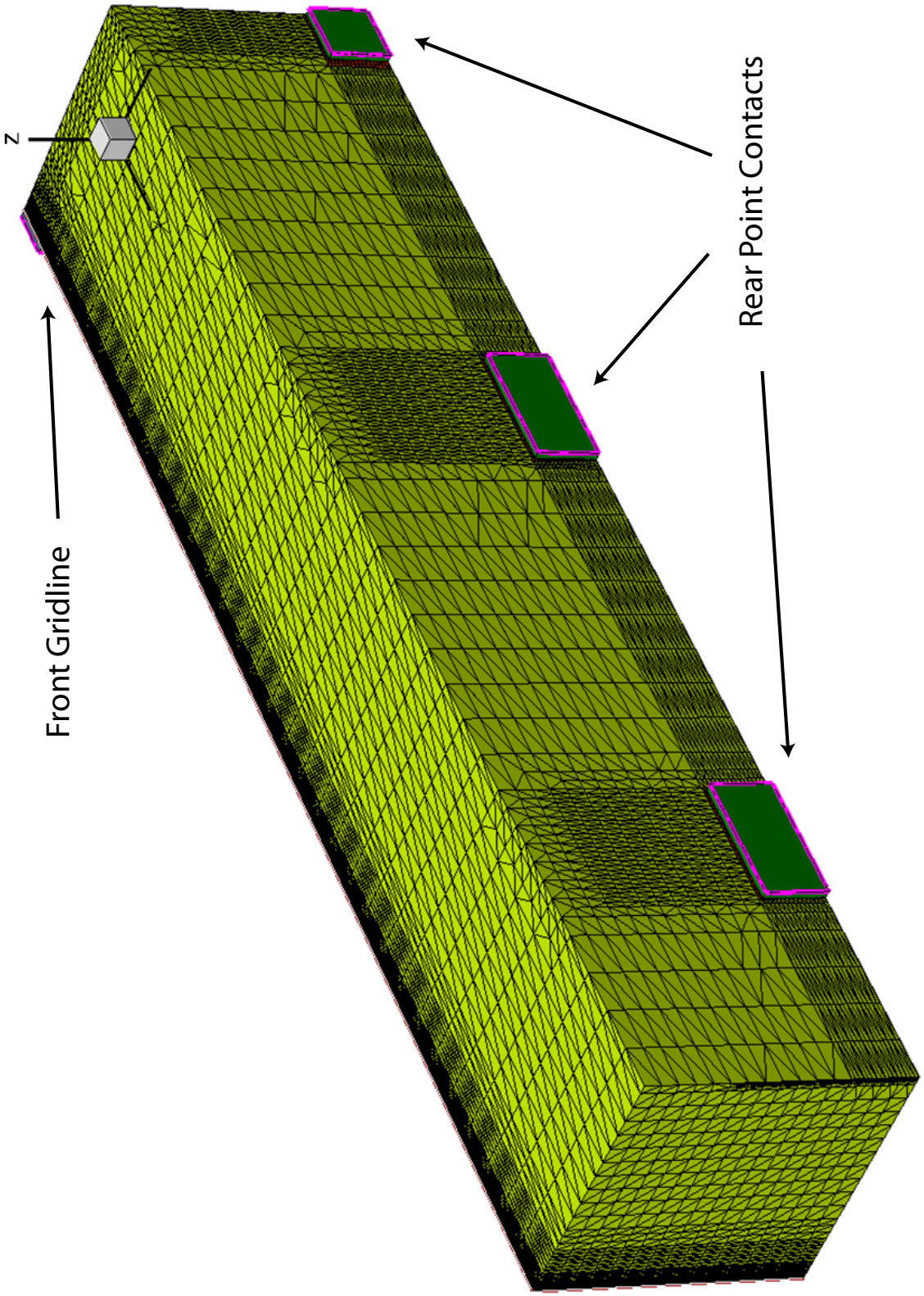

Figure 4.2: Completed Simulation Structure, **Young3** Model

is given a thickness of 200 μm. Sentaurus Structure Editor is used to algorithmically build the unit cell using the user-provided parameters [39]. Passivating dielectric is placed in regions of the surface which are not covered by a metal contact.

It should be noted that in this parametrization, only an integer number of rear contact points may fit between two gridlines, which limits the number of options for rear dot pitch. For the current study, we utilize a gridline spacing of 2110 μm, which allows us to simulate rear dot pitches of 2110, 1055, 703, 528, 422, 352, 301, and 264 μm. The unit cell also does not include geometric definition for the textured surface of the solar cell - light trapping behavior is implemented by tuning the generation profile, as discussed in Section 4.1.2.

There are a number of geometry flags which can be toggled in our model. One can create a BSF which covers the entire rear surface by setting the parameter *bsfWidth* to 0, otherwise this parameter represents the width of the local BSF dot. When a local BSF is present, it is also possible to enable doping in the rear field (areas not covered by the local BSF) by setting *enableRearField* to 1. To disable the local or full BSF entirely, one may set *enableBSF* to 0. Conversely on the front side, a full surface front emitter is applied if *emitterWidth* is set to 0, otherwise this parameter represents the width of the selective emitter. With a selective emitter, a field doping may be enabled by setting *enableFrontField* to 1. Finally, the emitter may be disabled entirely by setting *enableEmitter* to 0.

4.1.2 Implementation of Ray-Traced Generation Profile

The photogeneration of electron-hole pairs as a function of depth in a solar cell is dependent on surface texturing, the optical properties of any anti-reflection coatings, and the intrinsic properties of the silicon material. In addition, rear surface optical features such as texturing and metal reflectors can modify this generation profile. In simulating a solar cell, one must have an accurate generation profile from either experimental measurement or from simulation. For the current study, we make use of a generation profile created at the UCEP which uses a Monte Carlo ray-tracing algorithm to simulate photon absorption, and which

is calibrated to generate results consistent with our surface texturing and anti-reflection coating properties.

Shown in Figure 4.3 is a comparison of the generation profile used for the current study (Sentaurus Ray-Traced), in comparison to the default generation profile provided by Sentaurus and the generation profile created by PC1D. The 3D simulation code published by Sentaurus also has a feature which reflects the tail end of the generation profile and adds it back into the bulk, in order to reproduce the effect of a back surface reflector. In the current study, the rear surface metallization produces reflection of about 93% where metal makes contact to silicon, and 96% where a dielectric is present between metal and silicon. The reflected tail end of the generation profile is derated accordingly in these two regions before being added back into the bulk. The generation profile in the region underneath the front gridline is set to zero.

4.1.3 Integration of Simulated Doping Profiles

The doping profiles generated by the Sentaurus Process simulation are used for electrical device simulation. At the conclusion of each process simulation, the software outputs a file containing the doping profiles for electrically active boron and electrically active phosphorus. These doping profiles are read by Sentaurus Structure Editor, and placed in the unit cell at their corresponding locations. It should be noted that no other doping profiles are carried over from the process simulation - namely, there are no defect profiles or damage profiles inserted into the structure. For the **Young3** model, the profiles are added by hand. Subsequent models read the doping profiles automatically.

ECV profiles may also be used in lieu of simulated profiles, as long as the file format conforms to the standard. Doping profile definition files are of the *.tdr* format, in which each row has an entry for depth and an entry for doping concentration. Entries are delimited by a space character. Different data series are separated by multiple line breaks. The first line of each series is a label indicating the series name. It is noted that Sentaurus Process outputs *.tdr* files in which the series labels conform to the Sentaurus Process naming scheme: i.e. boron

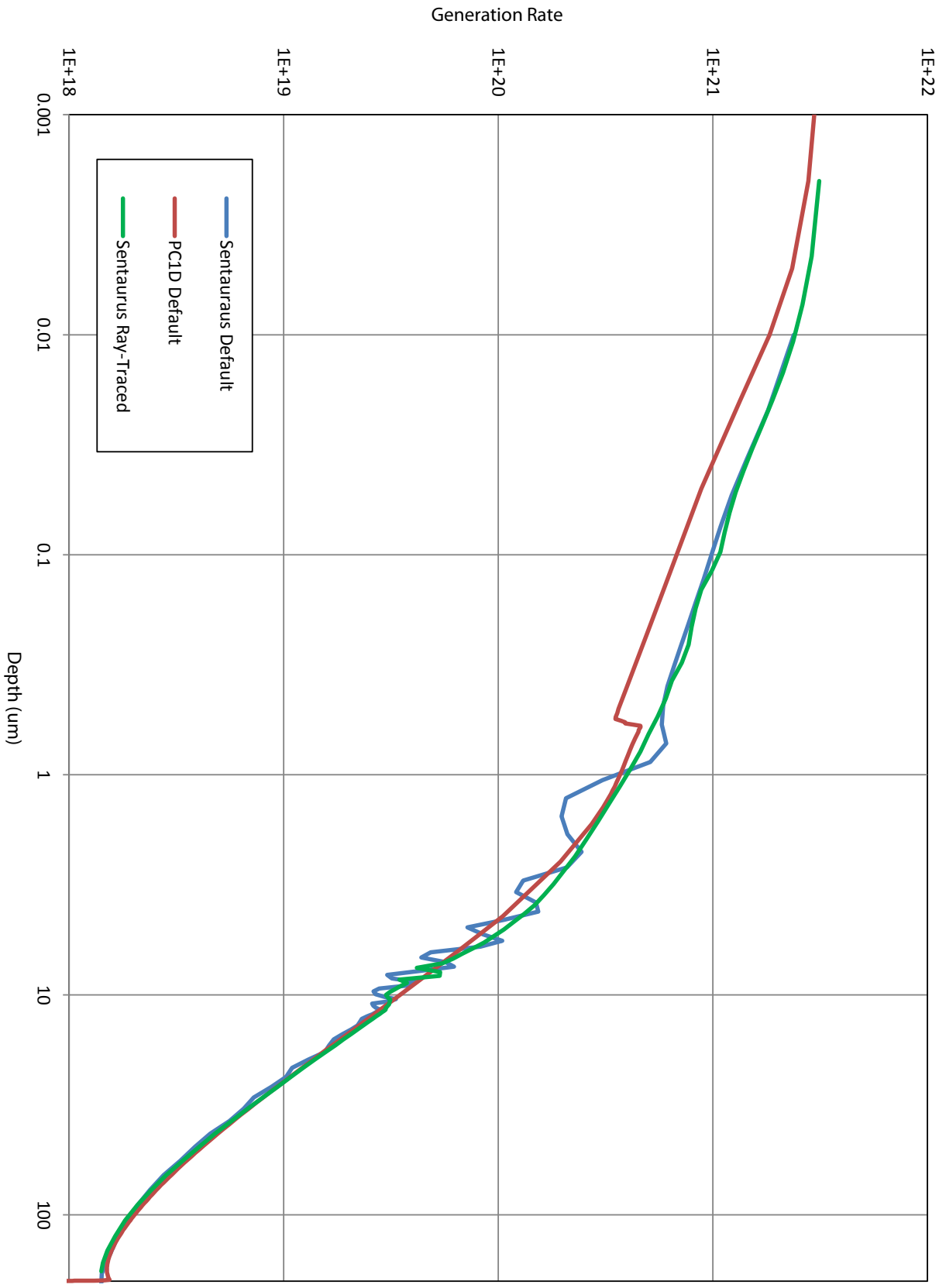

Figure 4.3: Optical Generation Profile Comparison

active concentration is denoted "BActive". Sentaurus Device, however, requires a different naming scheme in which boron active concentration is denoted "BoronActiveConcentration". A helper module is inserted between the Sentaurus Process step and the Sentaurus Structure Editor step in order to make these changes automatically in models **Young4** and **Young5**.

4.1.4 Definition of Metal Contact Structures

Contacts in the model are defined as rectangular prisms which touch the silicon surface. The front surface contact is defined to be aluminum, and the rear contacts silver. The material definition parameters for aluminum and silver are unchanged from the Sentaurus defaults.

4.1.5 Simulation Domain Meshing

After the structure has been defined in Sentaurus Structure Editor, all regions in the simulation must be meshed. The meshing process discretizes the simulation regions into small tetrahedral elements. During the Sentaurus Device simulation process, the transport equations and electrical models are solved for each mesh element at each time step.

In the first meshing stage, a coarse mesh is generated for the entire silicon bulk. Silicon in the X-direction of the unit cell (perpendicular the the gridline) is divided into 16 sections, in the Z-direction (parallel to the gridline) 10 sections, and in the Y-direction (depth) 20 sections.

In the second meshing stage, the front surface is refined into three depth regions with successively finer mesh sizes, with mesh elements reducing to $0.1\,\mu$m in depth at the surface. The bottom surface is refined into mesh elements of size corresponding to the doping gradient, using the Sentaurus "MaxTransDiff" mesh refinement method.

In the third meshing stage, the front emitter is divided into ten depth segments, each approximately $0.05\,\mu$m in depth. The region under the front gridline is also given finer definition, down to $4\,\mu$m in width and $0.05\,\mu$m in depth, to model carrier currents around

the gridline edge. Mesh elements under the gridline which are shaded are refined to a similar level. Finally, the LBSF regions are progressively refined in three rings centered around each contact. The finest mesh elements are defined under the contacts, with depths of roughly $0.03\,\mu$m and widths of $5\,\mu$m.

After the mesh element sizes are defined in the structure, Sentaurus Structure Editor calls a Delaunay triangulation algorithm to generate the tetrahedrons which represent the elements. A representative mesh for the **Young3** model contains 720,000 mesh elements.

4.2 Experimental Determination of SRV and Bulk Lifetime

One of the parameters required for device simulation which remains difficult to model is the surface recombination velocity on the interface between dielectric and silicon. In this case, the SRV depends on surface quality, texturing type, dielectric type, surface charge state, injection level, and surface doping density, among other factors [59, 60, 61]. There have been a few recent attempts to parametrize the SRV as a function of surface doping density for a number of different passivation types [62, 59, 63]. Such a parametrization is required for a self-enclosed simulation which can fully optimize solar cell efficiency as a function of implant and anneal parameters. For the current study, however, we attempt instead a simulation model accurate to first-order, and use experimentally determined SRV values for fixed representative conditions.

This study makes use of the quasi-steady-state photoconductance decay (QSSPC) method in order to experimentally measure SRV values for the interface between dielectric and lowly-doped silicon. The QSSPC method has been used for decades in the solar industry to characterize carrier lifetime and junction leakage current [64, 65, 66, 67]. In the absence of doped surfaces, it can also be used to measure SRV. The effective lifetime as measured by this method is influenced by recombination effects from both the bulk and the surfaces:

$$\frac{1}{\tau_{eff}} = \frac{1}{\tau_{bulk}} + \frac{2S}{W}, \tag{4.1}$$

Table 4.1: Oxide-Nitride Stack Passivation Quality, P-Type Substrate

Surface	**Oxide**	τ_{eff} (μs)	S_{max} (cm/s)
Planar	DCE	296 ± 85	33 ± 13
	Dry	108 ± 44	101 ± 61
Tex	DCE	199 ± 23	53 ± 6
	Dry	112 ± 24	96 ± 20

Table 4.2: Oxide-Nitride Stack Passivation Quality, N-Type Substrate

Surface	**Oxide**	τ_{eff} (μs)	S_{max} (cm/s)
Planar	DCE	601 ± 217	19 ± 14
	Dry	386 ± 121	26 ± 13
Tex	DCE	357 ± 66	29 ± 5
	Dry	259 ± 83	44 ± 18

where S is the surface recombination velocity and W the width of the wafer. If a very high lifetime wafer is used, we can assume $\tau_{bulk} \approx \infty$, leaving

$$\frac{1}{\tau_{eff}} \approx \frac{2S}{W}, \tag{4.2}$$

which yields an upper bound for the value of S.

The experiment **S1** was conducted in order to quantify SRV for a variety of different surface passivation types. Parameters varied include P-type vs. N-type wafers, planar vs. textured surfaces, and dry oxygen ambient vs. oxygen with 1,1-dichloroethylene (DCE) ambient. Permutation among these parameters produced eight experimental groups, each of which contained three wafers. Each wafer is measured eight times in different locations on the surface. Due to the small size of each measurement region, we assume each measurement is a statistically independent data point. It should be noted that the same N-type wafers are used in this experiment as those used to fabricate implanted N-type cells.

Figure 4.4 and Figure 4.5 summarize the distribution of data points from these measurements. The white lines represent the median, box boundaries the 25th and 75th percentile, and whiskers the data range. Outliers shown on the plots are excluded from analysis. The average τ_{eff} and S_{max} from the experiment are summarized in Table 4.1 and Table 4.2. We

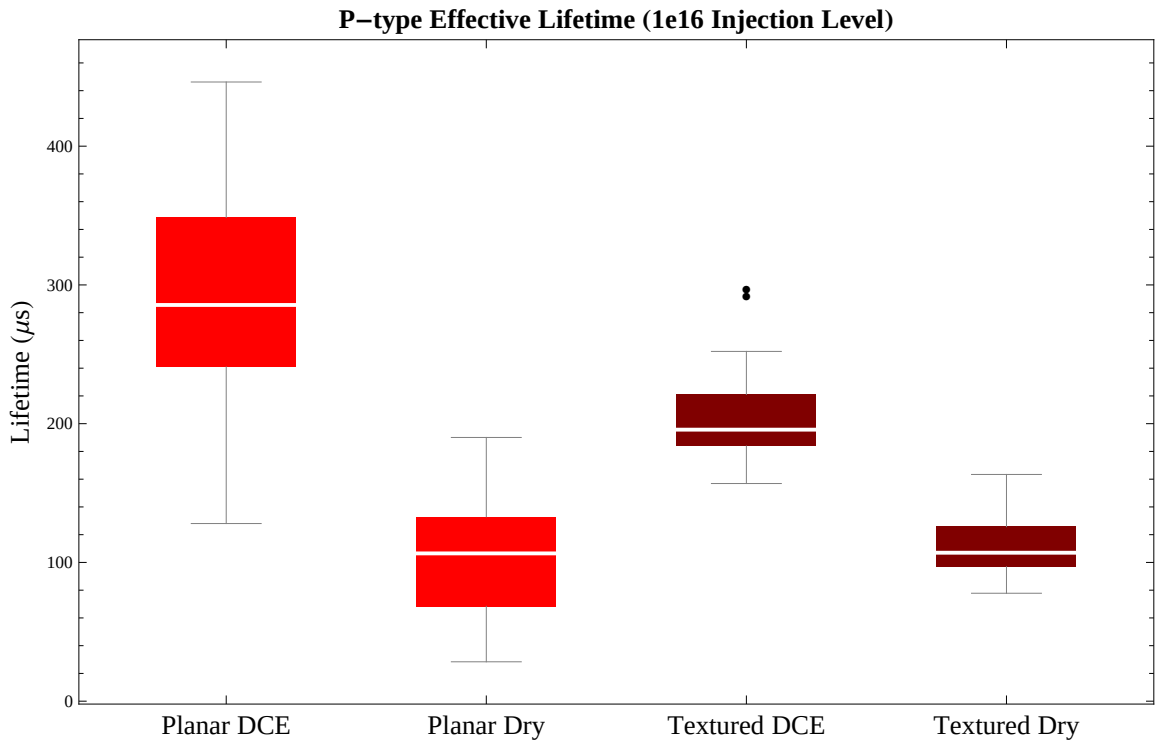

Figure 4.4: τ_{eff} Distribution for Oxide-Nitride Stack Passivation, P-type Substrate

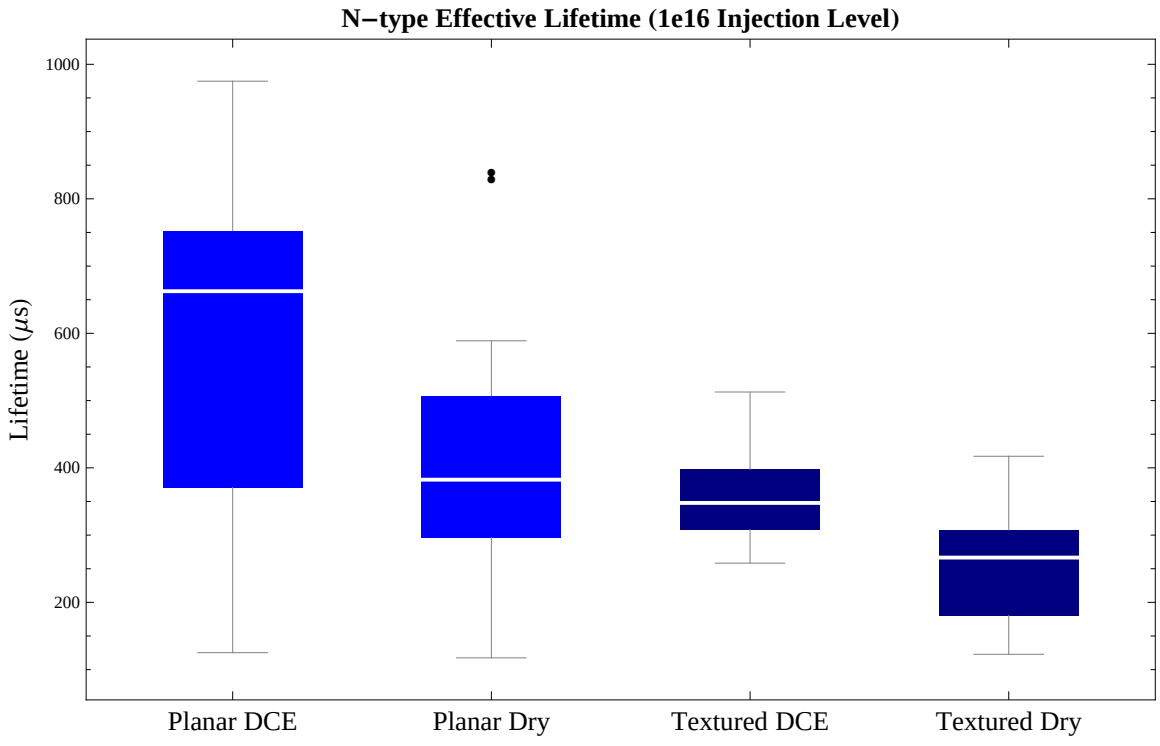

Figure 4.5: τ_{eff} Distribution for Oxide-Nitride Stack Passivation, N-type Substrate

can see from data for the N-type wafers that a DCE oxide-nitride stack on a planarized rear surface should provide a worst-case SRV of 19 cm/s. From these results, and in discussion with other UCEP members, it was reasoned that an actual SRV of 5 cm/s was obtainable with current process techniques [20]. This would correspond roughly to a 200 μm-thick cell with a bulk lifetime of 850 μs and a measured effective lifetime of 600 μs.

In addition to SRV, we can also measure the bulk lifetime of a silicon wafer using the QSSPC method. Instead of assuming a bulk lifetime of infinity, we passivate the surfaces of a silicon wafer with a liquid iodine-methanol solution which effectively reduces surface recombination to zero. The wafer is placed in a clear plastic bag containing the iodine-methanol solution, and the effective lifetime is measured. In this case, $S \approx 0$, leaving

$$\frac{1}{\tau_{eff}} \approx \frac{1}{\tau_{bulk}}. \tag{4.3}$$

Lifetime measurements for baseline N-type solar cells fabricated at the UCEP typically reveal a bulk lifetime of about $\tau_{bulk} = 700\,\mu$s.

Finally, while the QSSPC method is powerful, it still cannot provide an analytical solution for SRV when the surface is doped with a non-analytical doping profile [68]. In the current study, SRV values for the dielectric-emitter and dielectric-BSF interfaces are instead determined indirectly through IQE curve fitting. For this purpose, we use internal quantum efficiency (IQE) data taken from N-type baseline cell **BR69-19**, a representative prototype. The IQE curve is shown in Figure 4.6. The short wavelength response of the cell yields information about the front surface passivation quality, and the long wavelength response indicates bulk carrier lifetime and rear surface passivation quality.

A PC1D model of this cell was developed by the UCEP, and incorporated the bulk lifetime $\tau_{bulk} = 700\,\mu$s as measured. An iterative process was then used to find the combination of FSRV and BSRV values which will recreate the measured IQE curve for the solar cell. It is determined that an FSRV of 3000 cm/s and BSRV of $10000 - 20000$ cm/s produce a good fit to the IQE data. Although the PC1D model is not exact, it is able to give us a reasonably good approximation of the SRV values needed for the Sentaurus device simulation.

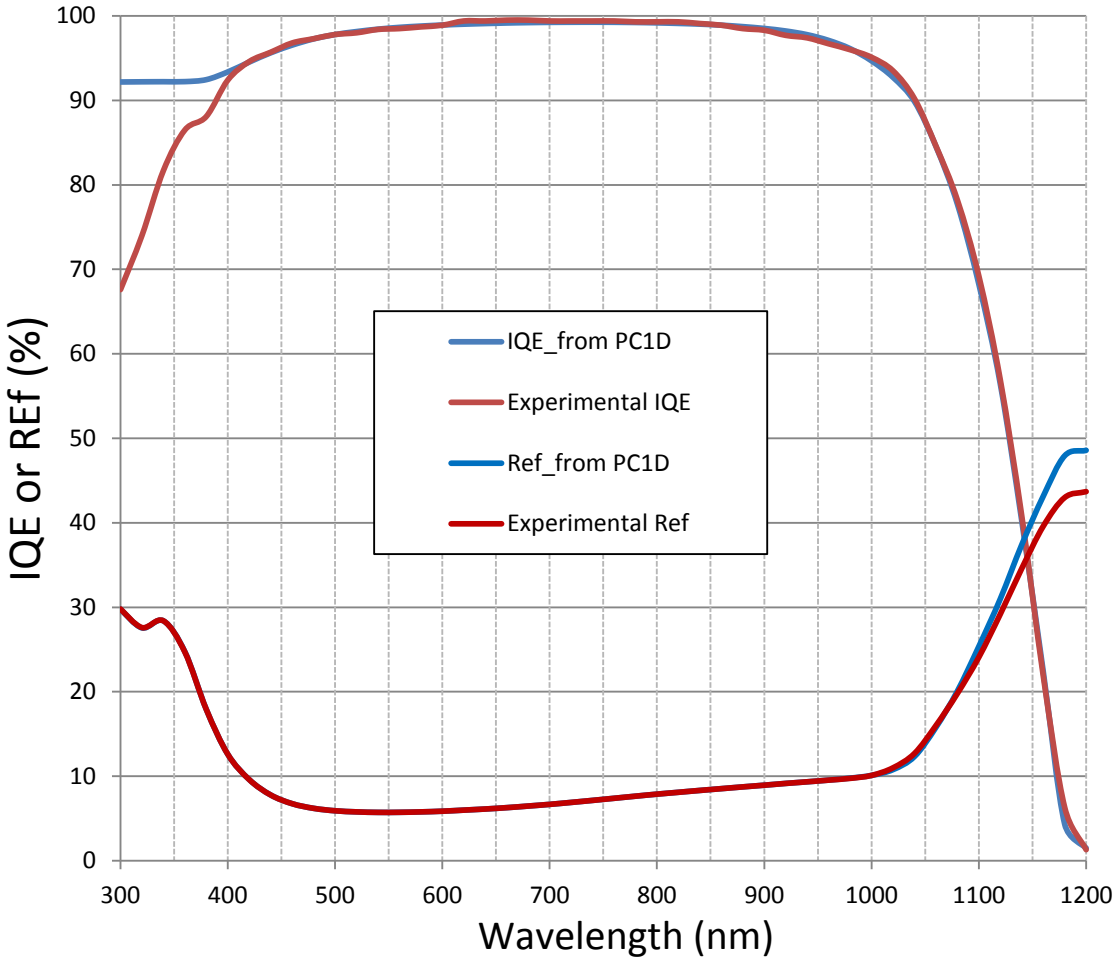

Figure 4.6: IQE Curve from **BR69-19** for SRV Calibration

Table 4.3: Calibration Cell Parameters

	V_{oc} (mV)	J_{sc} ($^{mA}/_{cm^2}$)	**FF**	(%)
69W-85	654	38.8	0.78	19.8
Young2 Simulation	655	38.7	0.78	19.86

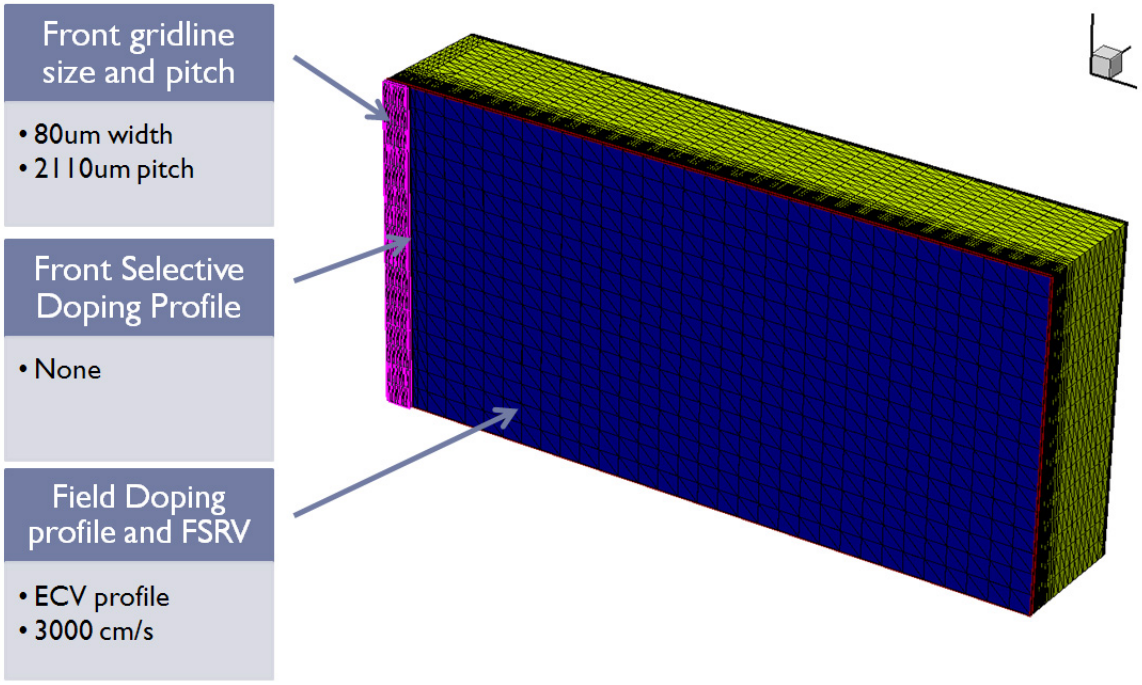

Figure 4.7: Geometry and Set Parameters for Calibration Model **Young2**, Front Side

4.3 Calibration of Remaining Free Parameters

Remaining free parameters in the simulation model include generation profile scaling, R_s, R_{sh}, and the adjustment of BSRV within the range $10000 - 20000\,^{cm}/_{s}$. In order to calibrate these parameters, we fit the simulation to the performance of a baseline N-type implanted solar cell with a full surface BSF. For this study, we use **69W-85** as the prototype cell, operational parameters for which are summarized in Table 4.3. Geometry and set parameters for the simulation model **Young2** are shown in Figure 4.7 and Figure 4.8.

The scaling of the generation profile, as mentioned previously, is a function of front surface reflectance, texturing, and busbar coverage. It affects the J_{sc} value most directly. We find that a generation profile scaling of 0.911 allows for an approximate match to the measured

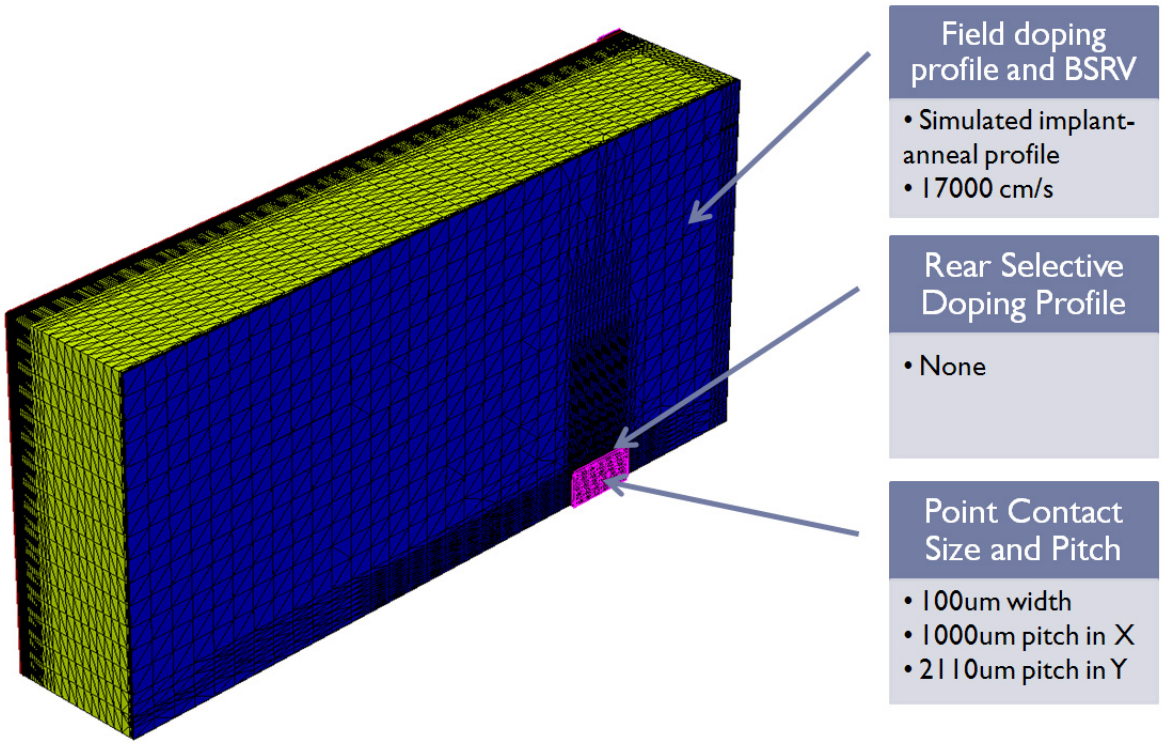

Figure 4.8: Geometry and Set Parameters for Calibration Model **Young2**, Rear Side

cell $J_{sc} = 38.8\,\mathrm{mA/cm^2}$.

R_s and R_{sh} are parameters measured during the IV curve characterization of the solar cell, and directly affect the fill factor of the cell. $R_{sh} = 7433\,\Omega$ is used in the model as measured. The measured series resistance $R_s = 0.67\,\Omega$, however, includes contributions from the busbar, grid, contact, sheet, and substrate resistances. Of these, the device simulation already accounts for the sheet and substrate resistances. In a recent study of implanted N-type cell **69-W-23**, it has been found that the relative contributions of the other sources amounts to about 60-70% of the total series resistance. Thus, we provide $R_s = 0.46\,\Omega$ as input for the simulation. The simulation results in a fill factor of 0.78, which matches that of the measured cell.

The BSRV value is closely tied to the V_{oc} performance of the cell. It was found for the calibration cell that a BSRV of $17000\,\mathrm{cm/s}$ closely matches the measured V_{oc}. A summary of the simulated cell performance for the calibrated model is given in Table 4.3.

It is noted that for the LBSF simulation model **Young3**, we need to adjust series resistance

to $R_s = 0.6\,\Omega$ and generation profile scaling to 0.914 in order for its full BSF results to match the calibration parameters. It is speculated that these small changes arose from changing the rear contact pitch for the full BSF case to $528\,\mu$m, from $1000\,\mu$m in the **Young2** simulation case.

4.4 Establishment of Electrical Boundary Conditions

Electrical boundary conditions are defined at various regions in the structure for LBSF simulation **Young3**. At the interface between the contact and the emitter, and the interfaces between the rear contacts and highly doped LBSF, we set an SRV of $10^5\,\mathrm{cm/s}$, which is unchanged from the **Young2** calibration conditions. The dielectric-emitter interface is given an SRV of $3000\,\mathrm{cm/s}$ as calibrated, and the dielectric-rear field interface an SRV of $5-30\,\mathrm{cm/s}$. For the simulation cases in which a full surface BSF is used, we use an SRV of $17000\,\mathrm{cm/s}$ as calibrated. Finally, there are also boundary conditions for the bulk substrate - the bulk minority carrier lifetime is specified to be $\tau_{bulk} = 700\,\mu$s as measured, and the bulk phosphorus doping $2.38 \times 10^{15}\,\mathrm{cm}^{-3}$, consistent with $2\,\Omega \cdot \mathrm{cm}$ N-type material.

In general, the total front surface recombination velocity (FSRV) which can be experimentally measured is the weighted sum of the separate SRV values:

$$FSRV = \frac{A_{contact}S_{contact} + A_{dielectric}S_{dielectric}}{A_{contact} + A_{dielectric}} \tag{4.4}$$

where $A_{contact}$ and $A_{dielectric}$ denote the areas of the contact-emitter interface and dielectric-emitter interface respectively. The total back surface recombination velocity (BSRV) is calculated in a similar manner.

In this model, it is possible to specify a rear locally doped region which is larger than the contact dot, but there is no easy way to specify a unique SRV between the now exposed LBSF region and the rear dielectric. It is still possible to account indirectly for SRV differences, however. Using the same logic as calculation of FSRV or BSRV, the effective SRV on the

Table 4.4: Summary of Electrical Models Used for Device Simulation

Phenomenon	Model
Free Carrier Statistics	Fermi-Dirac
Intrinsic Carrier Density	$n_i = 9.65 \times 10^9\,\mathrm{cm}^{-3}$[69]
Band Gap Narrowing	Schenck [70]
Free Carrier Mobility	Philips/Klaassen Unified Mobility [71]
Auger Recombination	Dziewior and Schmid [72]
SRH Recombination	Scharfetter [73]

dielectric covered region becomes

$$S_{dielectric,eff} = \frac{A_{field}S_{field} + A_{BSF}S_{BSF}}{A_{field} + A_{BSF}} \tag{4.5}$$

where A_{field} and A_{BSF} denote the areas of the dielectric-field interface and dielectric-BSF interface respectively.

For the purposes of the current study, we limit the simulation to LBSF structures in which the metal contacts are defined to be the same width as the locally doped regions. In order to avoid parasitic shunting around the edges of the rear contacts, the locally diffused regions are extended by $10\,\mu$m in all directions. In a similar fashion, any front surface selective emitter diffusion is also extended away from the gridline by $10\,\mu$m. It was estimated that a $10\,\mu$m margin provides enough room to avoid shunting, while at the same time small enough to avoid inconsistency in SRV between the dielectric-field interface and the dielectric-BSF interface.

4.5 Description of Electrical Models Used

A summary of the electrical models used for device simulation is given in Table 4.4. The choice of these models follows the recommendations of a recent study by Altermatt et al. for solar cell simulation, with the exception of the Scharfetter SRH model, which is the Sentaurus default. The parameters for the models are adjusted according to the Altermatt

study recommendations [36].

4.6 Description of Numerical Solvers Used

Sentaurus Device provides a number of numerical solvers. Among the more popular in literature are Pardiso and ILS. Pardiso is a direct numerical solver for systems of linear equations, which is capable of parallel threading. ILS is an iterative solver for systems of linear equations, which is also capable of parallel threading. ILS utilizes iterative solution and preconditioner methods, and typically solves large problems faster than Pardiso [41]. For example, a solar cell simulation which takes eight hours of CPU time for Pardiso has been seen to take only 1 hour on ILS. For problems which are sensitive to perturbations, however, ILS may not be capable of converging to a solution. This results in a solver crash. Early runs for the **Young2** model compare the results of using Pardiso versus using ILS for the solar cell device simulation. No appreciable difference in cell behavior is seen - both simulations result in $V_{oc} = 655\,\mathrm{mV}$, $J_{sc} = 38.7\,\mathrm{mA/cm^2}$, $FF = 0.78$, and $\eta = 19.86\%$. **Young3** makes use of the ILS solver running in multi-threaded mode.

There are a few different stages which occur during the solving process for the simulation developed in this work. The first stage calculates the behavior of the solar cell's equilibrium point under zero bias. In effect, this identifies the J_{sc} of the cell. During the next stage, the simulator ramps the applied bias upward while solving for the quasistationary equilibrium solution at each step. This stage proceeds in steps of less than 200 mV until the bias reaches 400 mV. The third stage is another quasistationary ramp with a smaller step size, which allows the simulation to accurately capture the maximum power point of the solar cell. This stage proceeds in steps of less than 20 mV until the net current flow reverses direction and the cell reaches V_{oc} condition. In effect, the Sentaurus Device simulation traces the IV curve for the solar cell model.

4.7 LBSF Simulation Results and Discussion

Characterization of the performance of LBSF solar cells using this model looked at two main parameters: LBSF dot size and dot pitch. These geometry factors cannot be adequately simulated in a 1D software such as PC1D. Simulations were also conducted to examine the dependence of efficiency on BSRV and wafer resistivity. Summarized below are the results of the simulation, and discussion of trends observed.

4.7.1 LBSF Performance as a Function of Dot Pitch and BSRV

The first two simulation series in the **Young3** model measured cell efficiency, V_{oc}, and FF as a function of dot pitch and BSRV. The results are summarized in Figure 4.9 and Figure 4.10. In the plots, the black lines represent a full-BSF cell of otherwise equivalent parameters (a baseline cell with dot pitch of 528 μm). It is apparent that reduced BSRV in all cases results in increased LBSF cell efficiency, however, the LBSF design does not always provide cell efficiencies higher than that of the baseline.

A look at the V_{oc} and FF trends reveals the reason. While the LBSF provides higher V_{oc} in all cases due to the quality of rear surface passivation, this gain is offset by a loss in FF due to the increased sheet resistance to carriers moving along the cell's rear surface. An optimized balance between the two effects is reached at approximately 450 μm dot pitch. The results also suggest that it might be possible to increase the cell efficiency by introducing a light field doping in the rear surface. If the recombination increase is slight, V_{oc} may be preserved while at the same time improving the FF.

4.7.2 LBSF Performance as a Function of Dot Size and Rear Surface Coverage

It is useful to also parametrize the LBSF geometry in terms of rear surface coverage, which is commonly seen in literature. We conduct simulations to examine the dependence of

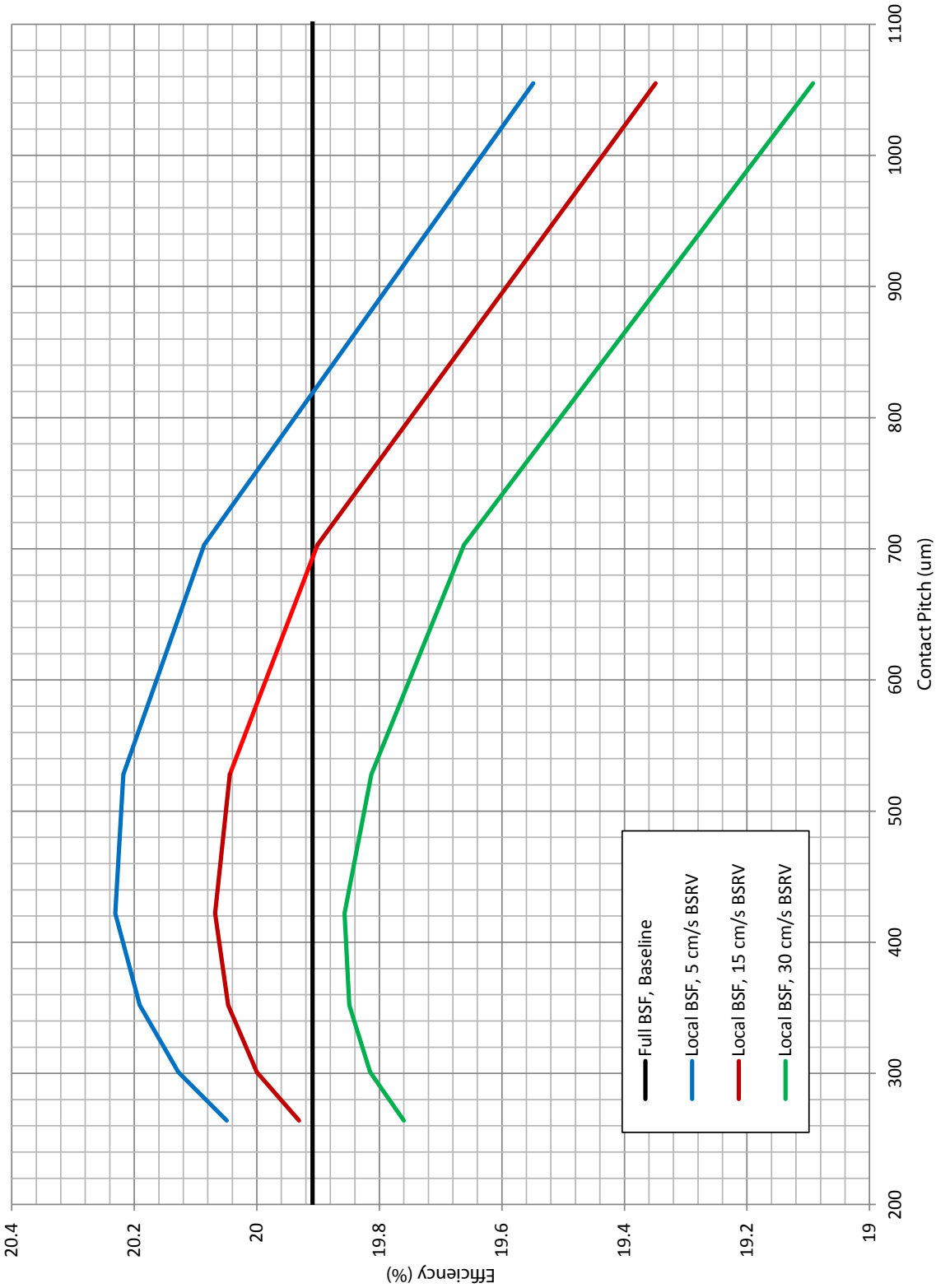

Figure 4.9: Solar Cell Efficiency as a Function of Dot Pitch and BSRV (**Young3**)

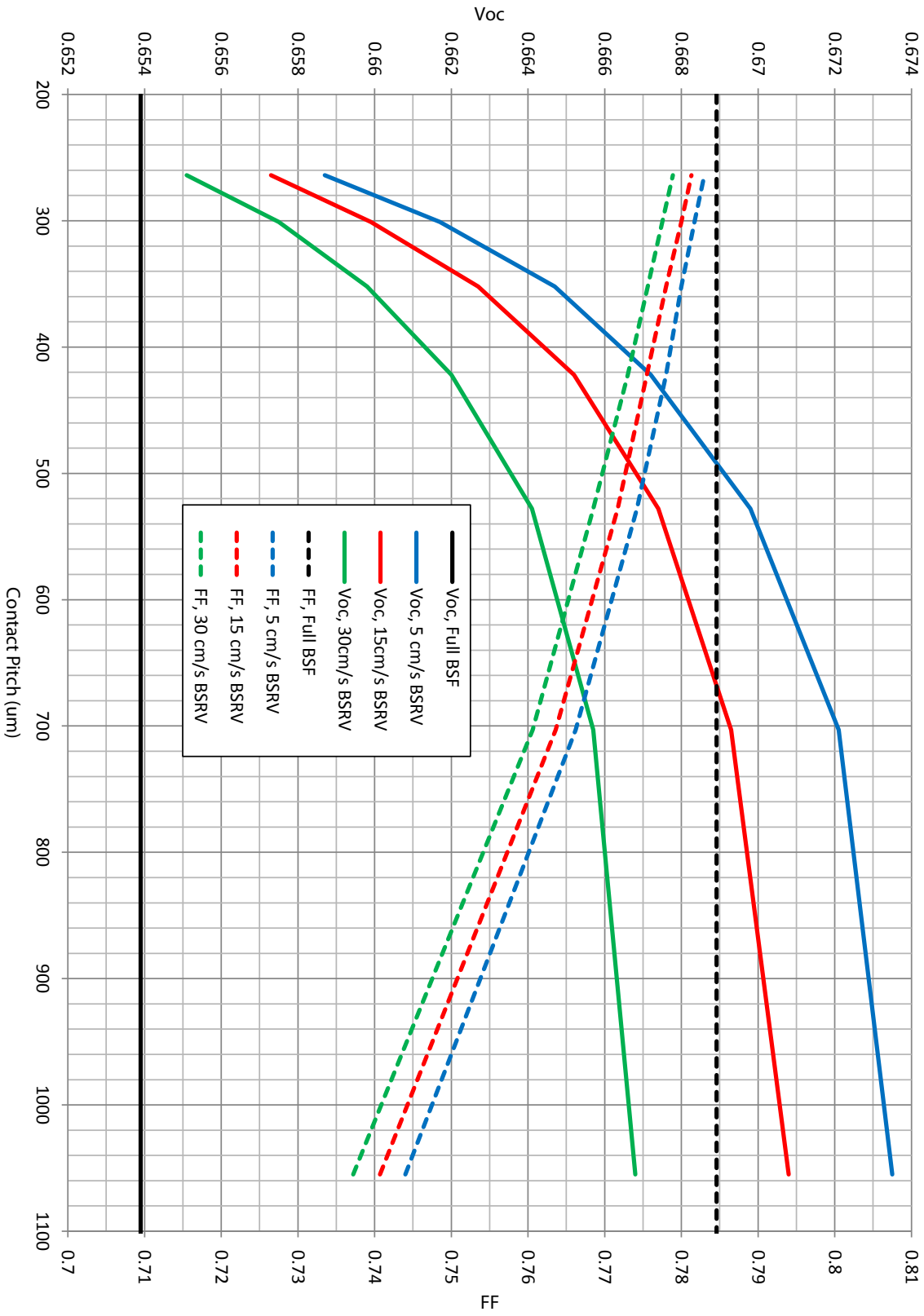

Figure 4.10: V_{oc} and FF as a Function of Dot Pitch and BSRV (**Young3**)

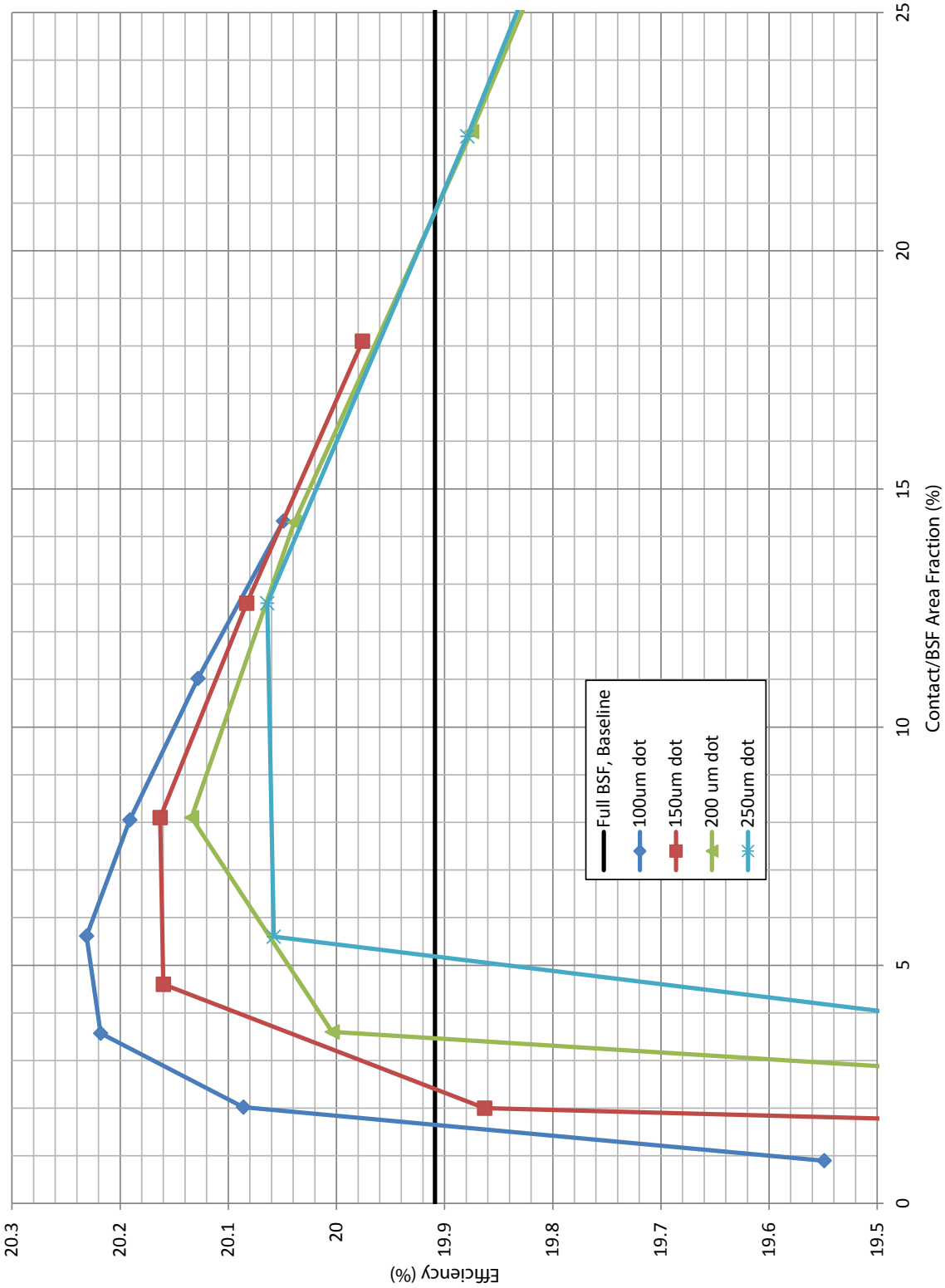

Figure 4.11: Solar Cell Efficiency a Function of Dot Size and Area Coverage (**Young3**)

efficiency on dot size and effective rear surface coverage. The results are summarized in Figure 4.11. It can be seen that the dot size influences not only the maximum efficiency of the cell but also the area coverage fraction at which that maximum efficiency occurs. Process limitations involving the implantation mask will place restrictions on the size of dots which can accurately be implanted. It is useful to know, however, that the smaller these dots become, the higher the potential efficiency gain.

4.7.3 LBSF Performance as a Function of Wafer Resistivity and Lifetime

Finally we examine the dependence of cell efficiency on the substrate material. Material lifetime considerations often limit the choice of wafer resistivity for the fabrication of solar cells. The trends identified by the simulation in Figure 4.12, however, show that if it is possible to obtain $1\,\Omega \cdot \mathrm{cm}$ N-type wafers with a lifetime of 1 ms, it is possible to increase the cell efficiency to 20.7%. If CZ grown wafers of that resistivity cannot reach such lifetimes, however, it may be necessary to use float-zone grown material instead.

4.8 Areas for Simulation Model Improvement

We have developed and calibrated for this study a 3D model of an N-type implanted solar cell with LBSF rear structure. The model is accurate to first order and capable of reproducing the behavior of a full BSF N-type implanted cell. There are a number of improvements, however, which can to make this model more accurate. The first of these would be implementation of BSRV and contact resistance models to calculate these values as a function of surface doping concentration. The solar cell model currently has fixed parameters for BSRV and R_s, and thus it is not yet possible to optimize the doping profiles to produce even higher solar cell efficiencies.

The second improvement involves more closely examining the finite-element mesh refinement in the 3D model. In a study by Altermatt et al., recommendations were put forth concerning the distribution of mesh element sizes for various parts of the solar cell [36]. The current

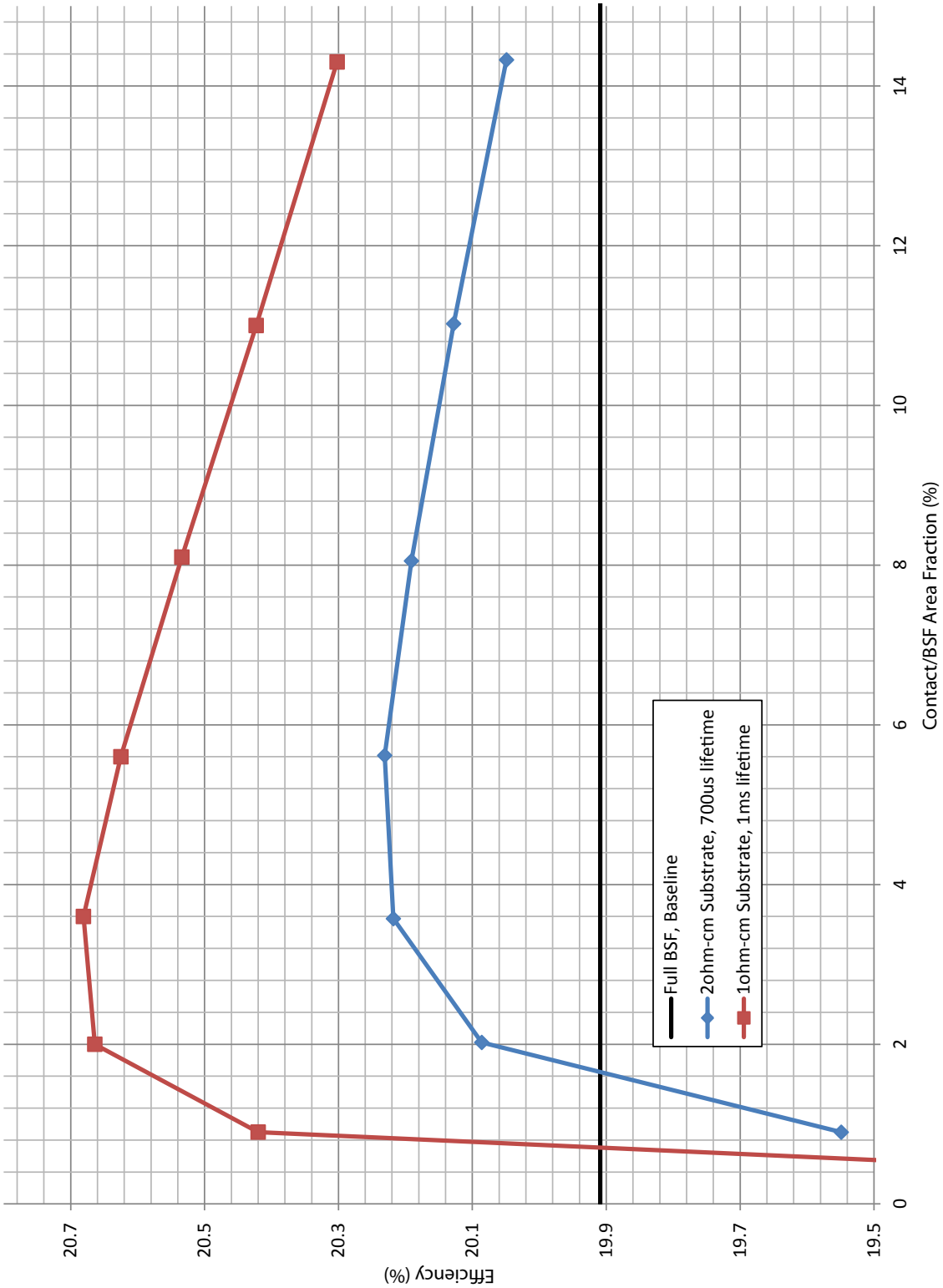

Figure 4.12: Solar Cell Efficiency a Function of Substrate Resistivity and Area Coverage (**Young3**)

study does not make use of those recommendations, and it would be elucidating to perform a comparative study of the Altermatt mesh refinement method versus the current mesh refinement method.

In addition, a study of overall mesh optimization could be conducted. For finite element analysis in general, a mesh is considered to have enough elements to accurately represent the physical behavior if increasing the number of mesh elements does not change the results of the simulation. On the other hand, using too many mesh elements unnecessarily slows down the model simulation. A very limited amount of mesh optimization has been conducted for the current study, and it would be helpful to perform a more complete characterization.

Additional areas of improvement include expanding the LBSF geometry capabilities of the model. It is easier from a process perspective to create round contacts for an LBSF, whether using photolithography or hard implant masking. The current simulation model, however, only supports square doping regions and contacts. Sentaurus Structure Editor code may be written in order to implement circular doping regions and cylindrical contacts. In addition, LBSF overhang is difficult to implement in this model due to the BSRV inconsistencies mentioned previously. For this purpose, Sentaurus Structure Editor code may also be written to define unique interface areas where the BSF contacts the dielectric, in order to allow for the proper SRV to be defined in those regions.

Chapter 5

Task III - Development of a Procedure for Ion Implanted N-type LBSF Cell Fabrication

Near the end of this study, an opportunity arose for performing masked ion implantation of phosphorus at Rochester Institute of Technology to fabricate LBSF structures. A procedure has been developed in this study to make proof-of-concept implanted LBSF solar cells utilizing photolithographically defined nitride for ion implant masking. The current work reports on the beginning stages of development for this procedure, and progress is still ongoing at the time of this writing.

Shown in Figure 5.1 is an outline of the proof-of-concept procedure. The boron implantation tool at Suniva, Inc. used by the UCEP can only accommodate 6" pseudosquare wafers, and the LBSF phosphorus implant tool at RIT only 4" round wafers. The procedure, then, involves forming the boron emitter on a 6" wafer, laser cutting the wafer to a 4" round, and completing the process on a 4" wafer. Since a hard mask is not currently available for performing the patterned LBSF implant, we make use of photolithographically defined openings in 150 nm-thick PECVD nitride in order to accomplish local implantation. The

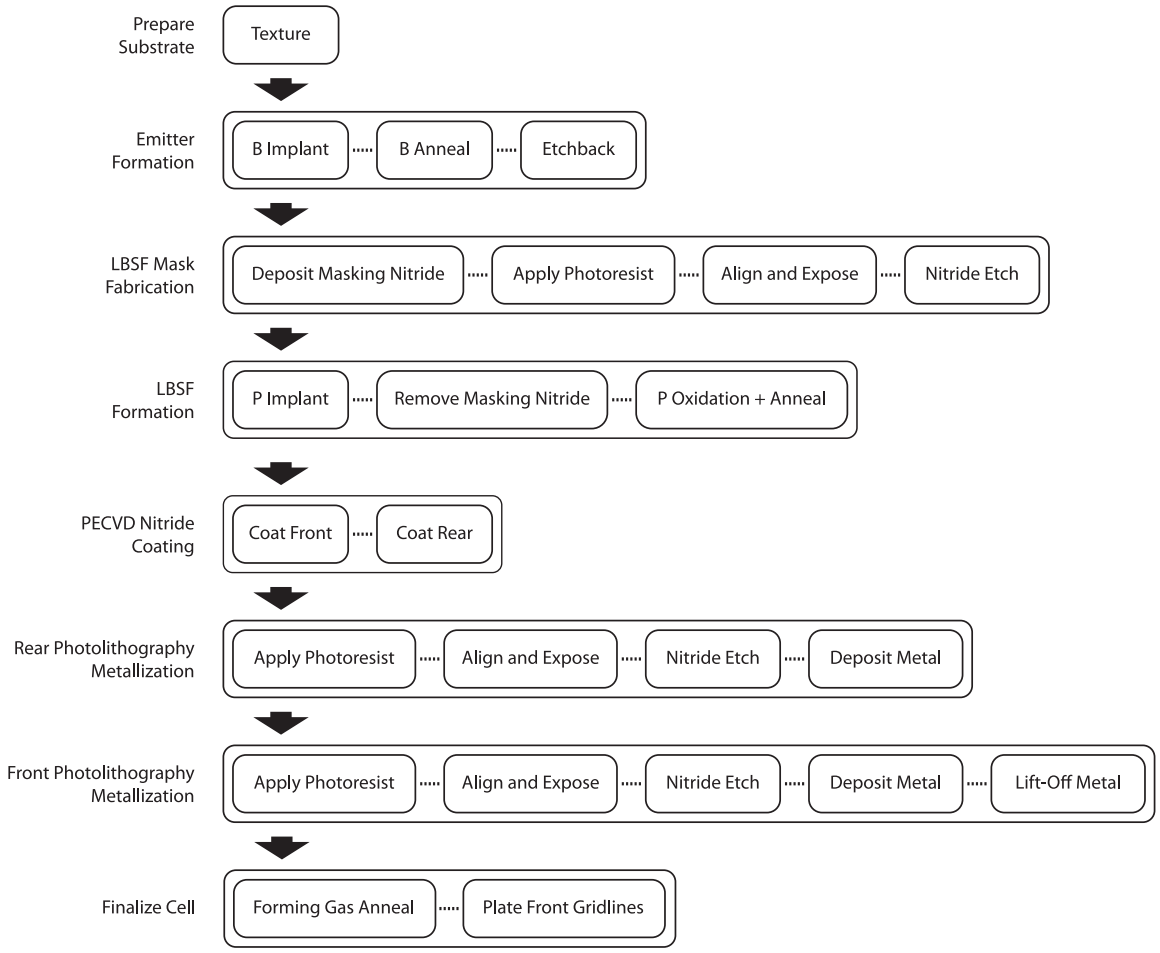

Figure 5.1: Procedure for Proof-of-Concept Implanted LBSF Cell Fabrication Utilizing Photolithography

photomask used for LBSF patterning in this study includes 75 μm diameter round openings with 500 μm pitch. It is estimated that a hard mask of the type used in the Dube et al. study would perform just as well in formation of LBSF regions with this feature size [35].

The full series of process steps is discussed in detail in the sections below.

5.1 Preparation of Substrate

1. Start with 6" pseudosquare 2ohm-cm CZ wafer
2. Saw damage etch
3. Texture random pyramids

Fabrication of the candidate LBSF cell begins in the same manner as the baseline implanted N-type solar cells developed at UCEP. On the bare wafer, a saw damage etch is performed to remove surface damage and residual contaminant caused by the wafer cutting process. An alkaline solution is then used to create random pyramidal texturing on the cell surface. After texturing, the wafers have an approximate thickness of 180 μm.

5.2 Implantation of Emitter

1. Boron implant front
2. Clean
3. Perform boron anneal
4. Planarize rear
   (a) Deposit etch blocking nitride on front
   (b) Etch rear
   (c) Remove etch blocking nitride

5. Emitter etchback/shaving
   (a) Remove oxide
   (b) Etch front emitter
   (c) Remove oxide

Implantation of the boron emitter also follows the same procedure as developed for the baseline cell. The ion implanter at Suniva, Inc. is used to perform boron implantation at a dose of $3 \times 10^{15}\,\mathrm{cm}^{-2}$ and an energy of 10 keV. This is followed by an RCA or equivalent clean. The wafer is then annealed in a contaminant-free tube furnace at 1000 °C for one hour in a nitrogen ambient.

Rear planarization is performed to increase the rear dielectric passivation quality. First, an etch-blocking nitride of 80 nm is grown via PECVD on the front surface of the wafer. Planarization is then achieved by immersing the wafers in dilute KOH solution for 12 min at a temperature of 75 °C. The etch-blocking nitride is then removed by immersing the wafers in 5% HF solution for 40 minutes.

Next, the BRL on the emitter surface post boron anneal is removed via direct etchback, instead of thermal oxide followed by oxide removal. It has been shown in preliminary studies at the UCEP that the etchback provides for a higher cell efficiency relative to the BRL oxide removal. The native oxide on the wafer surface is first removed by a 5 minute dip in 5% HF solution. The etchback is then performed in an acetic-nitric-HF (100:100:1) solution for 80 seconds. A follow-up 5% HF dip is performed for 5 minutes to remove any remaining oxide. At this stage, the wafers have an average thickness of 160 μm.

5.3 Creation of Rear Implant Mask

1. Deposit implant masking nitride on rear surface

2. Deposit protective nitride on front surface
3. Cut to 4" round
4. Apply rear photoresist for patterning
   (a) Spin photoresist on rear
   (b) Soft bake
5. Photolithography align and expose rear holes
   (a) Rough alignment to wafer round
   (b) Expose hole pattern and fiducials
6. Protect front surface
   (a) Spin photoresist on front
   (b) Soft bake
7. Open rear holes
   (a) Develop resist
   (b) Hard bake
   (c) Etch hole pattern in implant masking nitride
   (d) Strip resist

A rear implant mask procedure was developed for this study which utilizes a photolithography defined nitride mask to achieve patterned LBSF implant. PECVD nitride of 150 nm thickness is first grown on both front and rear surfaces. The wafer is then cut by UV laser to a 4" round form in order to be compatible with the phosphorus implant tool. It is noted that the flat on the 4" round shape should be oriented perpendicular to the remaining saw damage pattern. The gridlines are photolithographically defined perpendicular to the flat as well, and it was found that electroplating of the gridlines parallel to the damage lines results in more consistent gridline width.

Two coats of Microposit SC-1827 positive photoresist are then deposited on the rear surface of the wafer, followed by a spin each time at 3000rpm for 30 seconds. A soft bake is then performed at 90 °C for 20 minutes. Next, the wafer is aligned roughly (in absence of fiducials) to the LBSF photomask , and exposed at 405 nm to a dose of 460 $^{mJ}/_{cm^2}$. The front side

is then protected with two coats of Microposit SC-1827, followed by a spin each time at 3000rpm for 30 seconds. A soft bake is again performed at 90 °C for 20 minutes.

The wafers are developed for 50 seconds in Microposit 351 diluted to 25% concentration, with periodic slight agitation to the solution. This is followed by a hard bake at 120 °C for 30 minutes. The nitride etch is then performed for 50 minutes in BOE 6:1 solution. The photoresist is removed in an acetone soak, followed by a methanol and isopropanol rinse. It is found that slight surface contaminants introduced during the texturing process (fingerprints and smears) were carried through the planarization process, and resulted in damage to the LBSF features during nitride etch. The smeared regions over-etched and removed the LBSF pattern in those regions.

5.4 Implantation of LBSF

1. Phosphorus implant rear
2. Etch implant masking nitride away
3. Clean wafer
4. Perform phosphorus anneal and oxidation

Phosphorus implantation of the rear surface is performed at a dose of $3 \times 10^{15}\,\mathrm{cm}^{-2}$ and energy of 25 keV. At the time of this writing, this implant has just been completed. Characterization of the sheet resistance of nitride-masked versus unmasked regions is forthcoming. It is anticipated that the nitride will be removed with a 50 minute dip in BOE 6:1, and the wafers cleaned in an RCA equivalent process before phosphorus annealing. The anneal will consist of oxidation at 840 °C for 30 minutes in oxygen ambient, followed by anneal at 840 °C for 25 minutes in nitrogen ambient.

5.5 Creation of Dielectric Passivation Layer

1. Deposit PECVD nitride on front
2. Deposit PECVD nitride on rear

Creation of the dielectric layer will consist of PECVD nitride deposition on both front and rear surfaces in the same recipes used for baseline ion-implanted N-type cells. The front will receive an approximately 65 μm nitride, and the rear a 25 μm nitride.

5.6 Rear Surface Metallization

1. Apply rear photoresist for patterning
   (a) Spin photoresist on rear
   (b) Soft bake
2. Photolithography align and expose rear holes
   (a) Align to fiducials
   (b) Expose hole pattern
3. Protect front surface nitride
   (a) Spin photoresist on front
   (b) Soft bake
4. Open rear holes
   (a) Develop resist
   (b) Hard bake
   (c) Etch hole pattern in nitride
   (d) Strip resist
5. Evaporate metal on rear surface
6. Protect rear surface metallization

(a) Spin photoresist

(b) Soft bake

After creation of the dielectric stack, the front and rear side metallization processes will follow the same procedure used by the UCEP for fabricating small area cells. Although not yet performed for the LBSF cell described in this study, the author has performed and verified this metallization process on small area implanted N-type baseline cells.

On the rear, two coats of Microposit SC-1827 are first deposited, followed by a spin each time at 3000 rpm for 30 seconds. A soft bake is then performed at 90 °C for 20 minutes. The photomask in the LBSF case will be aligned to the fiducials on the rear surface of the LBSF cell, visible as contrast in the nitride color. As before, the photoresist will be exposed at 405 nm to a dose of 460 $^{mJ}/_{cm^2}$.

The front surface is protected using two coats of Microposit SC-1827, followed by a spin each time at 3000 rpm for 30 seconds. This is followed by a soft bake at 90 °C for 20 minutes. As before, windows in the photoresist are developed using Microposit 351 solution, followed by the same hard bake.

Windows in the nitride are etched using BOE 6:1 solution, and the resist is stripped in the same acetone-methanol-isopropanol rinse. The rear is then subject to a full surface metal evaporation of 60 nm Ti, 40 nm Pd, and 40 nm Ag. SPR220-7 photoresist is spun onto the rear surface at 3000 rpm for 30 seconds to protect the metallization. This is followed by a soft bake at 90 °C for 20 minutes. It is noted that a thicker 2000 nm Ag layer may be used next time to improve back surface reflectivity.

5.7 Front Grid Metallization

1. Apply front photoresist for patterning
   (a) Spin photoresist
   (b) Soft bake
2. Photolithography align and expose front grid
   (a) Rough alignment to wafer round
   (b) Expose grid pattern
3. Open lines
   (a) Develop resist
   (b) Hard bake
   (c) Etch grid pattern into nitride
4. Evaporate metal on front surface
5. Strip resist while lifting off metal from front

On the front, photolithographically defined openings in the photoresist and nitride stack serve as a deposition template for the front grid during the metal evaporation process. Microposit SC-1827 photoresist is spun and soft baked as before. The grid photomask is then aligned to the wafer round, and the wafer is exposed at 405nm to a dose of $460\,^{\mathrm{mJ}}/_{\mathrm{cm}^2}$. This grid pattern is opened in the nitride following the same procedure as before. The front is then subject to a full surface metal evaporation of 60 nm Al, 40 nm Ti, 40 nm Pd, and 40 nm Ag.

After evaporation, excess metal in the front field is removed when the photoresist is dissolved in a lift-off process. This also dissolves the protective photoresist on the rear surface.

5.8 Cell Finalization

1. Forming gas anneal

2. Plate front contacts
3. Isolate cells

A forming gas anneal (FGA) at 400 °C is performed to improve the front grid contact quality. The grid lines are subsequently plated with silver to improve their cross sectional area. Cell isolation may be accomplished with a photolithographically defined mesa etch, or alternatively with a wafer dicing saw.

The author has worked in collaboration with the UCEP to apply the above discussed front and rear metallization process to 4" baseline implanted N-type solar cells. It is shown that fill factors of 80%, series resistance values of 0.4 Ω, and short circuit current densities of 38.8 $^{mA}/_{cm^2}$ can be obtained with this process. Although the V_{oc} values were lower than baseline due to lack of process optimization, the maximum cell efficiencies for these 4" cells were around 20.0% [74]. As compared to the 6" baseline process to which the simulation model was calibrated, this 4" process provides noticeable improvement of contact quality. It is expected that the LBSF solar cells fabricated using the 4" process will see corresponding boosts to efficiency.

Chapter 6

Concluding Remarks

Development of an industrially feasible implanted N-type LBSF solar cell promises to be a major step forward in the quest toward more cost effective high efficiency silicon solar cells. Each concept explored in this study - namely N-type substrates, ion implantation, and LBSF structures - offers substantial benefits over current technologies if manufacturing challenges can be resolved. In addressing these challenges, the current study has proposed the use of advanced simulation to narrow the scope of process parameters which need to be explored during the development process. Toward this end, the study has accomplished three tasks which have been set out:

Task I - Implant and Anneal Model Development and Validation

We have developed a boron implant and anneal model and successfully validated it to theory and experiment. We have also developed phosphorus implant and anneal models which appear to fit experimental results. Although there remain uncertainties in the experimental data used to validate the phosphorus simulation, the simulated doping profiles were nonetheless successfully used to model solar cell performance.

Task II - Device Simulation Development and Calibration

We have extended the capabilities of an existing 3D Sentaurus model to allow for simulation of ion-implanted LBSF solar cells. We calibrated this model to experimentally measured cell performance parameters and surface recombination velocity values. The resulting model is capable of reproducing the behavior of a baseline implanted N-type full BSF solar cell, with all parameters falling into the theoretically expected ranges.

Next, we use the model to explore geometric parameters of an LBSF solar cell which optimize its performance. The model shows that 20.7% efficiency is achievable using an LBSF structure on a cell similar to baseline cells fabricated at the UCEP. The model also reveals trends in V_{oc} and FF which agree with theoretical predictions. It is additionally established that there are advantages to developing processes for smaller LBSF dot size, and to using lower resistivity wafers.

Task III - Development of a Procedure for Ion Implanted N-type LBSF Cell Fabrication

Taking advantage of a new opportunity for performing local implants, we developed a procedure which utilizes the prior experience of the UCEP, and includes new process steps to accomplish local implantation through the use of a patterned nitride mask. Although fabrication of these LBSF cells is still ongoing at the time of writing, we demonstrate that the process sequence is capable of producing 20.0% efficient full BSF solar cells.

Appendix A

Source Code

Included in this appendix is a copy of the primary command files written in this study to conduct implant/anneal simulations and 3D device simulations used in this study. Full copies of all Sentaurus project files may be found on the UCEP server, at the time of writing, in Z:\Steven Ning\Data\. Due to the size of these packages, it is not possible to include all files in the thesis.

A.1 process.cmd

This file serves as the input for Sentaurus Process in conducting implant and anneal simulations. The file is taken from model **Young5**.

```
1  # vim: set filetype=tcl :
2
3  #if "@tool_label@" == "Emitter"
4      if {@enableEmitter@ == 0} {
5          return
6      }
7      set implantSpecies "@emitterImplantSpecies@"
8      set implantEnergy @emitterImplantEnergy@
9      set implantDose @emitterImplantDose@
10     set implantTilt @emitterImplantTilt@
11     set annealTime1 @emitterAnnealTime1@
12     set annealTemp1 @emitterAnnealTemp1@
13     set annealGas1 "@emitterAnnealGas1@"
14     set annealTime2 @emitterAnnealTime2@
15     set annealTemp2 @emitterAnnealTemp2@
16     set annealGas2 "@emitterAnnealGas2@"
17     set annealTime3 @emitterAnnealTime3@
18     set annealTemp3 @emitterAnnealTemp3@
19     set annealGas3 "@emitterAnnealGas3@"
20 #elif "@tool_label@" == "FrontField"
21     if {@enableFrontField@ == 0} {
22         return
23     }
24     set implantSpecies "@frontImplantSpecies@"
25     set implantEnergy @frontImplantEnergy@
26     set implantDose @frontImplantDose@
27     set implantTilt @frontImplantTilt@
28     set annealTime1 @frontAnnealTime1@
29     set annealTemp1 @frontAnnealTemp1@
30     set annealGas1 "@frontAnnealGas1@"
31     set annealTime2 @frontAnnealTime2@
32     set annealTemp2 @frontAnnealTemp2@
33     set annealGas2 "@frontAnnealGas2@"
34     set annealTime3 @frontAnnealTime3@
35     set annealTemp3 @frontAnnealTemp3@
36     set annealGas3 "@frontAnnealGas3@"
37 #elif "@tool_label@" == "BSF"
38     if {@enableBSF@ == 0} {
39         return
40     }
41     set implantSpecies "@bsfImplantSpecies@"
42     set implantEnergy @bsfImplantEnergy@
43     set implantDose @bsfImplantDose@
44     set implantTilt @bsfImplantTilt@
45     set annealTime1 @bsfAnnealTime1@
46     set annealTemp1 @bsfAnnealTemp1@
47     set annealGas1 "@bsfAnnealGas1@"
48     set annealTime2 @bsfAnnealTime2@
49     set annealTemp2 @bsfAnnealTemp2@
50     set annealGas2 "@bsfAnnealGas2@"
51     set annealTime3 @bsfAnnealTime3@
52     set annealTemp3 @bsfAnnealTemp3@
53     set annealGas3 "@bsfAnnealGas3@"
54 #elif "@tool_label@" == "RearField"
55     if {@enableRearField@ == 0} {
56         return
57     }
```

```
58      set implantSpecies "@rearImplantSpecies@"
59      set implantEnergy @rearImplantEnergy@
60      set implantDose @rearImplantDose@
61      set implantTilt @rearImplantTilt@
62      set annealTime1 @rearAnnealTime1@
63      set annealTemp1 @rearAnnealTemp1@
64      set annealGas1 "@rearAnnealGas1@"
65      set annealTime2 @rearAnnealTime2@
66      set annealTemp2 @rearAnnealTemp2@
67      set annealGas2 "@rearAnnealGas2@"
68      set annealTime3 @rearAnnealTime3@
69      set annealTemp3 @rearAnnealTemp3@
70      set annealGas3 "@rearAnnealGas3@"
71  #else
72      return
73  #endif
74
75  # Adaptive remeshing options
76  pdbSet Grid Adaptive 1
77  pdbSet Diffuse Growth.Regrid.Steps 10
78
79  # Diffusion models
80  AdvancedCalibration 2012.06
81  AdvancedModels
82  pdbSet Silicon Boron Interstitial ClusterSizes {{1 0} {1 1} {1 2} {2 1} {3 1} {3 2}}
83  term name=PhosphorusDiffFactor add Silicon eqn = "@phosDiffFactor@"
84  term name=BoronDiffFactor add Silicon eqn = "@boronDiffFactor@"
85  pdbSet Ox_Si B CMax {[Arr @boronCmax@  1.0]}
86  #pdbSet Oxide_Silicon Phosphorus BoundaryCondition HomNeumann
87
88  # Specify MC implant model
89  pdbSet ImplantData MonteCarlo 1
90  pdbSet MCImplant model sentaurus.mc
91  pdbSet MCImplant cascades 1
92  pdbSet Silicon LatticeType Zincblende
93  pdbSet MCImplant Particles 1000
94
95  # Init mesh
96  line x location=0 spacing=.1<nm> tag=SiTop
97  line x location=10<nm> spacing=.2<nm>
98  line x location=50<nm> spacing=.5<nm>
99  line x location=300<nm> spacing=1<nm>
100 line x location=1<um> spacing=2<nm>
101 line x location=2<um> spacing=5<nm> tag=SiBottom
102
103 # Init substrate material and doping
104 region Silicon xlo=SiTop xhi=SiBottom
105 init field=@baseSpecies@ concentration=@baseDoping@ wafer.orient = {1 1 1}
106
107 # Perform Implant
108 implant $implantSpecies dose=$implantDose beam.dose energy=$implantEnergy tilt=
        $implantTilt
109
110 # Perform anneal
111 if {$annealTime1 > 0} {
112     diffuse time=$annealTime1<min> temperature=$annealTemp1<C> $annealGas1
113 }
114
115 if {$annealTime2 > 0} {
116     diffuse time=$annealTime2<min> temperature=$annealTemp2<C> $annealGas2
117 }
118
119 if {$annealTime3 > 0} {
120     diffuse time=$annealTime3<min> temperature=$annealTemp3<C> $annealGas3
121 }
122
123 strip oxide
124
```

```
125 # Make measurements
126 SheetResistance
127 if {$implantSpecies == "phosphorus"} {
128     puts "Integrate total phosphorus..."
129     select silicon z=PTotal
130     integrate
131     puts "Integrate active phosphorus..."
132     select silicon z=PActive
133     integrate
134 } elseif {$implantSpecies == "boron"} {
135     puts "Integrate total boron     ..."
136     select silicon z=BTotal
137     integrate
138     puts "Integrate active boron     ..."
139     select silicon z=BActive
140     integrate
141 }
142
143 # Export result
144 struct tdr=profiletdr_n@node@ !gas !interfaces
145 SetPlxList {PActive BActive}
146 WritePlx  profile-n@node@.plx
```

A.2 sde_dvs.cmd

This file is the input for Sentaurus Structure Editor. It generates the 3D solar cell structure and mesh. The file is based on a Sentaurus 3D simulation example [58]. The file is taken from model **Young5**.

```
#setdep @previous@
# vim: set filetype=scheme :
;-----------------------------------------------------------
;        3D Solar Cell structure with rear contacts;
;-----------------------------------------------------------
(sde:clear)

;;-------------------------------------------------------------------------------------------

;;STEP 1: define global parameters for structure set-up
;; STEP 1.1 (User-defined parameters)
(display "Begin variable definition...\n")
;;; define contact material
(define RearCntMaterial "Silver")
(define FrontCntMaterial "Aluminum")

;;; define geometry parameters
(define SubstrateThickness @cell_thickness@ ) ; um; suggested range: 100~200
(define FrontArcThickness 0.075 ) ; um
(define RearRcThickness 0.075 ) ; um

;;; front contacts
(define FrontCntThickness 6 ) ; um
(define FrontCntWidth @frontContactWidth@ ) ; um
(define FrontCntPitch @frontContactPitch@ ) ; um

;; Rear contacts
(define RearCntThickness 6 ) ; um
(define RearCntWidth @rearContactWidth@ ) ; um
(define RearCntPitch @rearContactPitch@ ) ; um
(define ShiftX @rearOffset@ ) ; um

;;; doping
(define SubstrateDop @baseDoping@ ) ; cm^-3; Uniform doping in substrate

(define EmitterJunc 0.65) ; junction depth for mesh refinement use
(define EmitterRange 1) ; how deep the profile definition goes
(define EmitterProfile "profile-n@node|Emitter@.plx")
(define EmitterWidth @emitterWidth@)

(define BSFJunc 0.8 ) ; junction depth for mesh refinement use
(define BSFRange 1) ; how deep the profile definition goes
(define BSFProfile "profile-n@node|BSF@.plx") ;"profile-ecvphos.plx");
(define BSFWidth @bsfWidth@)

(define FrontFieldJunc 0.65) ; junction depth for mesh refinement use
(define FrontFieldRange 1) ; how deep the profile definition goes
(define FrontFieldProfile "profile-n@node|FrontField@.plx")

(define RearFieldJunc 0.8 ) ; junction depth for mesh refinement use
(define RearFieldRange 1) ; how deep the profile definition goes
(define RearFieldProfile "profile-n@node|RearField@.plx")

;; Optical generation
(define CntFile "./contact_optical_@cell_thickness@.plx")
```

```
(define noCntFile "./no_contact_optical_@cell_thickness@.plx")

; Apply full rear contact if rearPointPitch == 0 or rearPointWidth == 0
(if (or (= RearCntPitch 0) (= RearCntWidth 0))
    (define FlagAllCnt 1)
    (define FlagAllCnt 0)
)

; Apply full rear BSF if bsfWidth == 0 or using full rear contact
(if (or (= @bsfWidth@ 0) (= FlagAllCnt 1))
    (begin
        (define FlagFullBSF 1)
        (set! RearFieldJunc BSFJunc)
    )
    (define FlagFullBSF 0)
)

; Do not apply rear field if enableRearField == 0 or have full BSF
(if (or (= @enableRearField@ 0) (= FlagFullBSF 1))
    (define FlagRearField 0)
    (define FlagRearField 1)
)

; Do not apply BSF if enableBSF == 0
(if (= @enableBSF@ 0)
    (define FlagBSF 0)
    (define FlagBSF 1)
)

; Apply full front emitter doping if emitterWidth == 0
(if (= @emitterWidth@ 0)
    (begin
        (define FlagFullEmitter 1)
        (set! FrontFieldJunc EmitterJunc)
    )
    (define FlagFullEmitter 0)
)

; Do not apply front field if enableFrontField == 0 or have full emitter
(if (or (= @enableFrontField@ 0) (= FlagFullEmitter 1))
    (begin
        (define FlagFrontField 0)
        (set! FrontFieldJunc EmitterJunc)
    )
    (define FlagFrontField 1)
)

; Do not apply emitter if enableEmitter == 0
(if (= @enableEmitter@ 0)
    (define FlagEmitter 0)
    (define FlagEmitter 1)
)

; Automatic computation
(define HalfFrontCntWidth (/ FrontCntWidth 2))
(define HalfRearCntWidth (/ RearCntWidth 2))
(define RearCntSpacing (- RearCntPitch RearCntWidth))

(if (= FlagEmitter 1)
    (begin
        (define HalfEmitterWidth (/ EmitterWidth 2))
        (define EmitterMargin (/ (- EmitterWidth FrontCntWidth) 2))
    )
    (begin
        (define EmitterMargin 0)
    )
)

```

```
123 (if (= FlagBSF 1)
124     (begin
125         (define HalfBSFWidth (/ BSFWidth 2))
126         (define BSFMargin (/ (- BSFWidth RearCntWidth) 2))
127     )
128     (begin
129         (define BSFMargin 0)
130     )
131 )
132
133 (display "End variable definition.\n")
134
135 ;; Error checking
136 (if
137     (>= FrontCntPitch RearCntPitch)
138     (begin
139         (define CellW (/ FrontCntPitch 2))
140         (if (= RearCntPitch 0)
141         (begin (define CellL CellW) )
142         (begin (define CellL (/ RearCntPitch 2)) )
143         )
144     )
145     (begin ; when FrontCntPitch < RearCntPitch
146         (display "Error --> frontCntPitch < rearCntPitch! User input violates the
                module's assumption.\n")
147         (stop)
148     )
149 )
150
151 (if
152     (and
153         (>= RearCntWidth RearCntPitch)
154         (not (= RearCntPitch 0))
155     )
156     (begin
157         (display "Error --> rearCntSize >= rearCntPitch! Cannot correctly place rear
                contacts. \n")
158         (stop)
159     )
160 )
161
162 ;;;; calculate how many rear contacts can be placed along X direction
163 ;;;; because the length of the simulation domain is half rear contact pitch, only a
    half-contact
164 ;;;; will be placed along Z direction.
165
166 (define RearCntArea 0)
167
168 (if (= FlagAllCnt 1)
169     (begin
170         (set! RearCntArea (* CellW CellL))
171     )
172     (begin
173         (if (> ShiftX 0)
174             (begin ; starting with a complete contact, whose 1st edge placed at x=
                    ShiftX
175                 (define numCnt_x (truncate (/ (- CellW ShiftX) RearCntPitch)))
176                 (set! RearCntArea (* numCnt_x (* RearCntWidth HalfRearCntWidth))) ;
                        only 0.5 contact size along Z
177                 (define endSpaceX (- (- CellW (* RearCntPitch numCnt_x)) ShiftX))
178             )
179             (begin ; else: starting with a half contact, whose center placed at x=0
180                 (define numCnt_x (+ 1 (truncate (/ (- CellW HalfRearCntWidth)
                        RearCntPitch))))
181                 (set! RearCntArea (* (- numCnt_x 1) (* HalfRearCntWidth RearCntWidth)
                        ))
182                 (set! RearCntArea (+ RearCntArea (* HalfRearCntWidth HalfRearCntWidth
                        )))
```

```
183                 (define endSpaceX (- (- (- CellW (* RearCntPitch (- numCnt_x 1)))
                        HalfRearCntWidth) RearCntSpacing))
184             )
185         )
186         (if
187             (and ; enough room to place 0.5 contact at end (+/-1um)
188                 (<= endSpaceX (+ HalfRearCntWidth 1))
189                 (>= endSpaceX (- HalfRearCntWidth 1))
190             )
191             (begin
192                 (set! numCnt_x (+ numCnt_x 1))
193                 (set! RearCntArea (+ RearCntArea (* HalfRearCntWidth endSpaceX)))
194             )
195         )
196         (if (> endSpaceX RearCntWidth) ; enough room to place a whole contact with
                some space left in X direction
197             (begin
198                 (set! numCnt_x (+ numCnt_x 1))
199                 (set! RearCntArea (+ RearCntArea (* RearCntWidth HalfRearCntWidth)))
200             )
201         )
202         (if (<= numCnt_x 0)
203             (begin
204                 (display "Error: 0 contacts along X direction! Please adjust input
                        structure info and continue.\n")
205                 (stop)
206             )
207         )
208     )
209 )
210
211 (display (string-append (string-append "\nnumCnt_x: " (number->string numCnt_x)) "\n
        "))
212 (display (string-append (string-append "\nendSpace_x: " (number->string endSpaceX))
        "\n"))
213 (display (string-append (string-append "\nDOE: Cell_W " (number->string CellW)) "\n")
        )
214 (display (string-append (string-append "\nDOE: Cell_L " (number->string CellL)) "\n")
        )
215 (display (string-append (string-append "\nDOE: rearCntArea " (number->string
        RearCntArea)) "\n"))
216 (define ac
217     (/
218         (round
219             (*
220                 1000
221                 (/ RearCntArea (* CellW CellL))
222             )
223         )
224         10
225     )
226 )
227 (display (string-append (string-append "\nDOE: AreaCoverage " (number->string ac)) "\
        n"))
228
229
230 ;;-----------------------------------------------------------------------------------

231 ;; STEP 2 (Create basic structure)
232
233 ;;; substrate
234 (sdegeo:create-cuboid
235     (position 0 0 0)
236     (position CellW SubstrateThickness CellL)
237     "Silicon"
238     "substrate"
239 )
240
```

```
241 ;;; front ARC
242 (sdegeo:create-cuboid
243     (position HalfFrontCntWidth 0 0)
244     (position CellW (- FrontArcThickness) CellL)
245     "FrontDielectric"
246     "frontArc"
247 )
248
249 ;;; front contact metal
250 (sdegeo:create-cuboid
251     (position 0 (- FrontCntThickness) 0)
252     (position HalfFrontCntWidth 0 CellL)
253     FrontCntMaterial
254     "frontContact"
255 )
256
257 ;;; rear ARC
258 (sdegeo:create-cuboid
259     (position 0 SubstrateThickness 0)
260     (position CellW (+ SubstrateThickness RearRcThickness) CellL)
261     "RearDielectric"
262     "rearRc"
263 )
264
265 ;;; rear contact metal
266 (sdegeo:set-default-boolean "ABiA")
267
268 ;;;; define a procedure to create one rear contact, which can be used repeatedly
269 (define CreateRearCnt
270     (lambda (Xll Zll Xur Zur) ; Xll/Zll (lower-left), Xur/Zur (upper-right)
271         (begin
272             (sdegeo:create-cuboid
273                 (position Xll SubstrateThickness Zll)
274                 (position Xur (+ SubstrateThickness RearCntThickness) Zur)
275                 RearCntMaterial
276                 "rearContact"
277             )
278         )
279     )
280 )
281
282 ;;;; Starting from the lower-left corner of simulation domain, to place the 1st rear
    contact
283 ;;;; --> 1st rear contact: starting from x=ShiftX Z=0 to place the edges of the 1st
    rear contact
284 ;;;; --> Place more rear contacts along X direction at the same Z location
285 ;;;; --> Move to the next Z location, and place another row of rear contacts along X
    direction
286
287 (define currentLocZ 0)
288 (define currentLocX ShiftX)
289 (define restSpaceX 0)
290
291 (if (= FlagAllCnt 0)
292     (begin
293         (set! restSpaceX (- CellW ShiftX))
294         (set! currentLocX ShiftX)
295         (do
296             ((x 0 (+ x 1)))  ; do-loop for X direction
297             ((= x numCnt_x))
298             (begin
299                 (display "restSpaceX:  ") (display restSpaceX) (newline)
300                 (cond
301                     (; place half of first contact in X direction
302                         (and (= x 0) (= ShiftX 0))
303                         (begin
304                             (display "Placing half first contact")(newline)
305                             (CreateRearCnt
```

```
306                                 currentLocX
307                                 currentLocZ
308                                 (+ currentLocX HalfRearCntWidth)
309                                 (+ currentLocZ HalfRearCntWidth)
310                             )
311                             (set! currentLocX (+ currentLocX (- RearCntPitch
                                    HalfRearCntWidth)))
312                             (set! restSpaceX (- restSpaceX (- RearCntPitch
                                    HalfRearCntWidth)))
313                         )
314                     )
315                     (; enough room to place 0.5 contact at the end (+/-1um)
316                         (and
317                             (<= restSpaceX (+ HalfRearCntWidth 1))
318                             (>= restSpaceX (- HalfRearCntWidth 1))
319                         )
320                         (begin
321                             (display "Placing half last contact")(newline)
322                             (CreateRearCnt
323                                 currentLocX
324                                 currentLocZ
325                                 (+ currentLocX restSpaceX)
326                                 (+ currentLocZ HalfRearCntWidth)
327                             )
328                         )
329                     )
330                     (; else enough room to place whole contact in X direction
331                         else
332                         (begin
333                             (display "Placing full contact")(newline)
334                             (CreateRearCnt
335                                 currentLocX
336                                 currentLocZ
337                                 (+ currentLocX RearCntWidth)
338                                 (+ currentLocZ HalfRearCntWidth)
339                             )
340                             (set! currentLocX (+ currentLocX RearCntPitch))
341                             (set! restSpaceX (- restSpaceX RearCntPitch))
342                         )
343                     )
344                 )
345             )
346         ) ; end of do-loop for X direction contact placement
347     )
348     (begin ; else apply whole back contact
349         (CreateRearCnt 0 0 CellW CellL)
350     )
351 )
352
353 ;;-----------------------------------------------------------------------------------

354 ;; STEP 3 (Create generation profiles)
355 ;; import external optical generation, which has been calculated separately
        beforehand
356 (display "Placing optical generation...")
357
358 (define PlaceOpt
359     (lambda (win_name place_name Xll Zll Xur Zur)
360         (begin
361             (sdedr:define-refinement-window
362                 win_name
363                 "Rectangle"
364                 (position Xll 0 Zll)
365                 (position Xur 0 Zur)
366             )
367             (sdedr:define-1d-external-profile
368                 "1d_opt_def2"
369                 CntFile
```

```
370                 "Scale" 1.0
371                 "Range" 0 1000
372                 "Erf"
373                 "Factor" 0
374             )
375             (sdedr:define-analytical-profile-placement
376                 place_name
377                 "1d_opt_def2"
378                 win_name
379                 "Positive"
380                 "Replace"
381                 "Eval"
382             )
383         )
384     )
385 )
386
387 (sdedr:define-refinement-window "globalopt_window" "Rectangle" (position
        HalfFrontCntWidth 0 0)
388 (position CellW 0 CellL))
389 (sdedr:define-1d-external-profile "1d_opt_def" noCntFile "Scale" 1.0 "Range" 0 1000 "
        Erf" "Factor" 0)
390 (sdedr:define-analytical-profile-placement "1d_opt_place" "1d_opt_def" "
        globalopt_window" "Positive" "NoReplace" "Eval")
391
392 (if (= FlagAllCnt 1)
393     (begin
394         (PlaceOpt "opt_win" "opt_place" HalfFrontCntWidth 0 CellW CellL)
395     )
396     (begin
397         (define optWinName "opt_win_")
398         (define optPlaceName "opt_place_")
399         (define optWinPrefix "opt_win_")
400         (define optPlacePrefix "opt_place_")
401         (define totalCnt 0)
402         (set! restSpaceX (- CellW ShiftX))
403         (set! currentLocX ShiftX)
404         (define Xstart currentLocX)
405
406         (do ((x 0 (+ x 1))) ((= x numCnt_x))
407             (begin
408                 (set! optWinName (string-append optWinPrefix (number->string totalCnt
                        )))
409                 (set! optPlaceName (string-append optPlacePrefix (number->string
                        totalCnt)))
410
411                 (cond
412                     ((and (= x 0) (= ShiftX 0)) ;; first condition: if it's the first
                            half-contact
413                         (begin ; only room to place half contact in X direction
414                             (if (< HalfFrontCntWidth (+ currentLocX HalfRearCntWidth)
                                    )
415                                 (begin
416                                     (set! Xstart (max currentLocX HalfFrontCntWidth))
417                                     (PlaceOpt
418                                         optWinName
419                                         optPlaceName
420                                         Xstart
421                                         currentLocZ
422                                         (+ currentLocX HalfRearCntWidth)
423                                         (+ currentLocZ HalfRearCntWidth)
424                                     )
425                                 )
426                             )
427
428                             (set! totalCnt (+ totalCnt 1))
429                             (set! currentLocX (+ currentLocX (- RearCntPitch
                                    HalfRearCntWidth)))
```

```
430                             (set! restSpaceX (- restSpaceX (- RearCntPitch
                                    HalfRearCntWidth)))
431                         )
432                     )
433                     ((= restSpaceX HalfRearCntWidth) ;; second condition: if it's the
                         last half-contact
434                         (begin ; only room to place half contact in X direction
435                             (PlaceOpt
436                                 optWinName
437                                 optPlaceName
438                                 currentLocX
439                                 currentLocZ
440                                 (set! totalCnt (+ totalCnt 1))
441                                 (+ currentLocX HalfRearCntWidth)
442                                 (+ currentLocZ HalfRearCntWidth)
443                             )
444                         )
445                     )
446                     (else ;; place whole contact
447                         (begin
448                             (if (< HalfFrontCntWidth (+ currentLocX RearCntWidth))
449                                 (begin
450                                     (set! Xstart (max currentLocX HalfFrontCntWidth))
451                                     (PlaceOpt
452                                         optWinName
453                                         optPlaceName
454                                         Xstart
455                                         currentLocZ
456                                         (+ currentLocX RearCntWidth)
457                                         (+ currentLocZ HalfRearCntWidth)
458                                     )
459                                 )
460                             )
461
462                             (set! totalCnt (+ totalCnt 1))
463                             (set! currentLocX (+ currentLocX RearCntPitch))
464                             (set! restSpaceX (- restSpaceX RearCntPitch))
465                         )
466                     )
467                 )
468             )
469         )
470     )
471 )
472
473 (display "Finished optical generation.")(newline)
474
475 ;;-----------------------------------------------------------------------------------

476 ;; STEP 5 (Substrate doping)
477 (display "Placing substrate doping: ")
478 (display SubstrateDop)(display " @baseSpecies@...")
479 (sdedr:define-refinement-window
480     "substrateWindow"
481     "Cuboid"
482     (position 0 0 0)
483     (position CellW SubstrateThickness CellL)
484 )
485 (if (equal? "@baseSpecies@" "phosphorus")
486     (sdedr:define-constant-profile
487         "subDop_def"
488         "PhosphorusActiveConcentration"
489         SubstrateDop
490     )
491 )
492 (if (equal? "@baseSpecies@" "boron")
493     (sdedr:define-constant-profile
494         "subDop_def"
```

```
495         "BoronActiveConcentration"
496         SubstrateDop
497     )
498 )
499 (sdedr:define-constant-profile-placement
500     "subDop_place"
501     "subDop_def"
502     "substrateWindow"
503 )
504
505 (display "Finished substrate doping.")(newline)
506
507 ;;-----------------------------------------------------------------------------

508 ;; Define a procedure to place doping profiles
509
510 (define PlaceDopingProfile
511     (lambda (name profile X Y Z dX dY dZ) ; profile definition starts at Y and
        extends dY
512         (begin
513             (define refinementname (string-append name "_refinement"))
514             (define placementname (string-append name "_place"))
515             (define refevalname (string-append name "_refeval"))
516             (define profilename (string-append name "_profile"))
517             (define pos1 (position X Y Z))
518             (define pos2 (position (+ X dX) (+ Y dY) (+ Z dZ)))
519             (define direction "Positive")
520             (if (= (/ dY (abs dY)) -1)
521                 (begin
522                     (set! pos1 (position X (+ Y dY) Z))
523                     (set! pos2 (position (+ X dX) Y (+ Z dZ)))
524                     (set! direction "Negative")
525                 )
526             )
527             (sdedr:define-refinement-window ; define the plane which the doping
                    profile starts from
528                 refinementname
529                 "Rectangle"
530                 (position X Y Z)
531                 (position (+ X dX) Y (+ Z dZ))
532             )
533             (sdedr:define-refeval-window ; define the 3D region the doping applies to
534                 refevalname
535                 "Cuboid"
536                 pos1
537                 pos2
538             )
539             (sdedr:define-1d-external-profile
540                 profilename
541                 profile
542                 "Scale" 1
543                 "Range" 0 (abs dY)
544                 "Erf"
545                 "Factor" 0
546             )
547
548             (sdedr:define-analytical-profile-placement
549                 placementname
550                 profilename
551                 refinementname
552                 direction
553                 "Replace"
554                 "Eval"
555                 refevalname
556                 0
557                 "evalwin"
558             )
559         )
```

```
560      )
561  )
562
563  ;;-----------------------------------------------------------------------------------------

564  ;; STEP 4 (Place front doping)
565  (display "Placing front doping: ")
566
567  (if (= FlagFrontField 1)
568      (begin ; Place front field
569          (display "Front field doping...")
570          (PlaceDopingProfile
571              "FrontField"
572              FrontFieldProfile
573              0 0 0
574              CellW FrontFieldRange CellL
575          )
576      )
577  )
578
579  (if (= FlagFullEmitter 1)
580      (begin ; Place full emitter
581          (display "Full emitter doping...")
582          (PlaceDopingProfile
583              "FullEmitter"
584              EmitterProfile
585              0 0 0
586              CellW EmitterRange CellL
587          )
588      )
589      (begin ; Place local emitter
590          (display "Local emitter doping...")
591          (PlaceDopingProfile
592              "LocalEmitter"
593              EmitterProfile
594              0 0 0
595              HalfEmitterWidth EmitterRange CellL
596          )
597      )
598  )
599
600  (display "Finished front doping.")(newline)
601
602  ;-----------------------------------------------------------------------------------------

603  ;; STEP 7 (Rear selective doping)
604  (display "Placing rear doping: ")
605
606  (if (= FlagRearField 1)
607      (begin ; Place rear field doping
608          (display "Rear field doping...")
609          (PlaceDopingProfile
610              "RearField"
611              RearFieldProfile
612              0 SubstrateThickness 0
613              CellW (* -1 RearFieldRange) CellL
614          )
615      )
616  )
617
618  (if (= FlagBSF)
619      (if (= FlagFullBSF 1)
620          (begin ; place full rear BSF
621              (display "Rear full BSF doping...")
622              (PlaceDopingProfile
623                  "FullBSF"
624                  BSFProfile
625                  0 SubstrateThickness 0
```

```
626                 CellW (* -1 BSFRange) CellL
627             )
628         )
629         (begin ; place local rear BSFs
630             (set! restSpaceX (- CellW ShiftX))
631             (set! currentLocX (- ShiftX HalfRearCntWidth))
632 
633             (do ((x 0 (+ x 1))) ((= x numCnt_x))
634                 (begin
635                     (display "Local BSF ")(display (+ x 1))(display "...")
636                     (PlaceDopingProfile
637                         (string-append "LocalBSF_" (number->string (+ x 1)))
638                         BSFProfile
639                         (- currentLocX BSFMargin) SubstrateThickness currentLocZ
640                         BSFWidth (* -1 BSFRange) HalfBSFWidth
641                     )
642                     (set! currentLocX (+ currentLocX RearCntPitch))
643                     (set! restSpaceX (- restSpaceX RearCntPitch))
644                 )
645             )
646         )
647     )
648 )
649 
650 (display "Finished rear doping.")(newline)
651 
652 ;;-----------------------------------------------------------------------------------------

653 ;; STEP 8: define the contacts
654 (display "Placing contacts...")
655 (sdegeo:define-contact-set "nContact" 4  (color:rgb 1 0 0 ) "##" )
656 (sdegeo:define-contact-set "pContact" 4  (color:rgb 0 0 1 ) "##" )
657 
658 (define pCntFace ; Define front electrical contact
659     (sdegeo:imprint-rectangular-wire
660         (position 0 (- FrontCntThickness) 0)
661         (position HalfFrontCntWidth (- FrontCntThickness) CellL)
662     )
663 )
664 (sdegeo:define-3d-contact
665     pCntFace
666     "pContact"
667 )
668 
669 (define DefineRearCnt ; Function to define rear electrical contacts, used later on
670     (lambda (cntFace_name Xll Zll Xur Zur) ; Xll/Zll (lower-left), Xur/Zur (upper-
        right)
671         (begin
672             (define cntFace_name
673                 (sdegeo:imprint-rectangular-wire
674                     (position Xll (+ SubstrateThickness RearCntThickness) Zll)
675                     (position Xur (+ SubstrateThickness RearCntThickness) Zur)
676                 )
677             )
678             (sdegeo:define-3d-contact
679                 cntFace_name
680                 "nContact"
681             )
682         )
683     )
684 )
685 
686 (display "Finished contacts.")(newline)
687 
688 ;;-----------------------------------------------------------------------------------------

689 ;; STEP 9: Add mesh refinements
690 (display "Adding mesh refinements...")
```

```
;; start from global mesh refinement with coarse mesh
(define gMeshX 100)
(define gMeshY 20)
(define gMeshZ 100)

(define FrontCntExt_X (max 10 (+ EmitterMargin 10))); um
(define FrontCntExt_Y EmitterJunc); um

(define RearCntExt_XZ (max 10 (+ BSFMargin 10))) ; um
(define RearCntExt_Y BSFJunc) ; um

;; --> bulk of the substrate which are not shaded
(sdedr:define-refinement-window
    "bulk_win1"
    "Cuboid"
    (position (+ HalfFrontCntWidth FrontCntExt_X) (* FrontCntExt_Y 10) 0)
    (position CellW SubstrateThickness CellL)
)
(sdedr:define-multibox-size
    "bulk_refsize1"
    gMeshX gMeshY gMeshZ
    gMeshX gMeshY gMeshZ
    1 1 1
)
(sdedr:define-multibox-placement
    "bulk_refplace1"
    "bulk_refsize1"
    "bulk_win1"
)

;; --> bulk of the substrate which are shaded
(sdedr:define-refinement-window
    "bulk_win"
    "Cuboid"
    (position 0 (* FrontCntExt_Y 10) 0)
    (position (+ HalfFrontCntWidth FrontCntExt_X) SubstrateThickness CellL)
)
(define tempX (/ (+ HalfFrontCntWidth FrontCntExt_X) 4))
(sdedr:define-multibox-size
    "bulk_refsize"
    tempX gMeshY gMeshZ
    tempX gMeshY gMeshZ
    1 1 1
)
(sdedr:define-multibox-placement
    "bulk_refplace"
    "bulk_refsize"
    "bulk_win"
)

(display "Bulk done, ")

;; --> top surface close to the p-n junction and ARC
(sdedr:define-refinement-window
    "global_topwin1"
    "Cuboid"
    (position 0 (- FrontArcThickness) 0)
    (position CellW (+ EmitterJunc FrontCntExt_Y) CellL)
)
(sdedr:define-refinement-size
    "global_topsize1"
    (/ gMeshX 2) (/ gMeshY 20) (/ gMeshZ 2)
    (/ gMeshX 5) (/ gMeshY 100) (/ gMeshZ 5)
)
(sdedr:define-refinement-function
    "global_topsize1"
    "DopingConcentration"
    "MaxTransDiff" 1.0
```

```
759 )
760 (sdedr:define-refinement-placement
761     "global_topplace1"
762     "global_topsize1"
763     "global_topwin1"
764 )
765
766 (display "Top done, ")
767
768 ;; --> second layer (coarser mesh) of refinement in between junction and bulk region
769 (sdedr:define-refinement-window
770     "global_topwin2"
771     "Cuboid"
772     (position 0 (+ EmitterJunc FrontCntExt_Y) 0)
773     (position CellW (* FrontCntExt_Y 10) CellL)
774 )
775 (sdedr:define-multibox-size
776     "global_topsize2"
777     gMeshX (/ gMeshY 5) gMeshZ
778     gMeshX (/ gMeshY 20) gMeshZ
779     1 1.2 1
780 )
781 (sdedr:define-multibox-placement
782     "global_topplace2"
783     "global_topsize2"
784     "global_topwin2"
785 )
786
787 (sdedr:define-refinement-window
788     "global_topwin3"
789     "Cuboid"
790     (position 0 (* FrontCntExt_Y 10) 0)
791     (position CellW (* FrontCntExt_Y 30) CellL)
792 )
793 (sdedr:define-multibox-size
794     "global_topsize3"
795     gMeshX gMeshY gMeshZ
796     gMeshX (/ gMeshY 5) gMeshZ
797     1 1.2 1
798 )
799 (sdedr:define-multibox-placement
800     "global_topplace3"
801     "global_topsize3"
802     "global_topwin3"
803 )
804
805 (display "Region near top done, ")
806
807 ; bottom surface and ARC
808 (sdedr:define-refinement-window
809     "global_botwin"
810     "Cuboid"
811     (position 0 (- SubstrateThickness (* RearCntExt_Y 10)) 0)
812     (position CellW (+ SubstrateThickness RearRcThickness) CellL)
813 )
814 (sdedr:define-refinement-size
815     "global_botsize"
816     gMeshX gMeshY gMeshZ
817     (/ gMeshX 5) (/ gMeshY 5) (/ gMeshZ 5)
818 )
819 (sdedr:define-refinement-function
820     "global_botsize"
821     "DopingConcentration"
822     "MaxTransDiff" 1.0
823 )
824 (sdedr:define-refinement-placement
825     "global_botplace"
826     "global_botsize"
```

```
827     "global_botwin"
828 )
829
830
831
832 ;front field refinement 1
833 (sdedr:define-refinement-window
834     "frontRegion_window"
835     "Cuboid"
836     (position 0 (+ FrontFieldJunc 0.3) 0)
837     (position CellW FrontCntExt_Y CellL)
838 )
839 (sdedr:define-multibox-size
840     "frontRegion_refsize"
841     (/ gMeshX 2) (+ FrontFieldJunc 0.3) gMeshZ
842     (/ gMeshX 2) (/ (+ FrontFieldJunc 0.3) 10) gMeshZ
843     1 1.2 1
844 )
845 (sdedr:define-multibox-placement
846     "frontRegion_refplace"
847     "frontRegion_refsize"
848     "frontRegion_window"
849 )
850
851 ;front field refinement 2
852 (sdedr:define-refinement-window
853     "frontRegion_window2"
854     "Cuboid"
855     (position 0 0 0)
856     (position CellW (+ FrontFieldJunc 0.3) CellL)
857 )
858 (sdedr:define-multibox-size
859     "frontRegion_refsize2"
860     (/ gMeshX 2) (/ (+ FrontFieldJunc 0.3) 10) gMeshZ
861     (/ gMeshX 2) (/ (+ FrontFieldJunc 0.3) 10) gMeshZ
862     1 1 1
863 )
864 (sdedr:define-multibox-placement
865     "frontRegion_refplace2"
866     "frontRegion_refsize2"
867     "frontRegion_window2"
868 )
869
870 (display "Front junction done, ")
871
872 ;; front local emitter refinement (use multiple refinement layers for better control
        of meshing)
873
874 ; Front local refinement 1
875 (sdedr:define-refinement-window
876     "frontCntShading_win3"
877     "Cuboid"
878     (position (+ HalfFrontCntWidth (+ FrontCntExt_X 10)) (* FrontCntExt_Y 5) 0)
879     (position (+ HalfFrontCntWidth (+ FrontCntExt_X 20)) (* FrontCntExt_Y 10) CellL)
880 )
881 (sdedr:define-multibox-size
882     "frontCntShading_size3"
883     (/ FrontCntWidth 8) 20 gMeshZ
884     (/ FrontCntWidth 8) 20 gMeshZ
885     1 1 1
886 )
887 (sdedr:define-multibox-placement
888     "frontCntShading_place3"
889     "frontCntShading_size3"
890     "frontCntShading_win3"
891 )
892
893 ; Front local refinement 2
```

```
(sdedr:define-refinement-window
    "frontCntShading_win2"
    "Cuboid"
    (position (+ HalfFrontCntWidth FrontCntExt_X) (+ EmitterJunc FrontCntExt_Y) 0)
    (position (+ HalfFrontCntWidth (+ FrontCntExt_X 10)) (* FrontCntExt_Y 5) CellL)
)
(sdedr:define-multibox-size
    "frontCntShading_size2"
    (/ FrontCntWidth 16) 20 gMeshZ
    (/ FrontCntWidth 16) 20 gMeshZ 1 1 1
)
(sdedr:define-multibox-placement
    "frontCntShading_place2"
    "frontCntShading_size2"
    "frontCntShading_win2"
)

; Front local refinement 3
(define minYmesh (min (/ (+ FrontFieldJunc 0.3) 10) 0.01))
(sdedr:define-refinement-window
    "frontContact_window"
    "Cuboid"
    (position (+ HalfFrontCntWidth FrontCntExt_X) (+ EmitterJunc FrontCntExt_Y) CellL
        )
    (position 0 0 0)
)
(sdedr:define-multibox-size
    "frontContact_refsize"
    (/ FrontCntWidth 20) (+ EmitterJunc FrontCntExt_Y) gMeshZ
    (/ FrontCntWidth 20) minYmesh gMeshZ
    1 1.1 1
)
(sdedr:define-multibox-placement
    "frontContact_refplace"
    "frontContact_refsize"
    "frontContact_window"
)

(display "Front local emitter done...")

;; rear contact refinement

;;; define a procedure

#if @rearContactPitch@ == 0
(define cntMeshSize1 20)
(define cntMeshSize2 20)
#elif @rearContactWidth@ <= 100
(define cntMeshSize2 10)
(define cntMeshSize1 5)
#else
(define cntMeshSize2 (/ RearCntWidth 10))
(define cntMeshSize1 (/ RearCntWidth 20))
#endif
(define cntMeshSize3 (/ RearCntWidth 5))

(define CreateRearCntMesh
    (lambda (win_name place_name Xll Zll Xur Zur Ext_xz Ext_y)
    ; Xll/Zll (lower-left), Xur/Zur (upper-right), Ext_xz (extension of the
        refinement window along X/Z direction)
        (begin
            (define win_ring1 (string-append win_name "_1")) ; most inner ring of
                refinement
            (define win_ring2 (string-append win_name "_2"))
            (define win_ring3 (string-append win_name "_3"))

            (define place_ring1 (string-append place_name "_1"))
            (define place_ring2 (string-append place_name "_2"))
```

```
959             (define place_ring3 (string-append place_name "_3"))
960
961             (sdedr:define-refinement-window win_ring1 "Cuboid"
962                 (position (- Xll Ext_xz) SubstrateThickness Zll)
963                 (position (+ Xur Ext_xz) (- SubstrateThickness (+ BSFJunc (* 1.5
                        Ext_y))) (+ Zur Ext_xz))
964
965             )
966
967             (sdedr:define-refinement-window win_ring2 "Cuboid"
968                 (position (- Xll (+ Ext_xz 30)) (- SubstrateThickness (+ BSFJunc (*
                        1.5 Ext_y))) Zll)
969                 (position (+ Xur (+ Ext_xz 30)) (- SubstrateThickness (* 5 Ext_y)) (+
                         Zur (+ Ext_xz 30)))
970
971             )
972
973             (sdedr:define-refinement-window win_ring3 "Cuboid"
974                 (position (- Xll (+ 70 Ext_xz)) (- SubstrateThickness (* 5 Ext_y))
                        Zll)
975                 (position (+ Xur (+ 70 Ext_xz)) (- SubstrateThickness (* 10 Ext_y))
                        (+ Zur (+ 70 Ext_xz)))
976
977             )
978
979             (sdedr:define-multibox-size "rearContact_ref1"
980                 cntMeshSize1 (/ (+ BSFJunc 0.3) 10) cntMeshSize1
981                 cntMeshSize1 (/ (+ BSFJunc 0.3) 25) cntMeshSize1
982                 1 0.9 1
983
984             )
985
986             (sdedr:define-multibox-size "rearContact_ref2"
987                 cntMeshSize2 (/ (+ BSFJunc 0.3) 2) cntMeshSize2
988                 cntMeshSize2 (/ (+ BSFJunc 0.3) 10) cntMeshSize2
989                 1 0.5 1
990
991             )
992
993             (sdedr:define-multibox-size "rearContact_ref3"
994                 cntMeshSize3 gMeshY cntMeshSize3
995                 cntMeshSize3 gMeshY cntMeshSize3
996                 1 1 1
997
998             )
999
1000            (sdedr:define-multibox-placement place_ring3 "rearContact_ref3" win_ring3
                    )
1001            (sdedr:define-multibox-placement place_ring2 "rearContact_ref2" win_ring2
                    )
1002            (sdedr:define-multibox-placement place_ring1 "rearContact_ref1" win_ring1
                    )
1003
1004        )
1005
1006    )
1007
1008 )
1009
1010 (if (or (= FlagFullBSF 1) (= FlagRearField 1))
1011     (begin
1012         (sdedr:define-refinement-window
1013             "rearCnt_win"
1014             "Cuboid"
1015             (position 0 SubstrateThickness 0)
1016             (position CellW (- SubstrateThickness (+ BSFJunc 0.3)) CellL)
1017         )
1018         (sdedr:define-multibox-size
```

```
1019                "rearCnt_ref"
1020                gMeshX (/ (+ BSFJunc 0.3) 2) gMeshZ ; max mesh sizes
1021                gMeshX (/ (+ BSFJunc 0.3) 10) gMeshZ ; min mesh sizes
1022                1 0.7 1
1023            )
1024            (sdedr:define-multibox-placement
1025                "rearCnt_place"
1026                "rearCnt_ref"
1027                "rearCnt_win"
1028            )
1029            (if (= FlagAllCnt 1)
1030                (begin
1031                    (DefineRearCnt "pContact_all" 0 0 CellW CellL)
1032                )
1033            )
1034        )
1035    )
1036
1037    (if (= FlagAllCnt 0)
1038        (begin
1039            (define myWinPrefix "rearCnt_win_")
1040            (define myWinName "rearCnt_win_")
1041            (define myPlacePrefix "rearCnt_place")
1042            (define myPlaceName "rearCnt_place")
1043            (define myFacePrefix "pContact_")
1044            (define myFaceName "pContact_")
1045            (set! totalCnt 0)
1046            (set! restSpaceX (- CellW ShiftX))
1047            (set! currentLocX ShiftX)
1048            (do ((x 0 (+ x 1))) ((= x numCnt_x))
1049                (begin
1050                    (set! myWinName (string-append myWinPrefix (number->string totalCnt))
                            )
1051                    (set! myPlaceName (string-append myPlacePrefix (number->string
                            totalCnt)))
1052                    (set! myFaceName (string-append myFacePrefix (number->string totalCnt
                            )))
1053                    (display "myWinName/myFaceName: ") (display myWinName) (display "/")
                            (display myFaceName) (newline)
1054                    (if (or (and (= x 0) (= ShiftX 0)) (= restSpaceX HalfRearCntWidth))
1055                    ;; if it's the first half-contact, or the last
1056                    (begin ; only room to place half contact in X direction
1057                        (CreateRearCntMesh
1058                            myWinName
1059                            myPlaceName
1060                            currentLocX
1061                            currentLocZ
1062                            (+ currentLocX HalfRearCntWidth)
1063                            (+ currentLocZ HalfRearCntWidth)
1064                            RearCntExt_XZ
1065                            RearCntExt_Y
1066                        )
1067                        (DefineRearCnt myFaceName currentLocX currentLocZ
1068                        (+ currentLocX HalfRearCntWidth) (+ currentLocZ HalfRearCntWidth)
                                )
1069                        (set! totalCnt (+ totalCnt 1))
1070                        (if (and (= x 0) (= ShiftX 0))
1071                        (begin
1072                            (set! currentLocX (+ currentLocX (- RearCntPitch
                                    HalfRearCntWidth)))
1073                            (set! restSpaceX (- restSpaceX (- RearCntPitch
                                    HalfRearCntWidth)))
1074                        )
1075                        )
1076                    )
1077                    (begin ; room to place whole contact in X direction
1078                        (CreateRearCntMesh
1079                            myWinName
```

```
1080                            myPlaceName
1081                            currentLocX currentLocZ
1082                            (+ currentLocX RearCntWidth) (+ currentLocZ HalfRearCntWidth)
1083                            RearCntExt_XZ RearCntExt_Y
1084                        )
1085                        (DefineRearCnt myFaceName currentLocX currentLocZ
1086                        (+ currentLocX RearCntWidth) (+ currentLocZ HalfRearCntWidth))
1087                        (set! totalCnt (+ totalCnt 1))
1088                        (set! currentLocX (+ currentLocX RearCntPitch))
1089                        (set! restSpaceX (- restSpaceX RearCntPitch))
1090                    )
1091                    )
1092                )
1093
1094            ) ; end of do-loop for X direction contact placement
1095
1096        )
1097
1098    )
1099    (display "Rear contacts done, ")
1100    (display "Finished mesh refinement.")(newline)
1101
1102    ;;-------------------------------------------------------------------------------

1103    ;; STEP 10: build mesh
1104
1105    (sde:build-mesh "snmesh" " -m 1000000 " "n@node@_msh")
```

A.3 sdevice.par

This file defines material parameters used in the Sentaurus Device simulation. Materials not defined here are unchanged from their default Sentaurus parameters. Parts of this file are based on a Sentaurus 3D simulation example [58]. The file is taken from model **Young5**.

```
Material = "Silicon" {
    ##from Altermatt models for numerical device simulations of crystall....
    Auger {
    * R_Auger = ( C_n n + C_p p ) ( n p - ni_eff^2)
    * with C_n,p = (A + B (T/T0) + C (T/T0)^2) (1 + H exp(-{n,p}/N0))
        A    = 2.8e-31 , 7.91e-32     # [cm^6/s]
        B    = 0,     -1.239e-32  # [cm^6/s]
        C    = 0 ,    3.231e-32   # [cm^6/s]
        H    = 8 ,    8 # [1]
        N0   = 2.5e+17 , 2.5e+17 # [cm^(-3)]
    }

    Epsilon
    { *  Ratio of the permittivities of material and vacuum

    * epsilon() = epsilon
        epsilon = 11.9  # [1] modified from 11.7 to 11.9 to match with PC1D by Kim
    }

    Bandgap {
        Eg0 = +1.1752165e+00  # n_i = 9.65e9 at 300 K (Altermatt PVSC Sapporo 1999)
        alpha = +4.73e-04
        beta = +6.36e+02
    }

    Scharfetter * relation and trap level for SRH recombination:
    {
    * tau = taumin + ( taumax - taumin ) / ( 1 + ( N/Nref )^gamma)
    * tau(T) = tau * ( (T/300)^Talpha )           (TempDep)
    * tau(T) = tau * exp( Tcoeff * ((T/300)-1) ) (ExpTempDep)
        taumin  = 0 ,  0     # [s]
        taumax  = @bulk_tau@ ,  @bulk_tau@     # [s]
    ** increase carrier lifetime. the other parameters are default values
    *       taumax  = 1.0000e-05 ,  3.0000e-06      # [s]
        Nref    = 1.0000e+16 ,  1.0000e+16      # [cm^(-3)]
        gamma   = 1 ,   1       # [1]
        Talpha  = -1.5000e+00 , -1.5000e+00     # [1]
        Tcoeff  = 2.55 ,        2.55    # [1]
        Etrap   = 0.0000e+00    # [eV]

    }

    SurfaceRecombination * surface SRH recombination:
    * currently using the default numbers
    { * s = S0 ( 1 + Sref ( N/Nref )^gamma ) recombination velocity
        S0      = 1.0000e+03 ,  1.0000e+03      # [cm/s]
        Sref    = 1.0000e-03    # [1]
        Nref    = 1.0000e+16    # [cm^(-3)]
        gamma   = 1     # [1]
        Etrap   = 0.0000e+00    # [eV]

    }

    * Schenk model
    TableBGN {
```

```
56          Acceptor   +1.0000000e+10   +000000000e+00
57          Acceptor   +1.0000000e+15   +1.4051583e-03
58          Acceptor   +1.1748976e+15   +1.5206727e-03
59          Acceptor   +1.3803843e+15   +1.6454732e-03
60          Acceptor   +1.6218101e+15   +1.7802713e-03
61          Acceptor   +1.9054607e+15   +1.9258276e-03
62          Acceptor   +2.2387211e+15   +2.0829536e-03
63          Acceptor   +2.6302680e+15   +2.2525147e-03
64          Acceptor   +3.0902954e+15   +2.4354322e-03
65          Acceptor   +3.6307805e+15   +2.6326857e-03
66          Acceptor   +4.2657952e+15   +2.8453154e-03
67          Acceptor   +5.0118723e+15   +3.0744238e-03
68          Acceptor   +5.8884366e+15   +3.3211775e-03
69          Acceptor   +6.9183097e+15   +3.5868093e-03
70          Acceptor   +8.1283052e+15   +3.8726185e-03
71          Acceptor   +9.5499259e+15   +4.1799729e-03
72          Acceptor   +1.1220185e+16   +4.5103084e-03
73          Acceptor   +1.3182567e+16   +4.8651296e-03
74          Acceptor   +1.5488166e+16   +5.2460092e-03
75          Acceptor   +1.8197009e+16   +5.6545873e-03
76          Acceptor   +2.1379621e+16   +6.0925695e-03
77          Acceptor   +2.5118864e+16   +6.5617248e-03
78          Acceptor   +2.9512092e+16   +7.0638822e-03
79          Acceptor   +3.4673685e+16   +7.6009265e-03
80          Acceptor   +4.0738028e+16   +8.1747919e-03
81          Acceptor   +4.7863009e+16   +8.7874538e-03
82          Acceptor   +5.6234133e+16   +9.4409168e-03
83          Acceptor   +6.6069345e+16   +1.0137196e-02
84          Acceptor   +7.7624712e+16   +1.0878292e-02
85          Acceptor   +9.1201084e+16   +1.1666151e-02
86          Acceptor   +1.0715193e+17   +1.2502602e-02
87          Acceptor   +1.2589254e+17   +1.3389274e-02
88          Acceptor   +1.4791084e+17   +1.4327467e-02
89          Acceptor   +1.7378008e+17   +1.5317973e-02
90          Acceptor   +2.0417379e+17   +1.6360844e-02
91          Acceptor   +2.3988329e+17   +1.7455116e-02
92          Acceptor   +2.8183829e+17   +1.8598517e-02
93          Acceptor   +3.3113112e+17   +1.9787260e-02
94          Acceptor   +3.8904514e+17   +2.1016072e-02
95          Acceptor   +4.5708819e+17   +2.2278648e-02
96          Acceptor   +5.3703180e+17   +2.3568704e-02
97          Acceptor   +6.3095734e+17   +2.4881569e-02
98          Acceptor   +7.4131024e+17   +2.6215946e-02
99          Acceptor   +8.7096359e+17   +2.7575083e-02
100         Acceptor   +1.0232930e+18   +2.8966616e-02
101         Acceptor   +1.2022644e+18   +3.0400895e-02
102         Acceptor   +1.4125375e+18   +3.1888388e-02
103         Acceptor   +1.6595869e+18   +3.3437288e-02
104         Acceptor   +1.9498446e+18   +3.5052217e-02
105         Acceptor   +2.2908677e+18   +3.6734250e-02
106         Acceptor   +2.6915348e+18   +3.8481835e-02
107         Acceptor   +3.1622777e+18   +4.0292000e-02
108         Acceptor   +3.7153523e+18   +4.2161341e-02
109         Acceptor   +4.3651583e+18   +4.4086607e-02
110         Acceptor   +5.1286138e+18   +4.6064873e-02
111         Acceptor   +6.0255959e+18   +4.8093417e-02
112         Acceptor   +7.0794578e+18   +5.0169411e-02
113         Acceptor   +8.3176377e+18   +5.2289550e-02
114         Acceptor   +9.7723722e+18   +5.4449713e-02
115         Acceptor   +1.1481536e+19   +5.6644789e-02
116         Acceptor   +1.3489629e+19   +5.8868845e-02
117         Acceptor   +1.5848932e+19   +6.1115840e-02
118         Acceptor   +1.8620871e+19   +6.3381069e-02
119         Acceptor   +2.1877616e+19   +6.5663281e-02
120         Acceptor   +2.5703958e+19   +6.7967054e-02
121         Acceptor   +3.0199517e+19   +7.0304467e-02
122         Acceptor   +3.5481339e+19   +7.2695032e-02
123         Acceptor   +4.1686938e+19   +7.5163362e-02
```

```
124          Acceptor   +4.8977882e+19   +7.7735212e-02
125          Acceptor   +5.7543994e+19   +8.0433422e-02
126          Acceptor   +6.7608298e+19   +8.3275258e-02
127          Acceptor   +7.9432823e+19   +8.6271728e-02
128          Acceptor   +9.3325430e+19   +8.9428500e-02
129          Acceptor   +1.0964782e+20   +9.2747564e-02
130          Acceptor   +1.2882496e+20   +9.6228912e-02
131          Acceptor   +1.5135612e+20   +9.9871838e-02
132          Acceptor   +1.7782794e+20   +1.0367577e-01
133          Acceptor   +2.0892961e+20   +1.0764072e-01
134          Acceptor   +2.4547089e+20   +1.1176740e-01
135          Acceptor   +2.8840315e+20   +1.1605729e-01
136          Acceptor   +3.3884416e+20   +1.2051250e-01
137          Acceptor   +3.9810717e+20   +1.2513568e-01
138          Acceptor   +4.6773514e+20   +1.2992990e-01
139          Acceptor   +5.4954087e+20   +1.3489856e-01
140          Acceptor   +6.4565423e+20   +1.4004528e-01
141          Acceptor   +7.5857758e+20   +1.4537385e-01
142          Acceptor   +8.9125094e+20   +1.5088819e-01
143          Acceptor   +1.0471285e+21   +1.5659232e-01
144          Acceptor   +1.2302688e+21   +1.6249042e-01
145          Acceptor   +1.4454398e+21   +1.6858680e-01
146          Acceptor   +1.6982437e+21   +1.7488602e-01
147          Acceptor   +1.9952623e+21   +1.8139296e-01
148          Acceptor   +2.3442288e+21   +1.8811299e-01
149          Acceptor   +2.7542287e+21   +1.9505213e-01
150          Acceptor   +3.2359366e+21   +2.0221722e-01
151          Acceptor   +3.8018940e+21   +2.0961622e-01
152          Acceptor   +4.4668359e+21   +2.1725839e-01
153          Acceptor   +5.2480746e+21   +2.2515463e-01
154          Acceptor   +6.1659500e+21   +2.3331769e-01
155          Acceptor   +7.2443596e+21   +2.4176248e-01
156          Acceptor   +8.5113804e+21   +2.5050626e-01
157          Acceptor   +1.0000000e+22   +2.5956885e-01
158          Donor      +1.0000000e+10   +000000000e+00
159          Donor      +1.0000000e+15   +1.4062347e-03
160          Donor      +1.1748976e+15   +1.5219386e-03
161          Donor      +1.3803843e+15   +1.6469623e-03
162          Donor      +1.6218101e+15   +1.7820231e-03
163          Donor      +1.9054607e+15   +1.9278886e-03
164          Donor      +2.2387211e+15   +2.0853788e-03
165          Donor      +2.6302680e+15   +2.2553687e-03
166          Donor      +3.0902954e+15   +2.4387915e-03
167          Donor      +3.6307805e+15   +2.6366404e-03
168          Donor      +4.2657952e+15   +2.8499720e-03
169          Donor      +5.0118723e+15   +3.0799081e-03
170          Donor      +5.8884366e+15   +3.3276384e-03
171          Donor      +6.9183097e+15   +3.5944230e-03
172          Donor      +8.1283052e+15   +3.8815942e-03
173          Donor      +9.5499259e+15   +4.1905585e-03
174          Donor      +1.1220185e+16   +4.5227991e-03
175          Donor      +1.3182567e+16   +4.8798772e-03
176          Donor      +1.5488166e+16   +5.2634341e-03
177          Donor      +1.8197009e+16   +5.6751936e-03
178          Donor      +2.1379621e+16   +6.1169637e-03
179          Donor      +2.5118864e+16   +6.5906400e-03
180          Donor      +2.9512092e+16   +7.0982093e-03
181          Donor      +3.4673685e+16   +7.6417546e-03
182          Donor      +4.0738028e+16   +8.2234619e-03
183          Donor      +4.7863009e+16   +8.8456296e-03
184          Donor      +5.6234133e+16   +9.5106804e-03
185          Donor      +6.6069345e+16   +1.0221177e-02
186          Donor      +7.7624712e+16   +1.0979842e-02
187          Donor      +9.1201084e+16   +1.1789578e-02
188          Donor      +1.0715193e+17   +1.2653491e-02
189          Donor      +1.2589254e+17   +1.3574911e-02
190          Donor      +1.4791084e+17   +1.4557386e-02
191          Donor      +1.7378008e+17   +1.5604661e-02
```

```
192          Donor      +2.0417379e+17   +1.6720575e-02
193          Donor      +2.3988329e+17   +1.7908875e-02
194          Donor      +2.8183829e+17   +1.9172870e-02
195          Donor      +3.3113112e+17   +2.0514899e-02
196          Donor      +3.8904514e+17   +2.1935611e-02
197          Donor      +4.5708819e+17   +2.3433144e-02
198          Donor      +5.3703180e+17   +2.5002439e-02
199          Donor      +6.3095734e+17   +2.6635059e-02
200          Donor      +7.4131024e+17   +2.8319882e-02
201          Donor      +8.7096359e+17   +3.0044811e-02
202          Donor      +1.0232930e+18   +3.1799142e-02
203          Donor      +1.2022644e+18   +3.3575801e-02
204          Donor      +1.4125375e+18   +3.5372605e-02
205          Donor      +1.6595869e+18   +3.7192170e-02
206          Donor      +1.9498446e+18   +3.9040695e-02
207          Donor      +2.2908677e+18   +4.0926272e-02
208          Donor      +2.6915348e+18   +4.2857330e-02
209          Donor      +3.1622777e+18   +4.4841561e-02
210          Donor      +3.7153523e+18   +4.6885363e-02
211          Donor      +4.3651583e+18   +4.8993682e-02
212          Donor      +5.1286138e+18   +5.1170056e-02
213          Donor      +6.0255959e+18   +5.3416736e-02
214          Donor      +7.0794578e+18   +5.5734777e-02
215          Donor      +8.3176377e+18   +5.8124085e-02
216          Donor      +9.7723722e+18   +6.0583432e-02
217          Donor      +1.1481536e+19   +6.3110525e-02
218          Donor      +1.3489629e+19   +6.5702249e-02
219          Donor      +1.5848932e+19   +6.8355268e-02
220          Donor      +1.8620871e+19   +7.1067129e-02
221          Donor      +2.1877616e+19   +7.3837903e-02
222          Donor      +2.5703958e+19   +7.6672069e-02
223          Donor      +3.0199517e+19   +7.9579985e-02
224          Donor      +3.5481339e+19   +8.2578090e-02
225          Donor      +4.1686938e+19   +8.5687344e-02
226          Donor      +4.8977882e+19   +8.8930252e-02
227          Donor      +5.7543994e+19   +9.2327600e-02
228          Donor      +6.7608298e+19   +9.5896151e-02
229          Donor      +7.9432823e+19   +9.9647875e-02
230          Donor      +9.3325430e+19   +1.0359053e-01
231          Donor      +1.0964782e+20   +1.0772892e-01
232          Donor      +1.2882496e+20   +1.1206626e-01
233          Donor      +1.5135612e+20   +1.1660522e-01
234          Donor      +1.7782794e+20   +1.2134866e-01
235          Donor      +2.0892961e+20   +1.2630001e-01
236          Donor      +2.4547089e+20   +1.3146340e-01
237          Donor      +2.8840315e+20   +1.3684371e-01
238          Donor      +3.3884416e+20   +1.4244647e-01
239          Donor      +3.9810717e+20   +1.4827781e-01
240          Donor      +4.6773514e+20   +1.5434434e-01
241          Donor      +5.4954087e+20   +1.6065310e-01
242          Donor      +6.4565423e+20   +1.6721147e-01
243          Donor      +7.5857758e+20   +1.7402714e-01
244          Donor      +8.9125094e+20   +1.8110807e-01
245          Donor      +1.0471285e+21   +1.8846250e-01
246          Donor      +1.2302688e+21   +1.9609897e-01
247          Donor      +1.4454398e+21   +2.0402636e-01
248          Donor      +1.6982437e+21   +2.1225397e-01
249          Donor      +1.9952623e+21   +2.2079164e-01
250          Donor      +2.3442288e+21   +2.2964992e-01
251          Donor      +2.7542287e+21   +2.3884018e-01
252          Donor      +3.2359366e+21   +2.4837493e-01
253          Donor      +3.8018940e+21   +2.5826799e-01
254          Donor      +4.4668359e+21   +2.6853482e-01
255          Donor      +5.2480746e+21   +2.7919283e-01
256          Donor      +6.1659500e+21   +2.9026166e-01
257          Donor      +7.2443596e+21   +3.0176349e-01
258          Donor      +8.5113804e+21   +3.1372335e-01
259          Donor      +1.0000000e+22   +3.2616938e-01
```

```
260
261     }
262
263 }
264
265 Material = "FrontDielectric" {
266     Insert = "Si3N4.par"
267
268 }
269
270 Material = "RearDielectric" {
271     Insert = "Si3N4.par"
272
273 }
274
275 MaterialInterface = "FrontDielectric/Silicon" {
276   SurfaceRecombination {
277     S0 = @Si_FrontArc_SRH_S0@, @Si_FrontArc_SRH_S0@ * [cm/s]
278     Sref = 0 * [1]
279   }
280 }
281
282 MaterialInterface = "RearDielectric/Silicon" {
283   SurfaceRecombination {
284     S0 = @Si_RearRc_SRH_S0@, @Si_RearRc_SRH_S0@ * [cm/s]
285     Sref = 0 * [1]
286   }
287 }
288
289 MaterialInterface = "Aluminum/Silicon" {
290   SurfaceRecombination {
291     S0 = @Si_Al_SRH_S0@, @Si_Al_SRH_S0@ * [cm/s]
292     Sref = 0 * [1]
293   }
294 }
295
296 MaterialInterface = "Silver/Silicon" {
297   SurfaceRecombination {
298     S0 = @Si_Silver_SRH_S0@, @Si_Silver_SRH_S0@ * [cm/s]
299     Sref = 0 * [1]
300   }
301 }
```

A.4 sdevice_des.cmd

This file serves as input for Sentaurus Device. It contains the instructions for the numerical solver, including definition of the simulation steps and selection of output variables. Parts of this file are based on a Sentaurus 3D simulation example [58]. The file is taken from model **Young5**.

```
#setdep @previous@

File {
  grid= "@tdr@"
  OpticalGenerationInput= "@tdr@"
  Plot= "@tdrdat@"
  Current= "@plot@"
  Output= "@log@"
  Parameter= "@parameter@"
}

*---------------------------------------------------
Electrode {
    {
        name="pContact"
        voltage= 0.0
    }
    {
        name="nContact"
        voltage= 0.0
    }
}

*---------------------------------------------------
Plot {
  DopingConcentration BoronActiveConcentration PhosphorusActiveConcentration
  BandGap ConductionBandEnergy ValenceBandEnergy
  eCurrent/Vector hCurrent/Vector current/vector
  SpaceCharge eDensity hDensity
  Potential
  eMobility hMobility
  SRH Auger TotalRecombination SurfaceRecombination
  eLifeTime hLifeTime
  EffectiveIntrinsicDensity IntrinsicDensity
  OpticalGeneration
}

CurrentPlot{
  OpticalGeneration(Integrate(Semiconductor) )
  OpticalGeneration(Integrate(material="Silicon") )
  SRH(Integrate(Semiconductor))
  Auger(Integrate(Semiconductor))
}

*---------------------------------------------------

Physics {
  Recombination(
    SRH(DopingDependence)
    Auger
  )
  Mobility(PhuMob(Klaassen Phosphorus))
  EffectiveIntrinsicDensity(TableBGN)
```

```
54    Fermi(-WithJoyceDixon)
55    Optics(
56      OpticalGeneration(
57        ReadFromFile(
58          TimeDependence(
59            WaveTime= (1, 2)
60            WaveTSlope= 0.05
61          )
62        )
63      )
64    )
65  }
66
67  Physics (MaterialInterface="FrontDielectric/Silicon") { Recombination(surfaceSRH) }
68  #if @rearContactPitch@ != 0
69  Physics (MaterialInterface="RearDielectric/Silicon") { Recombination(surfaceSRH) }
70  #endif
71
72  # Top contact
73  Physics (MaterialInterface="Aluminum/Silicon") { Recombination(surfaceSRH) }
74
75  # Bottom contact
76  Physics (MaterialInterface="Silver/Silicon") { Recombination(surfaceSRH) }
77
78  *---------------------------------------------------
79  Math{
80    Extrapolate
81    Derivatives
82    ExitOnFailure
83    Iterations= 30
84    Method= ils
85    ILSrc=
86    "set(1){
87      iterative(gmres(100), tolrel=1e-10, tolunprec=1e-8, tolabs=0, maxit=200);
88      preconditioning(ilut(0.001,-1),left);
89      ordering (symmetric=nd, nonsymmetric=mpsilst);
90      options(compact=yes, linscale=0, refineresidual=8, verbose=5); }; "
91    Number_of_Threads= maximum
92    BreakCriteria {
93     Current (Contact= "pContact" maxval= 1e-16)
94    }
95  }
96
97  *---------------------------------------------------
98  Solve{
99      NewCurrentPrefix= "tmp_"
100     Poisson
101     NewCurrentPrefix= ""
102
103     Transient (
104         InitialTime= 0
105         FinalTime= 1.2
106         InitialStep= 1
107         MaxStep= 1
108         MinStep= 1e-5
109
110     )
111     { Coupled {Poisson Electron Hole} }
112
113     Quasistationary (
114         InitialStep= 0.2
115         MaxStep= 0.2
116         MinStep= 1e-6
117         DoZero
118         Goal { Name= "pContact" voltage= 0.4 }
119
120     )
121     { Coupled {Poisson Electron Hole} }
```

```
122
123     Plot(FilePrefix= "n@node@_op")
124
125     Quasistationary (
126         InitialStep= 0.02
127         MaxStep= 0.02
128         MinStep= 1e-6
129         Goal { Name= "pContact" voltage= 0.8 }
130     )
131     { Coupled {Poisson Electron Hole} }
132
133     System("rm -f tmp_*")
134
135 }
```

A.5 fileutil_tcl.cmd

This file contains commands to transform variable names from Sentaurus Process convention to Sentaurus Device convention. The file is taken from model **Young5**.

```
#setdep @node|Emitter@
#setdep @node|FrontField@
#setdep @node|BSF@
#setdep @node|RearField@

#if @enableEmitter@ == 1
    # Change exported data labels to Sentaurus Device convention
    set FID [open profile_n@node|Emitter@.plx "r"]
    set fileData [read $FID]
    close $FID

    set FID [open profile_n@node|Emitter@.plx "w"]
    set istartphos [expr [string first "PActive" $fileData]]
    if {$istartphos != -1} {
        set fileData [string replace $fileData $istartphos [expr $istartphos + 6] "
            PhosphorusActiveConcentration"]
    }

    set istartboron [expr [string first "BActive" $fileData]]
    if {$istartboron != -1} {
        set fileData [string replace $fileData $istartboron [expr $istartboron + 6] "
            BoronActiveConcentration"]
    }

    puts $FID $fileData
    close $FID
#endif


#if @enableFrontField@ == 1
    # Change exported data labels to Sentaurus Device convention
    set FID [open profile_n@node|FrontField@.plx "r"]
    set fileData [read $FID]
    close $FID

    set FID [open profile_n@node|FrontField@.plx "w"]
    set istartphos [expr [string first "PActive" $fileData]]
    if {$istartphos != -1} {
        set fileData [string replace $fileData $istartphos [expr $istartphos + 6] "
            PhosphorusActiveConcentration"]
    }

    set istartboron [expr [string first "BActive" $fileData]]
    if {$istartboron != -1} {
        set fileData [string replace $fileData $istartboron [expr $istartboron + 6] "
            BoronActiveConcentration"]
    }

    puts $FID $fileData
    close $FID
#endif

#if @enableBSF@ == 1
    # Change exported data labels to Sentaurus Device convention
    set FID [open profile_n@node|BSF@.plx "r"]
    set fileData [read $FID]
    close $FID
```

```
54
55      set FID [open profile-n@node|BSF@.plx "w"]
56      set istartphos [expr [string first "PActive" $fileData]]
57      if {$istartphos != -1} {
58          set fileData [string replace $fileData $istartphos [expr $istartphos + 6] "
                PhosphorusActiveConcentration"]
59      }
60
61      set istartboron [expr [string first "BActive" $fileData]]
62      if {$istartboron != -1} {
63          set fileData [string replace $fileData $istartboron [expr $istartboron + 6] "
                BoronActiveConcentration"]
64      }
65
66      puts $FID $fileData
67      close $FID
68  #endif
69
70  #if @enableRearField@ == 1
71      # Change exported data labels to Sentaurus Device convention
72      set FID [open profile-n@node|RearField@.plx "r"]
73      set fileData [read $FID]
74      close $FID
75
76      set FID [open profile-n@node|RearField@.plx "w"]
77      set istartphos [expr [string first "PActive" $fileData]]
78      if {$istartphos != -1} {
79          set fileData [string replace $fileData $istartphos [expr $istartphos + 6] "
                PhosphorusActiveConcentration"]
80      }
81
82      set istartboron [expr [string first "BActive" $fileData]]
83      if {$istartboron != -1} {
84          set fileData [string replace $fileData $istartboron [expr $istartboron + 6] "
                BoronActiveConcentration"]
85      }
86
87      puts $FID $fileData
88      close $FID
89  #endif
```

Bibliography

[1] J. Benick, B. Hoex, M. Van de Sanden, W. Kessels, O. Schultz, and S. W. Glunz, "High efficiency n-type si solar cells on alo-passivated boron emitters," *Applied Physics Letters*, vol. 92, p. 253504, 2008.

[2] pveducation.org. http://www.pveducation.org/pvcdrom/manufacturing/high-efficiency.

[3] L. Rubin and J. Poate, "Ion implantation in silicon technology," *Industrial Physicist*, vol. 9, no. 3, pp. 12–15, 2003.

[4] A. Rohatgi, D. L. Meier, B. McPherson, Y.-W. Ok, A. D. Upadhyaya, J.-H. Lai, and F. Zimbardi, "High-throughput ion-implantation for low-cost high-efficiency silicon solar cells," *Energy Procedia*, vol. 15, pp. 10–19, 2012.

[5] J. Schermer, A. Martinez-Limia, P. Pichler, C. Zechner, W. Lerch, and S. Paul, "On a computationally efficient approach to boron-interstitial clustering," *Solid-State Electronics*, vol. 52, no. 9, pp. 1424–1429, 2008.

[6] B. Pawlak, T. Janssens, S. Singh, I. Kuzma-Filipek, J. Robbelein, N. Posthuma, J. Poortmans, F. Cristiano, and E. Bazizi, "Studies of implanted boron emitters for solar cell applications," *Progress in Photovoltaics: Research and Applications*, vol. 20, no. 1, pp. 106–110, 2012.

[7] Z. Essa. Personal Communication.

[8] J. Benick, B. Hoex, G. Dingemans, A. Richter, M. Hermle, and S. Glunz, "High-efficiency n-type silicon solar cells with front side boron emitter," in *Proceedings of the 24th European Photovoltaic Solar Energy Conference*, pp. 863–870, 2009.

[9] J. Poortmans, K. Baert, J. Hozel, N. Posthuma, J. John, G. Flamand, I. Gordon, F. Bruynseels, and R. Mertens, "Where photovoltaics meets microelectronics," *Energy Procedia*, vol. 15, pp. 40–49, 2012.

[10] T. Ohrdes, S. Steingrube, H. Wagner, C. Zechner, G. Letay, R. Chen, S. Dunham, and P. Altermatt, "Solar cell emitter design with pv-tailored implantation," *Energy Procedia*, vol. 8, pp. 167–173, 2011.

[11] Y.-W. Ok, A. D. Upadhyaya, Y. Tao, F. Zimbardi, S. Ning, and A. Rohatgi, "Ion-implanted and screen-printed large area 19.6% efficient n-type bifacial si solar cell," in *Photovoltaic Specialists Conference (PVSC), 2012 38th IEEE*, pp. 002240–002243, IEEE, 2012.

[12] A. Wang, J. Zhao, and M. Green, "24% efficient silicon solar cells," *Applied physics letters*, vol. 57, no. 6, pp. 602–604, 1990.

[13] S. Glunz, S. Rein, J. Lee, and W. Warta, "Minority carrier lifetime degradation in boron-doped czochralski silicon," *Journal of Applied Physics*, vol. 90, no. 5, pp. 2397–2404, 2001.

[14] D. Macdonald and L. Geerligs, "Recombination activity of interstitial iron and other transition metal point defects in< equation> p</equation>-and< equation> n</equation>-type crystalline silicon," *Applied Physics Letters*, vol. 85, no. 18, pp. 4061–4063, 2004.

[15] V. Mihailetchi, G. Coletti, Y. Komatsu, L. Geerligs, R. Kvande, L. Arnberg, K. Wambach, C. Knopf, R. Kopecek, and A. Weeber, "Large area screen printed n-type base silicon solar cells with efficiency exceeding 18%," *Solar Energy*, vol. 2011, p. 2010, 2012.

[16] J. Schmidt, A. Merkle, R. Brendel, B. Hoex, M. v. de Sanden, and W. Kessels, "Surface passivation of high-efficiency silicon solar cells by atomic-layer-deposited al2o3," *Progress in Photovoltaics: Research and Applications*, vol. 16, no. 6, pp. 461–466, 2008.

[17] J. Schmidt and M. Kerr, "Highest-quality surface passivation of low-resistivity p-type silicon using stoichiometric pecvd silicon nitride," *Solar Energy Materials and Solar Cells*, vol. 65, no. 1, pp. 585–591, 2001.

[18] M. A. Green, "High-efficiency silicon solar cells," in *Asia Pacific Symposium on Microelectronics and MEMS*, pp. 49–59, International Society for Optics and Photonics, 1999.

[19] J. Zhao, A. Wang, and M. A. Green, "24· 5% efficiency silicon pert cells on mcz substrates and 24· 7% efficiency perl cells on fz substrates," *Progress in Photovoltaics: Research and Applications*, vol. 7, no. 6, pp. 471–474, 1999.

[20] Y. W. Ok. Personal Communication.

[21] S. Ramanathan, A. Das, I. Cooper, A. Rohatgi, A. Payne, and I. Koehler, "20% efficient screen printed lbsf cell fabricated using uv laser for rear dielectric removal," in *Photovoltaic Specialists Conference (PVSC), 2010 35th IEEE*, pp. 000678–000682, IEEE, 2010.

[22] J.-H. Lai, A. Upadhyaya, S. Ramanathan, A. Das, K. Tate, V. Upadhyaya, A. Kapoor, C.-W. Chen, and A. Rohatgi, "High-efficiency large-area rear passivated silicon solar cells with local al-bsf and screen-printed contacts," *Photovoltaics, IEEE Journal of*, vol. 1, no. 1, pp. 16–21, 2011.

[23] E. Schneiderlöchner, R. Preu, R. Lüdemann, and S. Glunz, "Laser-fired rear contacts for crystalline silicon solar cells," *Progress in Photovoltaics: Research and Applications*, vol. 10, no. 1, pp. 29–34, 2002.

[24] M. B. Spitzer, S. P. Tobin, and C. J. Keavney, "High-efficiency ion-implanted silicon solar cells," *Electron Devices, IEEE Transactions on*, vol. 31, no. 5, pp. 546–550, 1984.

[25] M. Spitzer and C. Keavney, "Attainment of transparent boron-implanted layers for silicon solar cell applications," *Applied physics letters*, vol. 47, p. 731, 1985.

[26] A. Rohatgi and D. Meier, "Developing novel low-cost, high-throughput processing techniques for 20%-efficient monocrystalline silicon solar cells," *Photovoltaics International*, vol. 10, pp. 87–93, 2010.

[27] N. Bateman, P. Sullivan, C. Reichel, J. Benick, and M. Hermle, "High quality ion implanted boron emitters in an interdigitated back contact solar cell with 20% efficiency," *Energy Procedia*, vol. 8, pp. 509–514, 2011.

[28] E. Chason, S. Picraux, J. Poate, J. Borland, M. Current, T. Diaz de La Rubia, D. Eaglesham, O. Holland, M. Law, C. Magee, *et al.*, "Ion beams in silicon processing and characterization," *Journal of applied physics*, vol. 81, no. 10, pp. 6513–6561, 1997.

[29] S. A. Campbell, *Fabrication engineering at the micro and nanoscale*. Oxford University Press, 2008.

[30] D. Macdonald, H. Maeckel, S. Doshi, W. Brendle, A. Cuevas, J. Williams, and M. Conway, "Carrier lifetime studies of deeply penetrating defects in self-ion implanted silicon," *Applied physics letters*, vol. 82, no. 18, pp. 2987–2989, 2003.

[31] D. Macdonald, P. N. Deenapanray, and S. Diez, "Onset of implant-related recombination in self-ion implanted and annealed crystalline silicon," *Journal of applied physics*, vol. 96, no. 7, pp. 3687–3691, 2004.

[32] F. Cristiano, N. Cherkashin, X. Hebras, P. Calvo, Y. Lamrani, E. Scheid, B. De Mauduit, B. Colombeau, W. Lerch, S. Paul, *et al.*, "Ion beam induced defects in crystalline silicon," *Nuclear Instruments and Methods in Physics Research Section B: Beam Interactions with Materials and Atoms*, vol. 216, pp. 46–56, 2004.

[33] K. Ryu, A. Upadhyaya, Y.-W. Ok, H. Xu, L. Metin, and A. Rohatgi, "High efficiency n-type solar cells with screen-printed boron emitters and ion-implanted back surface field," in *Photovoltaic Specialists Conference (PVSC), 2012 38th IEEE*, pp. 002247–002249, IEEE, 2012.

[34] C. Ho, J. Plummer, J. Meindl, and B. Deal, "Thermal oxidation of heavily phosphorus-doped silicon," *Journal of the Electrochemical Society*, vol. 125, no. 4, pp. 665–671, 1978.

[35] C. E. Dubé, B. Tsefrekas, D. Buzby, R. Tavares, W. Zhang, A. Gupta, R. J. Low, W. Skinner, and J. Mullin, "High efficiency selective emitter cells using patterned ion implantation," *Energy Procedia*, vol. 8, pp. 706–711, 2011.

[36] P. P. Altermatt, "Models for numerical device simulations of crystalline silicon solar cells - a review," *Journal of computational electronics*, vol. 10, no. 3, pp. 314–330, 2011.

[37] Synopsys, *Sentaurus Device User Guide (Version G-2012.06)*, 2012.

[38] Synopsys, *Sentaurus Process User Guide (Version G-2012.06)*, 2012.

[39] Synopsys, *Sentaurus Structure Editor User Guide (Version G-2012.06)*, 2012.

[40] Synopsys, *Sentaurus Workbench User Guide (Version G-2012.06)*, 2012.

[41] Synopsys, *Solvers User Guide (Version G-2012.06)*, 2012.

[42] V. Meemongkolkiat, *Development of High Efficiency Monocrystalline Si Solar Cells Through Improved Optical and Electrical Confinement.* PhD thesis, Georgia Institute of Technology, 2008.

[43] S. Jain, W. Schoenmaker, R. Lindsay, P. Stolk, S. Decoutere, M. Willander, and H. Maes, "Transient enhanced diffusion of boron in si," *Journal of applied physics*, vol. 91, no. 11, pp. 8919–8941, 2002.

[44] L. Shao, J. Liu, Q. Y. Chen, and W.-K. Chu, "Boron diffusion in silicon: the anomalies and control by point defect engineering," *Materials Science and Engineering: R: Reports*, vol. 42, no. 3, pp. 65–114, 2003.

[45] P. Stolk, H.-J. Gossmann, D. Eaglesham, D. Jacobson, C. Rafferty, G. Gilmer, M. Jaraiz, J. Poate, H. Luftman, and T. Haynes, "Physical mechanisms of transient enhanced dopant diffusion in ion-implanted silicon," *Journal of applied physics*, vol. 81, no. 9, pp. 6031–6050, 1997.

[46] N. Zographos, C. Zechner, and I. Avci, "Efficient tcad model for the evolution of interstitial clusters,{311} defects, and dislocation loops in silicon," in *MATERIALS RESEARCH SOCIETY SYMPOSIUM PROCEEDINGS*, vol. 994, p. 297, Cambridge Univ Press, 2007.

[47] S. Mirabella, E. Bruno, F. Priolo, D. De Salvador, E. Napolitani, A. Drigo, and A. Carnera, "Dissolution kinetics of boron-interstitial clusters in silicon," *Applied physics letters*, vol. 83, no. 4, pp. 680–682, 2003.

[48] S. Boninelli, S. Mirabella, E. Bruno, F. Priolo, F. Cristiano, A. Claverie, D. De Salvador, G. Bisognin, and E. Napolitani, "Evolution of boron-interstitial clusters in crystalline si studied by transmission electron microscopy," *Applied Physics Letters*, vol. 91, no. 3, pp. 031905–031905, 2007.

[49] C. J. Ortiz, P. Pichler, T. Fuhner, F. Cristiano, B. Colombeau, N. E. Cowern, and A. Claverie, "A physically based model for the spatial and temporal evolution of self-interstitial agglomerates in ion-implanted silicon," *Journal of applied physics*, vol. 96, no. 9, pp. 4866–4877, 2004.

[50] P. Pichler, C. J. Ortiz, B. Colombeau, N. E. Cowern, E. Lampin, S. Uppal, M. Karunaratne, J. M. Bonar, A. F. Willoughby, A. Claverie, *et al.*, "Diffusion and activation of dopants in silicon and advanced silicon-based materials," *Physica Scripta*, vol. 2006, no. T126, p. 89, 2006.

[51] Y.-S. Oh and D. E. Ward, "A calibrated model for trapping of implanted dopants at material interface during thermal annealing," in *Electron Devices Meeting, 1998. IEDM'98. Technical Digest., International*, pp. 509–512, IEEE, 1998.

[52] K. Ryu, A. Upadhyaya, H.-J. Song, C.-J. Choi, A. Rohatgi, and Y.-W. Ok, "Chemical etching of boron-rich layer and its impact on high efficiency n-type silicon solar cells," *Applied Physics Letters*, vol. 101, no. 7, pp. 073902–073902, 2012.

[53] T. Ambridge, C. Elliott, and M. Faktor, "The electrochemical characterization of n-type gallium arsenide," *Journal of Applied Electrochemistry*, vol. 3, no. 1, pp. 1–15, 1973.

[54] R. Bock, P. P. Altermatt, and J. Schmidt, "Accurate extraction of doping profiles from electrochemical capacitance voltage measurements," *WIP Munich, Proc. 23rd EU PVSEC, Valencia,(Sept. 2008)*, pp. 1510–1513, 2008.

[55] D. Hinken, A. Milsted, R. Bock, B. Fischer, K. Bothe, M. Schutze, J. Isenberg, A. Schulze, and M. Wagner, "Determination of the base-dopant concentration of large-area crystalline silicon solar cells," *Electron Devices, IEEE Transactions on*, vol. 57, no. 11, pp. 2831–2837, 2010.

[56] M. Uematsu, "Simulation of boron, phosphorus, and arsenic diffusion in silicon based on an integrated diffusion model, and the anomalous phosphorus diffusion mechanism," *Journal of applied physics*, vol. 82, no. 5, pp. 2228–2246, 1997.

[57] F. Lau, L. Mader, C. Mazure, C. Werner, and M. Orlowski, "A model for phosphorus segregation at the silicon-silicon dioxide interface," *Applied Physics A*, vol. 49, no. 6, pp. 671–675, 1989.

[58] Synopsys, *Optimization of Rear Contact Design in Monocrystalline Silicon Solar-Cell Using 3D TCAD Simulations*, 2010.

[59] P. Altermatt, H. Plagwitz, R. Bock, J. Schmidt, R. Brendel, M. Kerr, and A. Cuevas, "The surface recombination velocity at boron-doped emitters: comparison between various passivation techniques," in *Proceedings of the 21st European Photovoltaic Solar Energy Conference*, pp. 647–650, 2006.

[60] A. Guo, F. Ye, L. Guo, D. Ji, and S. Feng, "Effect of the back surface topography on the efficiency in silicon solar cells," *Journal of Semiconductors*, vol. 30, no. 7, p. 074003, 2009.

[61] S. W. Glunz, A. B. Sproul, W. Warta, and W. Wettling, "Injection-level-dependent recombination velocities at the si-sio 2 interface for various dopant concentrations," *Journal of applied physics*, vol. 75, no. 3, pp. 1611–1615, 1994.

[62] A. G. Aberle, T. Lauinger, J. Schmidt, and R. Hezel, "Injection-level dependent surface recombination velocities at the silicon-plasma silicon nitride interface," *Applied physics letters*, vol. 66, no. 21, pp. 2828–2830, 1995.

[63] A. Cuevas, P. A. Basore, G. Giroult-Matlakowski, and C. Dubois, "Surface recombination velocity of highly doped n-type silicon," *Journal of Applied Physics*, vol. 80, no. 6, pp. 3370–3375, 1996.

[64] R. A. Sinton and A. Cuevas, "Contactless determination of current–voltage characteristics and minority-carrier lifetimes in semiconductors from quasi-steady-state photoconductance data," *Applied Physics Letters*, vol. 69, no. 17, pp. 2510–2512, 1996.

[65] D. K. Schroder, "Carrier lifetimes in silicon," *Electron Devices, IEEE Transactions on*, vol. 44, no. 1, pp. 160–170, 1997.

[66] A. Cuevas, "The effect of emitter recombination on the effective lifetime of silicon wafers," *Solar energy materials and solar cells*, vol. 57, no. 3, pp. 277–290, 1999.

[67] H. Mäckel and K. Varner, "On the determination of the emitter saturation current density from lifetime measurements of silicon devices," *Progress in Photovoltaics: Research and Applications*, 2012.

[68] A. Cuevas and D. Macdonald, "Measuring and interpreting the lifetime of silicon wafers," *Solar Energy*, vol. 76, no. 1, pp. 255–262, 2004.

[69] P. P. Altermatt, A. Schenk, F. Geelhaar, and G. Heiser, "Reassessment of the intrinsic carrier density in crystalline silicon in view of band-gap narrowing," *Journal of applied physics*, vol. 93, no. 3, pp. 1598–1604, 2003.

[70] A. Schenk, "Finite-temperature full random-phase approximation model of band gap narrowing for silicon device simulation," *Journal of applied physics*, vol. 84, no. 7, pp. 3684–3695, 1998.

[71] D. Klaassen, "A unified mobility model for device simulation - i. model equations and concentration dependence," *Solid-State Electronics*, vol. 35, no. 7, pp. 953–959, 1992.

[72] J. Dziewior and W. Schmid, "Auger coefficients for highly doped and highly excited silicon," *Applied Physics Letters*, vol. 31, no. 5, pp. 346–348, 1977.

[73] D. Roulston, N. Arora, and S. Chamberlain, "Modeling and measurement of minority-carrier lifetime versus doping in diffused layers of n< sup>+</sup>-p silicon diodes," *Electron Devices, IEEE Transactions on*, vol. 29, no. 2, pp. 284–291, 1982.

[74] B. Rounsaville. Personal Communication.